

University of Windsor

## Scholarship at UWindor

---

Electronic Theses and Dissertations

Theses, Dissertations, and Major Papers

---

10-30-2020

# Development of Graphene-Filled Fluoropolymer Composite Coatings for Condensing Heat Exchangers

Mitchell Jacob Cierpisz  
*University of Windsor*

Follow this and additional works at: <https://scholar.uwindsor.ca/etd>

---

### Recommended Citation

Cierpisz, Mitchell Jacob, "Development of Graphene-Filled Fluoropolymer Composite Coatings for Condensing Heat Exchangers" (2020). *Electronic Theses and Dissertations*. 8441.  
<https://scholar.uwindsor.ca/etd/8441>

This online database contains the full-text of PhD dissertations and Masters' theses of University of Windsor students from 1954 forward. These documents are made available for personal study and research purposes only, in accordance with the Canadian Copyright Act and the Creative Commons license—CC BY-NC-ND (Attribution, Non-Commercial, No Derivative Works). Under this license, works must always be attributed to the copyright holder (original author), cannot be used for any commercial purposes, and may not be altered. Any other use would require the permission of the copyright holder. Students may inquire about withdrawing their dissertation and/or thesis from this database. For additional inquiries, please contact the repository administrator via email ([scholarship@uwindsor.ca](mailto:scholarship@uwindsor.ca)) or by telephone at 519-253-3000ext. 3208.

**DEVELOPMENT OF GRAPHENE-FILLED  
FLUOROPOLYMER COMPOSITE COATINGS FOR  
CONDENSING HEAT EXCHANGERS**

By

**Mitchell Cierpisz**

A Thesis

Submitted to the Faculty of Graduate Studies  
through the Department of Mechanical, Automotive and Materials Engineering  
in Partial Fulfillment of the Requirements for  
the Degree of Master of Applied Science at the  
University of Windsor

Windsor, Ontario, Canada

© 2020 Mitchell Cierpisz

# **DEVELOPMENT OF GRAPHENE-FILLED FLUOROPOLYMER COMPOSITE COATINGS FOR CONDENSING HEAT EXCHANGERS**

By

**Mitchell Cierpisz**

APPROVED BY:

---

M. Mirhassani

Department of Electrical and Computer Engineering

---

R. Riahi

Department of Mechanical, Automotive and Materials Engineering

---

A. Edrisy, Co-Advisor

Department of Mechanical, Automotive and Materials Engineering

---

Y. He, Co-Advisor

CanmetMATERIALS, Natural Resources Canada

September 4, 2020

## **Declaration of Co-Authorship**

I hereby declare that this thesis incorporates material that is result of joint research between Natural Resources Canada's CanmetMATERIALS and the University of Windsor's Department of Mechanical, Automotive and Materials Engineering, under the supervision of Dr. A. Edrisy. CanmetMATERIALS provided technical knowledge and experimental facilities in the research project. In all cases, the key ideas, primary contributions, experimental designs, data analysis, interpretation and writing were performed by the author.

I am aware of the University of Windsor Senate Policy on Authorship and I certify that I have properly acknowledged the contribution of other researchers to my thesis, and have obtained written permission from each of the co-author(s) to include the above material(s) in my thesis.

I certify that, with the above qualification, this thesis, and the research to which it refers, is the product of my own work.

I declare that, to the best of my knowledge, my thesis does not infringe upon anyone's copyright nor violate any proprietary rights and that any ideas, techniques, quotations, or any other material from the work of other people included in my thesis, published or otherwise, are fully acknowledged in accordance with the standard referencing practices. Furthermore, to the extent that I have included copyrighted material that surpasses the bounds of fair dealing within the meaning of the Canada Copyright Act, I certify that I have obtained a written permission from the copyright owner(s) to include such material(s) in my thesis.

I declare that this is a true copy of my thesis, including any final revisions, as approved by my thesis committee and the Graduate Studies office, and that this thesis has not been submitted for a higher degree to any other University or Institution.

## **Abstract**

Low-temperature waste heat recovery employs condensing heat exchangers to recover both sensible and latent heats. Due to the condensation of flue gases within these heat exchangers, they are subjected to severe corrosion. Perfluoroalkoxy (PFA) has been applied as a barrier layer on the surfaces of these heat exchangers for the prevention of corrosion. However, PFA has exhibited poor thermal properties and durability, which are requirements in low-temperature heat recovery applications. In this thesis, carbon-based nano-materials (8 nm and 60 nm thickness graphene particles and multi-walled carbon nanotubes, MWCNT) were incorporated into fluoropolymer (PFA) powders to generate thermally conductive and corrosion resistant composites as heat exchanger coatings. The microstructure, thermal conductivity, electrical conductivity of these composites were characterized. It was found that the thermal conductivities of the graphene-filled composites were significantly higher than that of the virgin PFA, i.e. approximately 8 times, while the composites containing MWCNT particles exhibited minimal improvement in thermal properties. The coatings containing both grades of graphene exhibited good surface finish and coating adhesion, good wear resistance and excellent corrosion resistance. The MWCNT-filled composites showed poor surface finish, resulting in poor corrosion resistance.

## **Dedication**

This study is dedicated to my beloved parents, Jacob and Karen Cierpisz, and brother, Dustin Cierpisz, who have provided me with a great deal of support throughout my academic career. Without them, I would not be the person I am today.

## **Acknowledgements**

I would first like to thank my advisors Dr. A. Edrisy and Dr. Y. He for their supervision, guidance, and assistance throughout the entirety of this project.

I would also like to thank my committee members Dr. R. Riahi and Dr. M. Mirhassani for attending my presentations and reviewing my thesis. Additionally, their input directly benefitted my work during this project.

The funding for this study was provided by Natural Resources Canada through the Program of Energy Research and Development, and by NanoPhyll Inc. Gratitude is provided to Raul Santos, Dan Walsh, Ruby Zhang, Chao Shi, Tyler Smith, Renata Zavadil and Maciej Podlesny for their assistance in experimentation and material characterization.

I am also grateful to the members of my research group, who have been extremely helpful throughout this project.



## Table of Contents

Declaration of Co-Authorship.....	iii
Abstract.....	v
Dedication.....	vi
Acknowledgements.....	vii
List of Figures.....	x
List of Tables.....	xvi
Chapter 1. Introduction.....	1
1.1 Background and Motivation.....	1
1.2 Objectives.....	1
1.3 Organization of Thesis.....	2
Chapter 2. Literature Review.....	3
2.1 Introduction.....	3
2.2 Corrosion Mechanism in Flue Gas Condensation.....	4
2.3 Problems Caused by Corrosion.....	7
2.4 Polymer Coatings.....	9
2.5 New Coating Development: Graphene and CNT.....	17
2.6 Coating Deposition.....	19
2.7 Thermal Conductivity of Composite Coatings.....	21
2.8 Electrical Properties of the Polymeric Materials.....	23
2.9 Mechanical Properties of the Composite Coatings.....	25
2.10 Purpose of Research.....	27
Chapter 3. Experimental Procedure.....	28
3.1 Materials.....	28
3.2 Compression Moulding of Composite Coupons.....	29
3.2.1 Hot Pressing of Disks.....	29
3.2.2 Sectioning of the Disks.....	30
3.2.3 Thermal Property Measurements.....	30
3.2.4 Electrical Property Measurements.....	30
3.3 Composite Coatings.....	31

3.3.1 Electrostatic Powder Spray Coating .....	31
3.3.2 Microscratch Testing .....	33
3.3.3 Wear Testing.....	33
3.4 Microscopy.....	34
Chapter 4. Results .....	36
4.1 Compression-moulded Composite Disks .....	36
4.1.1 Microstructure of the Compression-Moulded Disks .....	36
4.1.2 SEM of Composite Disks .....	41
4.2 Thermal Measurements .....	46
4.2.1 Specific Heat Measurements .....	46
4.2.2 Laser Flash Results.....	49
4.2.3 Thermal Conductivity Results .....	51
4.3 Electrical Resistivity Measurements .....	55
4.4 Fluoropolymer Composite Coatings .....	57
4.4.1 Optical Microscopy of Fluoropolymer Composite Coatings .....	57
4.4.2 Scratch Testing of Composite Coatings .....	63
4.4.3 Surface Roughness .....	67
4.4.4 Wear Testing.....	68
4.4.5 Corrosion Test .....	81
Chapter 5. Discussion .....	84
5.1 Composite Disks .....	84
5.2 Composite Coatings .....	89
Chapter 6. Conclusions .....	95
6.1 Conclusions .....	95
6.2 Recommendations .....	97
References.....	98
Vita Auctoris.....	105

## List of Figures

Figure 1. Effect of tube temperature on corrosion rate of low-temperature heat exchangers [3].	6
Figure 2. Erosion-corrosion attack (left) and corrosion-fatigue attack (right) on heat exchanger tubes [5].	8
Figure 3. Optical micrograph (A) of the surface of an E-coated aluminium fin showing a defect and polarization curve in 3.5% NaCl solution (B) performed on the area indicated by the circle in the micrograph (200- $\mu$ m diameter) [6].	10
Figure 4. Optical micrograph (A) of the surface of an aluminum fin painted with polyurethane potentiodynamic coating containing metallic pigments and potentiodynamic polarization curve in 3.5% NaCl solution (B) performed on an area with thick coating and on one not uniformly coated [6].	11
Figure 5. Electrochemical measurements as a function of time: EIS charge transfer resistance and electrochemical noise resistance [7].	12
Figure 6. Tube wall heat transfer in gas-water heat exchanger [2].	13
Figure 7. SEM microscopic observations of the cross-sections of coated coupons. The areas in the SEM photos from left to right: metal, primer, PFA, and epoxy [2].	15
Figure 8. Thermal properties of graphite-filled PFA at various temperatures: (a) thermal diffusivity, (b) thermal conductivity [10].	16
Figure 9. Graphene sheet showing coordinate system, lattice basis vectors, and position vector. Circles denote the positions of carbon atoms [11].	17
Figure 10. Curing schemes used for the primer and top coatings [10].	21

Figure 11. Electrical conductivity vs. $\phi_{H15}$ , indicating the electrical percolation threshold, for graphene-filled epoxy composite [17].....	24
Figure 12. Hot press setup (left) and the temperature controller (right). .....	29
Figure 13. The Pro-4 Four-Probe system for surface resistivity measurements.....	31
Figure 14. Preparing the substrate for electrostatic spray coating. ....	32
Figure 15. Samples hung on the stand for spray coating. ....	33
Figure 16. AO-2 Graphene/AC-5600 PFA Composite 5% by weight 100x Magnification (a), binary filter (b). ....	36
Figure 17. AO-2 Graphene/AC-5600 PFA Composite 100x Magnification (a) 5wt%, (b) 10wt%, (c) 14wt%, and (d) 20wt%.....	37
Figure 18. AO-4 Graphene/AC-5600 PFA Composite 100x Magnification (a) 5wt%, (b) 10wt%, (c) 14wt%, and (d) 20wt%.....	38
Figure 19. MWCNT/AC-5600 PFA Composite 100x Magnification (a) 1wt%, (b) 5wt%, (c) 10wt%, (d) 14wt%, and (e) 20wt%. ....	39
Figure 20. Area fraction of the filler material with respect to the weight fraction of the filler material within the compression-molded composite materials.....	40
Figure 21. SEM images of AO-2 Graphene 1wt%: (a) 80x, (b) 2,000x, (c) 10,000x.....	42
Figure 22. SEM images of AO-2 Graphene 10wt%: (a) 80x, (b) 2,000x, (c) 10,000x....	42
Figure 23. SEM images of AO-2 Graphene 20wt%: (a) 80x, (b) 2,000x, (c) 10,000x....	43
Figure 24. SEM images of AO-4 Graphene 1wt%: (a) 80x, (b) 2,000x, (c) 10,000x.....	43
Figure 25. SEM images of AO-4 Graphene 10wt%: (a) 80x, (b) 2,000x, (c) 10,000x....	43
Figure 26. SEM images of AO-4 Graphene 20wt%: (a) 80x, (b) 2,000x, (c) 10,000x....	44

Figure 27. SEM images of MWCNT 1wt%: (a) 80×, (b) 2,000×, (c) 10,000×. ....	44
Figure 28. SEM images of MWCNT 10wt%: (a) 80×, (b) 2,000×, (c) 10,000×. ....	44
Figure 29. SEM images of MWCNT 20wt%: (a) 80×, (b) 2,000×, (c) 10,000×. ....	45
Figure 30. Heat Capacity of PFA AO-2 Graphene Composites (Ratio Method) .....	46
Figure 31. Heat Capacity of PFA AO-2 Graphene Composites (ASTM E1269).....	47
Figure 32. Heat Capacity of PFA AO-4 Graphene Composites (Ratio Method). ....	48
Figure 33. Heat Capacity of PFA MWCNT Composites (Ratio Method).....	48
Figure 34. Thermal Diffusivity of PFA AO-2 Graphene Composites $\sigma = 0.022\text{mm}^2/\text{s}$ . $\sigma$ denotes standard deviation of thermal diffusivity.....	50
Figure 35. Thermal Diffusivity of PFA AO-4 Graphene Composites $\sigma = 0.018\text{mm}^2/\text{s}$ . ..	50
Figure 36. Thermal Diffusivity of PFA MWCNT Composites $\sigma = 0.015\text{mm}^2/\text{s}$ . ....	51
Figure 37. Thermal Conductivity of PFA AO-2 Graphene Composites $\sigma = 0.044\text{mm}^2/\text{s}$ .	52
Figure 38. Thermal Conductivity of PFA AO-4 Graphene Composites $\sigma = 0.036\text{mm}^2/\text{s}$ .	53
Figure 39. Thermal Conductivity of PFA MWCNT Composites $\sigma = 0.025\text{mm}^2/\text{s}$ . ....	53
Figure 40. Electrical surface resistivity of filled PFA composites. Measurements were performed using a Pro-4 Four-Probe resistivity sensor at five locations on the surface of each compressed disk sample. ....	55
Figure 41. The cross-sectional optical microscopy image of PFA matrix – 10 wt% AO-2 graphene filler coating on steel substrate.....	58
Figure 42. AC-5600 PFA Composite with 1 wt % AO-2 Graphene Filler (left), binary view (right). ....	58

Figure 43. AC-5600 PFA Composite with 10 wt % AO-2 Graphene Filler (left), binary view (right).....	59
Figure 44. AC-5600 PFA Composite with 20 wt % AO-2 Graphene Filler (left), binary view (right).....	59
Figure 45. AC-5600 PFA Composite with 1 wt % AO-4 Graphene Filler (left), binary view (right). .....	59
Figure 46. AC-5600 PFA Composite with 10 wt % AO-4 Graphene Filler (left), binary view (right).....	60
Figure 47. AC-5600 PFA Composite with 20 wt % AO-4 Graphene Filler (left), binary view (right).....	60
Figure 48. AC-5600 PFA Composite with 1 wt % MWCNT Filler (left), binary view (right). .....	60
Figure 49. AC-5600 PFA Composite with 10 wt % MWCNT Filler (left), binary view (right). .....	61
Figure 50. AC-5600 PFA Composite with 20 wt % MWCNT Filler (left), binary view (right). .....	61
Figure 51 Coefficient of friction vs scratch distance in AO-2 Graphene Coating during microscratch testing. ....	63
Figure 52. Coefficient of friction vs scratch distance in AO-4 Graphene Coating during microscratch testing. ....	64
Figure 53. Secondary electron SEM images of (a) the scratch track on the surface of AO-2 graphene composite coating, the enclosed area “b” indicates where closer inspection was performed; (b) higher magnification image of area “b” in Fig. 10(a), displaying a tear in	

the coating; (c) the scratch track on the surface of AO-4 graphene composite coating, the enclosed area “d” indicates where closer inspection was performed; (d) higher magnification image of area “d” in Fig. 10(c), displaying elongated fibers leading to a tear in the coating..... 65

Figure 54. SEM BSE images of scratch tracks at end of scratch of AO-2 graphene filled PFA coating (left), and AO-4 graphene filled PFA coating (right). ..... 66

Figure 55. Scratch depth analysis of AO-2 grade graphene filled PFA composite coating at maximum scratch load. .... 67

Figure 56. Scratch depth analysis of AO-4 grade graphene filled PFA composite coating at maximum scratch load. .... 67

Figure 57. Wear track of 20wt% AO-2 filled composite performed at ambient conditions. .... 68

Figure 58. Wear track of 20wt% AO-2 filled composite performed at 200°C. .... 69

Figure 59. Wear track of 20wt% AO-4 filled composite performed at ambient conditions. .... 69

Figure 60. Wear track of 20wt% AO-4 filled composite performed at 200°C. .... 69

Figure 61. Analysis of wear scar at selected point perpendicular to wear direction in 14wt% AO-2 graphene sample undergoing ambient wear testing. .... 71

Figure 62. Analysis of wear scar at selected point perpendicular to wear direction in 14wt% AO-2 graphene sample undergoing wear testing at 200°C. .... 71

Figure 63. Volumetric wear rates of polymer composite coatings. .... 72

Figure 64. Coefficient of friction vs. sliding distance of wear test of 14 wt% AO-2 graphene-filled coating at ambient temperature. .... 73

Figure 65. Coefficient of friction vs. sliding distance of wear test of 14 wt% AO-2 graphene filled coating at 200°C. ....	74
Figure 66. Coefficient of friction vs. sliding distance of wear test of 20 wt% AO-2 graphene filled coating at ambient temperature. ....	74
Figure 67. Coefficient of friction vs. sliding distance of wear test of 20 wt% AO-2 graphene filled coating at 200°C. ....	75
Figure 68. Coefficient of friction vs. sliding distance of wear test of 14 wt% AO-4 graphene filled coating at ambient temperature. ....	75
Figure 69. Coefficient of friction vs. sliding distance of wear test of 14 wt% AO-4 graphene filled coating at 200°C. ....	76
Figure 70. Coefficient of friction vs. sliding distance of wear test of 20 wt% AO-4 graphene filled coating at ambient temperature. ....	76
Figure 71. Coefficient of friction vs. sliding distance of wear test of 20 wt% AO-4 graphene filled coating at 200 °C. ....	77
Figure 72. Counterface surface after wear testing performed at ambient conditions on coating containing 20 wt% AO-2 graphene. ....	79
Figure 73. Counterface surface after wear testing performed at 200°C on coating containing 20 wt% AO-2 graphene. ....	79
Figure 74. Counterface surface topography after wear testing performed at ambient conditions on coating containing 20 wt% AO-2 graphene. ....	80
Figure 75. Counterface surface topography after wear testing performed at 200 °C on coating containing 20 wt% AO-2 graphene. ....	80



## **List of Tables**

Table 1. Properties of Pure Graphene [12]. .....	17
Table 2. The properties of carbon nanomaterials [12], [40-42]. .....	28
Table 3. Weight Fraction and Area Fraction of Filler Materials in Polymer Matrix. ....	40
Table 4. Area fraction of filler materials within composite coatings. ....	61
Table 5. Surface roughness values of PFA composite coatings. ....	68
Table 6. The (a) AO-2 Grade Graphene, (b) AO-4 Grade Graphene, and (c) MWCNT samples after corrosion testing. ....	82

# **Chapter 1. Introduction**

## **1.1 Background and Motivation**

Waste heat recovery from low-temperature streams using condensing heat exchangers is becoming increasingly important with regards to energy efficiency in industrial processes. Condensing flue gases result in extremely corrosive solutions on the internal surfaces of the heat exchangers, leading to short life of heat exchange elements made of metallic materials. There is a need for a corrosion resistant, thermally conductive barrier coating to protect the heat exchanger from the corrosive environment, while maintaining high thermal transfer efficiency of the heat exchanger. Melt-processable polymers are generally corrosion resistant and can be readily coated onto metal surfaces, but they have poor thermal properties. The introduction of thermally conductive filler into polymer matrix would yield a coating suitable for this application. Carbon-based nanomaterials such as graphene have extremely high in-plane thermal properties and can be incorporated within a polymer matrix via powder mixture.

## **1.2 Objectives**

The objective of this research is to develop a corrosion resistant coating with improved thermal properties as compared to those in prior research. The viability of the coating will be determined through microstructural characterization, thermal and electrical testing, and durability analysis.

### **1.3 Organization of Thesis**

This thesis is organized into six chapters, including Chapter one which introduces the background information, motivation, and objectives of this research. The second chapter reviews relevant literature to determine a suitable experimental methodology. The third chapter outlines the experimental procedures performed during the research. The fourth chapter details the results obtained from the experimentation. The fifth chapter discusses the results and the associated theories. The sixth chapter concludes the study by summarizing the results and recommending directions for future investigation.

## Chapter 2. Literature Review

### 2.1 Introduction

With increasing concern on the efficiency of energy use, waste heat recovery has been recognized as an effective energy saving method in industrial processes. It has been demonstrated that approximately 20 to 50% of the energy consumed in industrial processes in North America is lost via waste heat in the form of exhaust fluids [1]. It is also estimated that about 60% of this waste heat is low grade (temperatures below  $\sim 232^{\circ}\text{C}$ ) [2], and is rarely recovered. Materials and technologies that can assist the recovery of this waste heat have been developed, which can considerably increase the energy efficiency in these processes. During the recovery of waste heat from the exhaust fluids, heat exchangers are indispensable devices for the transfer of the heat (energy) contained in the fluids to usable energy. These heat exchangers are usually made of metallic materials such as carbon steels, aluminum, stainless steels, copper, etc. However, these metals tend to fail rapidly in the exhaust fluids, due to the severe chemical attack which is induced by the cooling of the fluids to below the dew points (condensing). Although exotic metals such as titanium, nickel, niobium, zirconium, tantalum, etc. may last longer in such corrosive environment, the extremely high cost of these metals prevents their economical use in waste heat recovery application.

When industrial fuels such as oil, coal and natural gas are burnt,  $\text{SO}_3$  can be generated in the flue gases since these fuels all contain sulfur. If the flue gases are kept above the dew points, corrosion may not occur. However, in order to effectively recover both the sensible and latent heats, the low-grade flue gases are usually cooled to below the

dew points, which leads to the generation of very corrosive sulfuric acid (condensation). Within the fluid gases, fly ash may also be observed, especially when a solid fuel (coal) is burnt. Viscous substances may be present as well, resulting from condensed salts. These may deposit on the surfaces of the heat exchange elements (fouling) or may damage the elements through erosion. This work will focus on the resistance of sulfuric acid produced in the condensation of the flue gases. The fouling and erosion resistance may be reflected by the smoothness of the coating and the wear resistance of the composite.

Corrosion occurs within these heat exchangers due to the decrease of the temperature of the flue gas. Condensation occurs when the walls of the heat exchange elements reach a temperature below the dew points of the flue gases. When this temperature is reached, sulfuric acid and water vapour within the flue gas condense on the surface of the exchange element, resulting in the corrosion of the heat exchanger. This process is important to understand and avoid, as the corrosion of the surfaces exacerbates the issues of material deposition (fouling) from the fly ash and viscous substances, which greatly reduces the heat transfer efficiency of the heat exchanger.

## **2.2 Corrosion Mechanism in Flue Gas Condensation**

In power plants that burn fossil fuels such as coal or oil,  $\text{SO}_2$  is first generated, which is further oxidized to form  $\text{SO}_3$ .  $\text{SO}_3$  then reacts with water vapour to form  $\text{H}_2\text{SO}_4$  vapour. The volume fraction of this vapour is usually 1-50 ppm within the flue gas, thus the acid dew point of this flue gases is in the range of 129 °C to 147 °C [3]. On the other hand, the water vapour dew point is usually much lower, i.e. around 60 °C. When the water dew point is reached, the  $\text{H}_2\text{SO}_4$  vapour will condense on the surfaces of the heat exchange

elements (but with very little water), resulting in highly concentrated sulphuric acid (80%, with pH ~2), which attacks the heat exchange elements. If the flue gas temperature is to be cooled below the water dew point (to maximize the recovered heat), this corrosion tends to be unavoidable, as it is associated with both the wall temperature of the heat exchanger and the condensation rate of the acid.

Figure 1 shows the general relationship between the corrosion rate on the surface of the heat exchanger and the temperature of the heat exchanger walls. It is seen that once the dew point temperature of the sulphuric acid is reached, condensation of the  $H_2SO_4$  starts, yielding an increase in the corrosion rate. As the temperature continues to decrease, the amount of condensed acid increases, leading to a rapid increase in corrosion rate. It can be seen that a maximum corrosion rate is achieved approximately  $30^{\circ}C$  to  $50^{\circ}C$ , which then decreases with decreasing wall temperature. The limiting factor of the corrosion rate is no longer the acid concentration at this point. At this temperature, the acid condensation is sufficient enough, and will no longer yield an increase in corrosion with an increase in condensation. The rate of corrosion then becomes dependent on the temperature of the wall, resulting in a decrease in the rate of corrosion. When the dew point of water within the flue gases is reached, the water vapour condenses and then combines with more  $SO_2$  present in the flue gases, yielding sharp increase in the concentration of  $H_2SO_3$ , resulting in a significant increase in the corrosion of the heat exchanger walls.

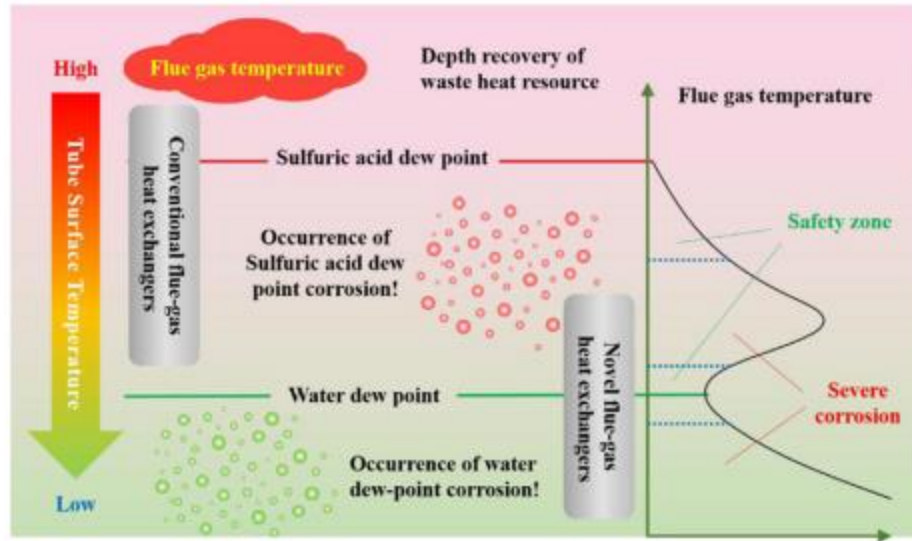


Figure 1. Effect of tube temperature on corrosion rate of low-temperature heat exchangers [3].

The type of corrosion that is present within the heat exchangers has been studied thoroughly in [4]. The process is known as de-alloying, which involves the selective removal of one of the components from the alloy. The removed material acts as an anode with respect to the other.

The other issue that is present in these materials is fouling. The buildup of the fly ash on the surfaces of the heat exchangers may lead to an increase in the corrosion in several ways. The first is a blockage that is generated in this way may lead to an increase in the flue gas velocity. With an increase in the velocity of the flue gases, the corrosion within the heat exchanger is increased. In addition, chemical reactions can occur between the deposited material on the surfaces of the heat exchangers and the metal itself. The reactions may also lead to the degradation of the material, resulting in the required replacement or maintenance of the heat exchanger, reducing the overall efficiency of the process.

Erosion of the material may also occur within the heat exchangers due to the flowing fly ash particulates. The erosion may lead to crevices and cracks in the surface of the heat exchanger. These cracks and crevices can be filled with pockets of sulfuric acid mentioned previously. The stagnant sulfuric acid within the crevice and a flowing gas outside of the crevice leads to what is known as crevice corrosion. Thus, it is possible for the internal structure of the metal to be corroded along with the surface due to general corrosion.

There are many interacting systems within the heat exchangers that lead to significant corrosion of the material, such as dealloying, fouling and erosion. These mechanisms lead to damage of the heat exchanger, worsening their lifespan

### **2.3 Problems Caused by Corrosion**

The main issues that are caused from the corrosion of the heat exchangers include the decrease of heat recovery rate, the damage to the heat exchanger, and the need to repair or replace the heat exchangers. The cost of repairing and replacing the heat exchanger material that is lost or damaged due to corrosion may exceed the profits acquired through the waste heat recovery. If the corrosion is severe enough, failure of the heat exchanger may occur, resulting in significant damage that would no longer be localized to the surfaces of the heat exchange elements. Corrosion leads to the thinning of the surface wall, which may then result in the buckling of the heat exchanger. In order to repair the damage that is generated through this process, considerable expenses are required. Thus, the corrosion present in the waste heat recovery process of low-temperature heat exchangers causes many issues that are not easily resolved.



The erosion phenomenon in heat exchangers of this type leads to other issues that can make the treatment of the corrosion even more difficult. Coating a corrosion resistant material onto the surfaces of the heat exchange elements is one of the methods adopted. It is important to note that the coatings used may include polymeric materials, due to their high corrosion resistance. However, polymeric coatings are much softer than ceramics or metals, and thus are more susceptible to erosion. Failure of the heat exchanger is not solely caused by general corrosion, and it may be due to pitting, galvanic attack, or crevice corrosion attack. Mechanical failure or damage may also lead to significant increase in corrosion, which has been mentioned previously in the form of erosion. Another form of combined failure is corrosion-fatigue failure. Vibrations in machinery or vibrations due to fast flowing liquids or gases may lead to fatigue stresses. These stresses may result in the formation of cracks within the walls of the heat exchange elements, as well as damaging the protective layer that may have been applied to resolve the corrosion issues. These cracks can lead to increased localized corrosion, much in the same way that erosion does. Images of tubes that have undergone these types of combined failure are displayed in Figure 2.

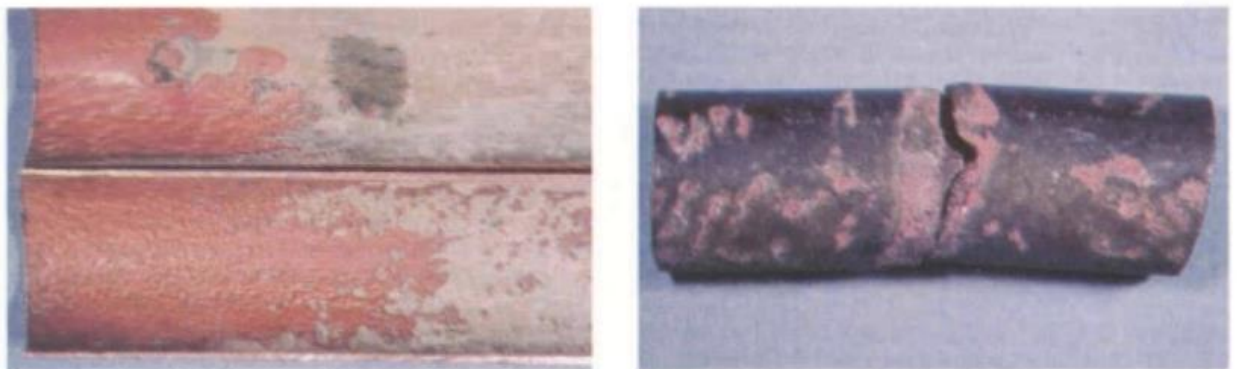


*Figure 2. Erosion-corrosion attack (left) and corrosion-fatigue attack (right) on heat exchanger tubes [5].*

In order to combat the corrosion present within these heat exchangers, the use of a polymer matrix composite coating has been attempted in the past. The issue that arises in using polymers as a heat exchanger material is that the temperature in the heat exchangers usually exceeds the maximum operating temperatures of commonly used polymers.

Since traditional metals experience damage to their surfaces due to corrosion, they are not suitable for prolonged use in low temperature heat exchangers. The use of polymer coatings as a corrosion resistant barrier on these metals may provide the desired properties.

## **2.4 Polymer Coatings**

The application of this research work is marginally different from the topic of industrial waste heat recovery. However, it involves the reduction or elimination of corrosion in heat exchangers, so the data derived from Ref. [6] applies to the current topic. The heat exchangers were designed for applications in the HVAC/R field, with copper tubes and aluminum fins. Fedrizzi et al. [7] performed testing on two different coatings for aluminum heat exchangers. The first of these coatings is an E-coating (epoxy resin), which has a glass transition temperature of 100 °C. The other was a polyurethane coating containing metallic (aluminum) pigments, which has a glass transition temperature of 160 °C. Figures 3 and 4 show the polarization curves of both coatings.

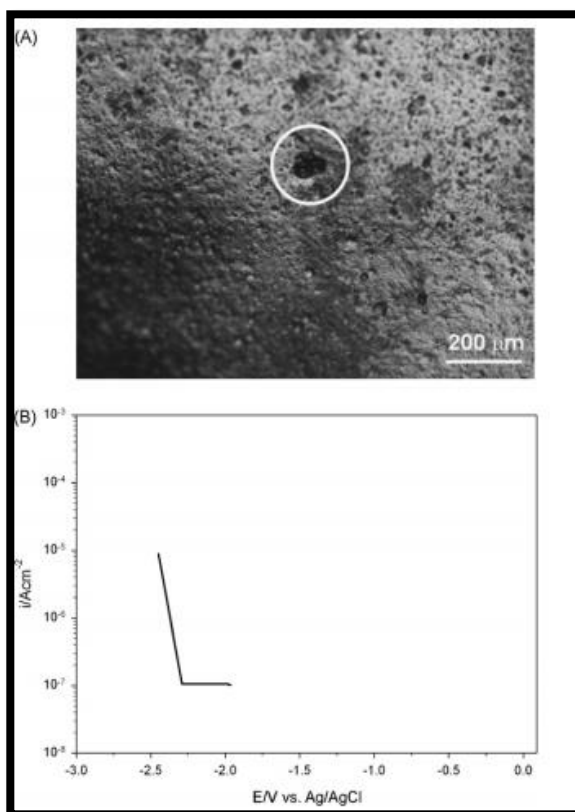


Figure 3. Optical micrograph (A) of the surface of an E-coated aluminium fin showing a defect and polarization curve in 3.5% NaCl solution (B) performed on the area indicated by the circle in the micrograph (200- $\mu\text{m}$  diameter) [6].

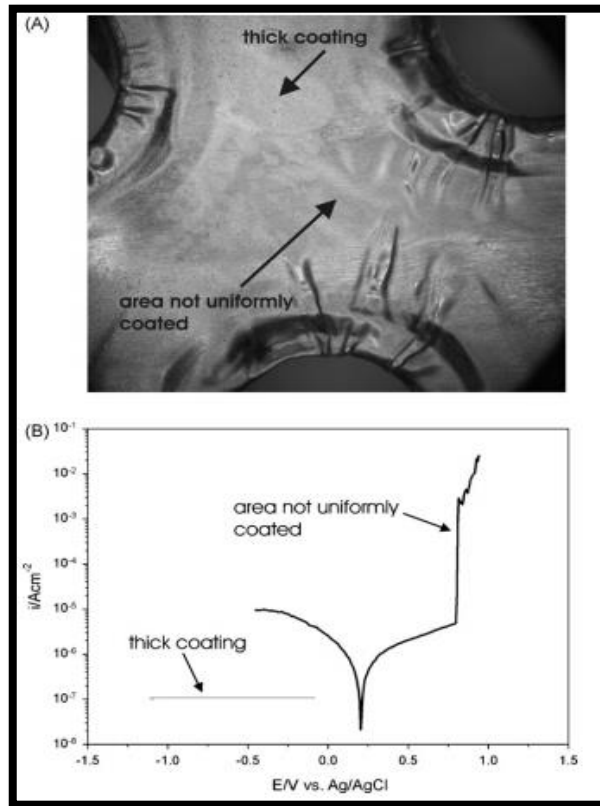


Figure 4. Optical micrograph (A) of the surface of an aluminum fin painted with polyurethane potentiodynamic coating containing metallic pigments and potentiodynamic polarization curve in 3.5% NaCl solution (B) performed on an area with thick coating and on one not uniformly coated [6].

It was determined that the epoxy coating has uniform thickness and provides good coverage of the aluminum fins. A few defects were observed including pinholes, but the majority of the coating provided good coverage for corrosion resistance. Impedance measurements that had been carried out on the E-coating show that this coating provides good barrier properties. The polyurethane coating, however, did not provide uniform coverage, as the spray process did not allow for the complete coverage of the aluminum fins behind the copper tubes. Thus, the corrosion resistance of this coating is impaired due to the zones in which the coating was not completely covering the aluminum fins.

Research on hydrophobic coatings has also been performed to assist in the reduction of corrosion in heat exchanger applications. Dhama et al. [7] focused on the application of heat exchangers in geothermal power plants. In geothermal power plants, the heat exchangers are in contact with highly corrosive fluids, which results in the deposition of fluid salts onto the tube walls, resulting in corrosion. The usage of hydrophobic coatings may assist the reduction of the deposition and therefore corrosion of the heat exchangers. Two coatings were utilised in this paper. The first coating was perfluoro ethyltriethoxysilane, in which aluminum substrates were dip coated.

Electrochemical analyses were performed on these coatings (electrochemical impedance spectroscopy). Figure 5 displays the results of these tests, which indicated that similar patterns for both coatings were present. After approximately 720 h immersion, a decrease was observed for both techniques, which suggests an increase in the corrosion rate for the coatings that were tested. The study concluded that good coating behaviour was observed through this experimentation.

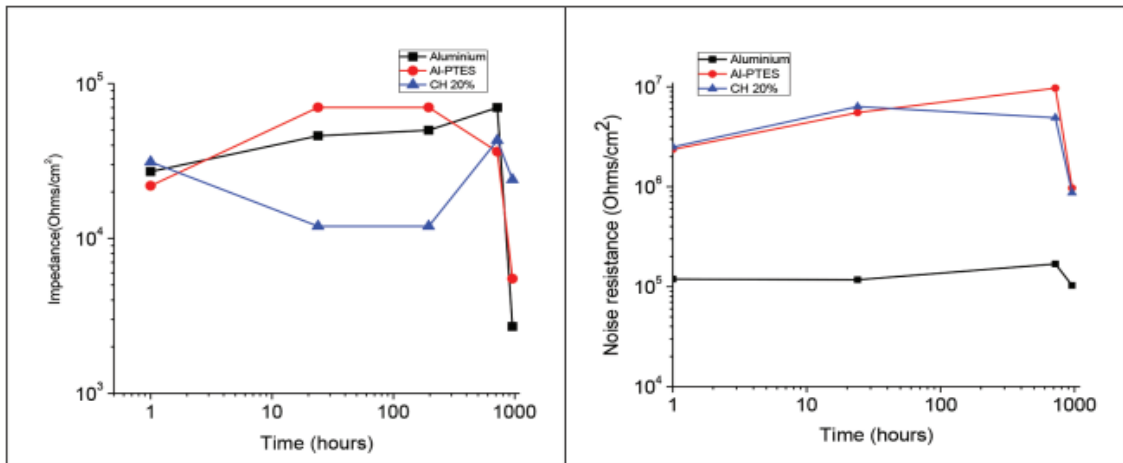


Figure 5. Electrochemical measurements as a function of time: EIS charge transfer resistance and electrochemical noise resistance [7].

These coatings were not used in the application presented at the beginning of this paper (waste heat recovery), so it is unknown how these coatings would be affected by the presence of fly ash and particulates in the flue gases. It is also important to note that no operating temperature was given in this research, so it is unknown if these coatings may be applicable to the recovery of waste heat. It is, however, important to discuss all possible solutions to the problem, and these hydrophobic coatings appear to be one possible solution.

Thermal resistance measurements of the wall of the heat exchanger were performed, where the separate measurements corresponding to layers within the heat exchanger tube wall are shown in Figure 6. The values indicate that the resistance of the gas side film is higher than that of the PFA coating, meaning that the resistance of the polymer coating may not yield a significant reduction in the overall heat transfer process.

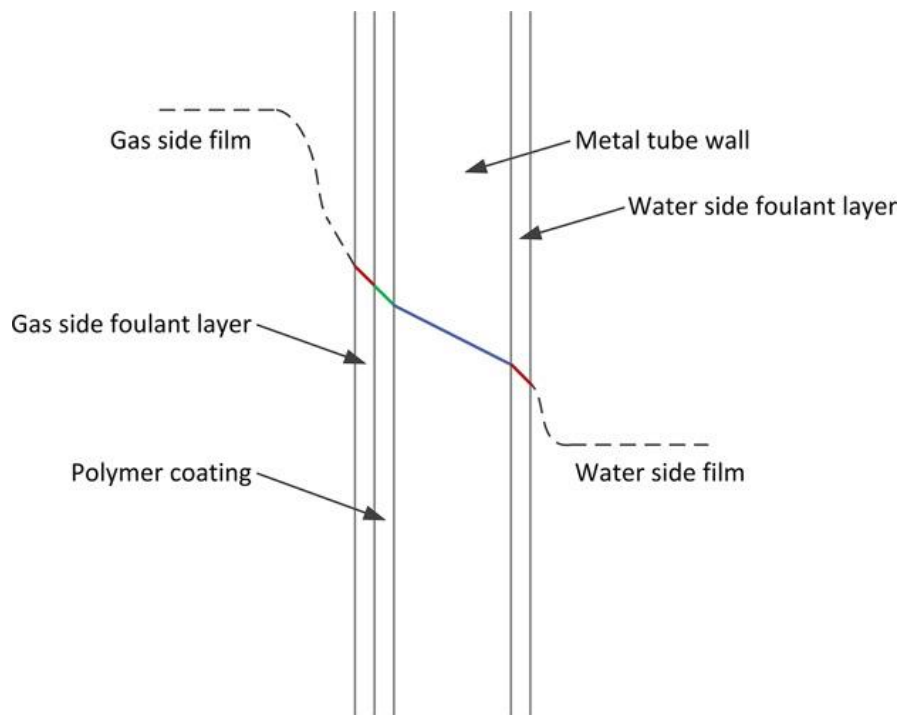


Figure 6. Tube wall heat transfer in gas-water heat exchanger [2].

Fluoropolymers are used in a wide range of industries, and have excellent corrosion resistance [8]. Several fluoropolymers have been tested for their corrosion resistance. Of those tested by Leivo et al., only PFA (perfluoroalkoxy alkane) had a maximum operating temperature above the temperatures experienced in low-temperature heat exchangers. PFA is also fully fluorinated, resulting in strong bonding between the carbon and fluorine atoms, which results in excellent corrosion resistance.

PFA has been employed as a coating material for heat exchangers used in low-temperature waste heat recovery [9], [10]. PFA has excellent corrosion resistance and is able to produce smooth and pin-hole free coatings due to its melt-processable nature. Although its thermal conductivity is only 0.195 W/mK, it can be compounded with other materials to improve the thermal properties [10]. While most polymers have a glass transition temperature or melting point below the earlier stated 232°C temperature of the low-grade flue gas, PFA has a maximum operating temperature up to 260°C. Due to these, PFA is an interesting polymer that may be able to solve the issues present in the corrosive environment.

PFA can be applied electrostatic powder coating [9] or by aqueous spray coating [2]. For aqueous PFA coating, aluminum coupons were coated with a thin layer of primer, followed by an aqueous PFA (30 wt%) layer [2]. A second PFA layer was applied after air-drying. The coating was then cured at 370 °C - 400 °C for 10 minutes. The coated samples, as well as other types of materials as reference, were submerged in 20 wt% sulfuric acid at 50 °C (ASTM G31). It was found that the PFA-coated samples had a significantly reduced corrosion rate than stainless steel and was comparable to the samples made of Inconel and Hastelloy. It is important to note the thickness of each of the applied

layers of coating for these types of applications. Figure 7 shows SEM images of the cross section of the coating. From left to right, these regions are the metal, the primer, PFA and epoxy (mounting material). The top-coat layer is dense and non-porous, which is favourable in this application. A coating containing pin holes would allow the corrosive substance to penetrate near to the substrate, resulting in limited lifespan of the heat exchanger. The primer coating remains a solid layer between the substrate and the top-coat, with a tight contact between them. The PFA-coated samples showed excellent corrosion resistance, surviving in a bath of 20% sulfuric acid at 50 °C with nearly no weight loss.

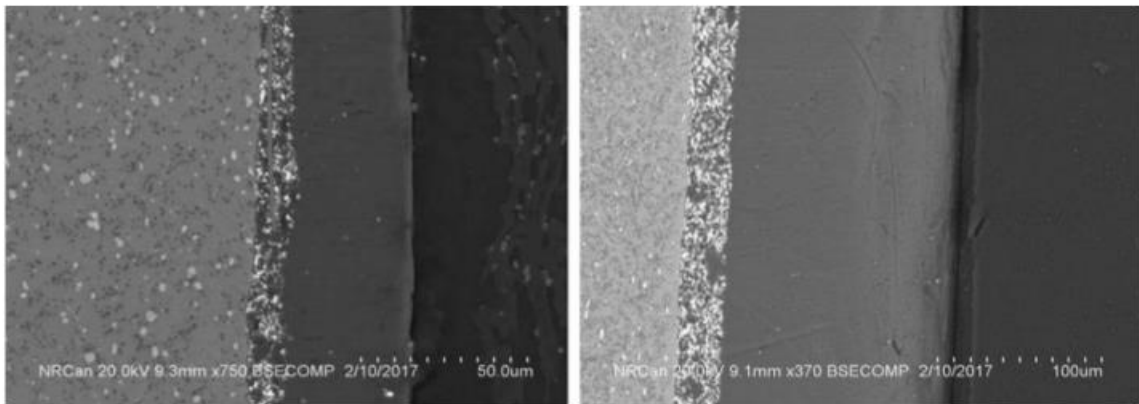


*Figure 7. SEM microscopic observations of the cross-sections of coated coupons. The areas in the SEM photos from left to right: metal, primer, PFA, and epoxy [2].*

The work by He et al. [10] has focused on the development of composite coatings of PFA with graphite filler. Graphite fillers at different weight fractions from 0 wt% to 50 wt% in 10 wt% increments were studied. Cyclic heating/cooling was performed on coated samples at 80% sulfuric acid solution for 1500 h. Thin coatings (<60  $\mu\text{m}$ ) without primer layer did not yield good results, showing blistering on their edges at approximately 100 hours. All samples with a thicker coating ( $\geq 140 \mu\text{m}$ ) and a primer layer yielded excellent



corrosion resistance (no weight change before and after corrosion immersion). Failure in higher weight fractions (greater than 30 wt%) was due to poor cross-linking of the polymer on the graphite particles. It was concluded that the PFA composite coating with electrostatic powder spray can be utilised to avoid corrosion in these heat exchangers. The thermal conductivities of the coatings are demonstrated in Figure 8 to show the applicability of these coatings in heat exchanger applications.

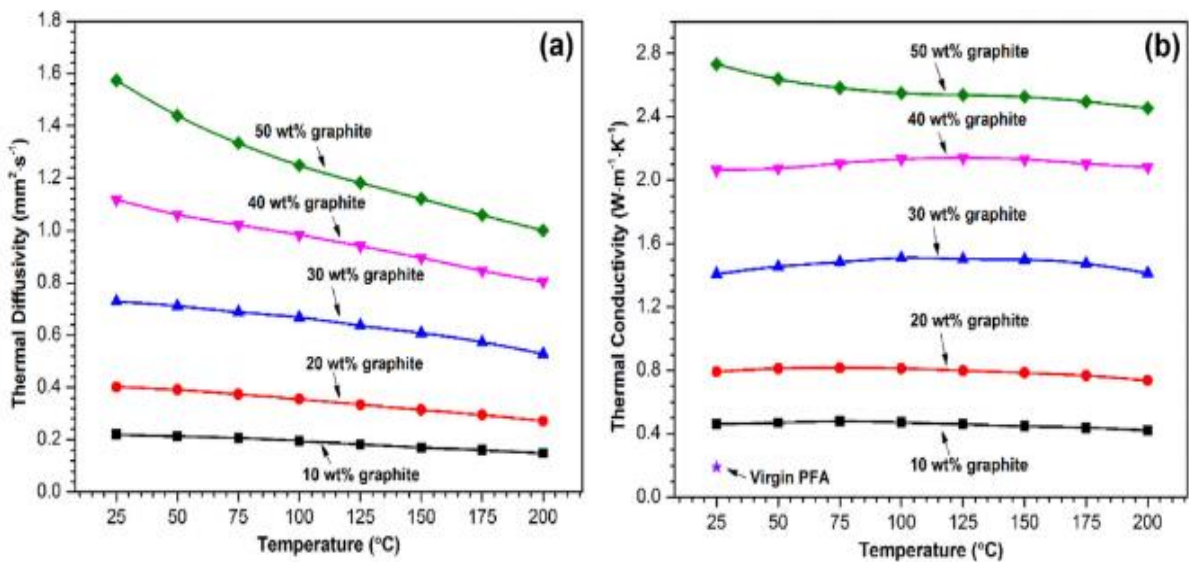


Figure 8. Thermal properties of graphite-filled PFA at various temperatures: (a) thermal diffusivity, (b) thermal conductivity [10].

Polymers have been applied to many substrates as barrier coatings for many different applications. They have been proven to generate cohesive, pinhole free coatings. Polymers tend to have low operating temperatures and very low thermal conductivities, excluding them from this application. However, some polymers such as PFA have been shown to have high maximum operating temperatures, and improvements can be made to their thermal conductivities with the inclusion of filler materials.

## 2.5 New Coating Development: Graphene and CNT

The introduction of filler materials to the PFA has been shown to yield significant increases in the thermal conductivity, which is a very important property in low-temperature heat exchanger applications. The use of nanomaterials, e.g. graphene, as filler may yield improved results compared to previous work with this polymer. Graphene is a one-atom thick sheet of  $sp^2$ -bonded carbon atoms in a honeycomb structure, as shown in Figure 9. Graphene exhibits extraordinary properties, making it highly attractive for use in many applications. Table 1 lists some of these properties.

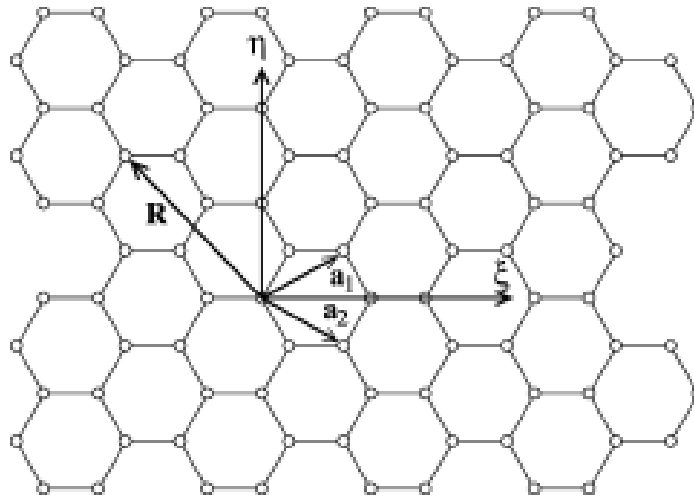


Figure 9. Graphene sheet showing coordinate system, lattice basis vectors, and position vector. Circles denote the positions of carbon atoms [11].

Table 1. Properties of Pure Graphene [12].

Properties	Values
Young's Modulus	$\sim 1100$ GPa
Fracture Strength	125 GPa
Thermal Conductivity	$\sim 5000$ W $m^{-1}$ K $^{-1}$
Mobility of Charge Carrier	$2 \times 10^5$ cm $^2$ V $^{-1}$ s $^{-1}$
Specific Surface Area	2630 m $^2$ g $^{-1}$

Many applications involving graphene take advantage of these properties to generate superior electrical devices such as supercapacitors. The thermal conductivity of graphene is significantly higher than those of the previously mentioned filler materials (e.g. graphite) utilised in previous studies [10].

It has been shown that a small amount of graphene filler added to a polymer matrix can yield significant increases in thermal, electrical and mechanical properties of the composite material[13]–[15]. However, it is important to note the difficulties in using graphene as a filler material. Reliably producing the same or a similar structure of matrix is important to achieve consistently high performance composites. However, due to the anisotropy of graphene flakes, as well as their wide range in sizes, this may be difficult without further orienting methods[14], [16]–[18]. In order to thoroughly mix the graphene and polymer, several methods have been developed. In a manner similar to the experimentation performed by He et al. [10], tumble mixing of the powders prior to coating application may be suitable. Other methods include the mixing and orienting the graphene within a liquid polymer through the use of a magnetic field [19], or a mixture in a water dispersion [20].

Another filler type that may be suitable for these applications is carbon nanotubes (CNT). Similar to graphene, CNTs exhibit excellent mechanical and electrical properties. However, they also exhibit anisotropy, yielding poor properties in the radial direction as well as between the tubes[20]–[22]. Carbon nanotubes can be regarded as simple sheets of graphene wrapped along an axis to form a cylinder. Depending on which axis is utilised, different types of carbon nanotubes are formed (zigzag along  $\xi$ -axis, armchair along  $\eta$ -axis,

and chiral not along either of them). These axes are displayed on the diagram of a sheet of graphene in Figure 9 [11].

Carbon nanomaterials have been shown to have extremely high theoretical thermal conductivities, which is an attractive property in a filler material within a polymer matrix for this application. These materials display anisotropy, and thus may prove difficult for use as filler materials.

## **2.6 Coating Deposition**

It is noted that there are several methods available to apply fluoropolymer coatings. The first of these methods is the wet spray of water-based dispersions of fluoropolymer resins onto the substrates. This process is followed by heat treatment to remove the water and form a smooth film [8]. This method has been discussed earlier in [18, 19]. Another method that has been tested is the use of a thermal spray coating, so the heat treatment steps can be avoided. However, this method requires careful temperature control to ensure stability in the coating after cooling. This method has been performed on PFA/MWCNT mixtures for electrical property measurement, and has been shown to be a viable coating method, with excellent dispersion and low percolation thresholds [23]. One final method discussed is that of electrostatic powder spray coating. This method involves the spray of mixed powder through an electrically charged gun towards a grounded workpiece. The powder sticks to the substrate and can be heated above the melting temperature of the polymer to ensure good crosslinking. This method was performed by He et al. [10] on PFA/Graphite composite coatings for low-temperature heat exchanger applications.

Electrostatic powder spray coating allows for complete coverage of a three-dimensional object, due to the attraction of the particles to the substrate through electrical charges. The powder particles are charged in the barrel of the spray gun, then ejected towards the work piece. Because the particles have negative charges, they are repelled from one another, which assists in the even distribution of the particles on the substrate. The charge also ensures that the particles do not remain in the air, as they are attracted to the grounded workpiece [24]. Electrostatic spray coating has a high transfer efficiency, allowing for coverage of a sample requiring less powder than conventional spray coating processes [25-27].

In real application, a primer coating was applied to the substrate by He et al. [10]. This was intended to give better adhesion to the substrate. The primer adheres to the substrate better than the top-coat, and ensures the adherence of the coating to the substrate. Poor adhesion may lead to failure of the coating, resulting in damage to the heat exchanger. The top-coat adheres to the primer coating better than the substrate due to the chemical bonding between the primer and top layers that occurs during the curing process. After electrostatic powder spray coating, a curing process is required to ensure a smooth, poreless coating. The curing scheme for the PFA/Graphite composite materials mentioned previously is displayed in Figure 10. This figure shows the curing process for both the primer coating (red) and the polymer matrix top coating (blue). All coating applications in this research work followed this curing process.

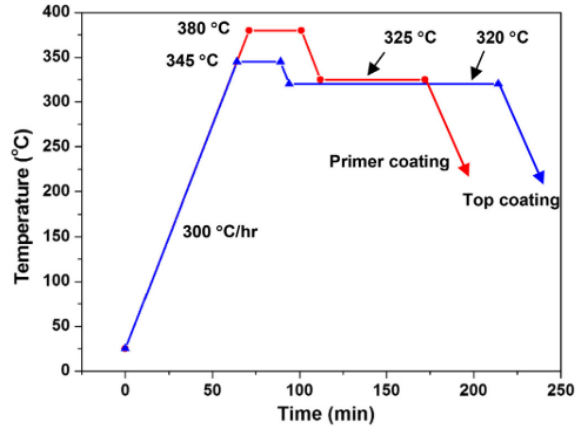


Figure 10. Curing schemes used for the primer and top coatings [10].

Several coating methods have been performed to apply polymer composite materials onto substrates. Wet-spraying can be utilised for water-based dispersions. Materials in powder form can be applied through the use of electrostatic spray coating. This is the process used in many studies involving the use of PFA as a barrier coating.

## 2.7 Thermal Conductivity of Composite Coatings

Polymers exhibit weak intermolecular forces between polymeric chains. Due to this, energy is not easily transferred through the material, resulting in poor thermal properties. This is why it is important to understand the relationship between polymer matrices and filler materials. Conductive polymers are polymer that exhibit much greater thermal and electrical conductivities than general polymers. However, these polymers tend to exhibit unstable conductive properties at varying temperatures. Given that the proposed application is above 200 °C, it is unlikely that conductive polymers will exhibit adequate properties, if they are even able to achieve those temperatures without degrading [28]. With respect to filler materials, the thermal properties of graphene and CNT have been discussed

previously, and it is clear that these filler materials provide the bulk of the pathways through which thermal conduction occurs.

An understanding of the process with which these thermal properties are characterised is also important. Thermal properties of the coatings generated by He et al. [10] were characterized through measurements of the thermal diffusivity ( $\alpha$ ) using laser flash analysis, and specific heat ( $C_p$ ) through differential scanning calorimetry. Disks of 12.7 mm in diameter and 2 mm in thickness were produced through hot pressing of tumble-mixed PFA/Graphite powders. These disks acted as substitutes for sections of coatings, as they contain close microstructure to the coating. These samples were utilised in the above-mentioned processes. The densities of these samples ( $\rho$ ) were also determined, and the values were utilised in Equation 1 to determine the thermal conductivity ( $\lambda$ ) of the composites.

$$\lambda = \rho C_p \alpha \quad (1)$$

The results of this experimentation have been shown in Figure 9 before. From this analysis, it can be determined that the thermal conductivity can be greatly increased with the addition of filler materials while maintaining cohesion and a smooth surface. It was shown that an increase in weight fraction yielded an increase in thermal conductivity in a near linear relationship. However, the authors noted that at high weight fractions (> 30 wt %), the composite tends to degrade due to poor cross-linking, as not enough polymer is present.

The laser flash analysis involves the use of a light source as a heat source, heating the bottom of a sample. A sensor at the top of the sample detects the time dependent

temperature rise. The full process was performed according to ASTM standards [29]. Differential scanning calorimetry was also performed according to ASTM standards [30]. The hot disk method is another method that has been utilised to determine the thermal conductivity of PFA composite coatings [31]. This method involves the introduction of a constant current to heat a sample, to determine the average temperature increase as a function of the characteristic time of the material [32].

Polymers display poor thermal conductivity due to their weak intermolecular forces. The introduction of filler materials such as graphite has proven to lead to an increase in their thermal conductivities. Improvement can be made on the thermal properties of these coatings with different filler materials.

## **2.8 Electrical Properties of the Polymeric Materials**

For the same reason that polymers have low thermal conductivities, they tend to have low electrical conductivities. Electrons are unable to transfer between polymer chains easily, often yielding little or no electrical conductivity. As mentioned previously, conductive polymers may yield better results for conductivity, but it is unlikely that they will remain stable at the proposed operating temperatures.

Electrical conductivity measurements of polymer-matrix graphene composites has been performed by some researchers [17]. Electrical conductivity measurements were conducted using a two-probe configuration on a square shaped sample. At filler loadings higher than 0.05 weight fraction, the electrical conductivity reaches its near maximum and plateaus with an increase in filler loading. Initially reaching this value, increases in the loading do have a mild effect on the electrical conductivity. However, this is only noticed



at loadings slightly higher than 0.05. Below this loading, the electrical conductivity changes drastically with slight changes to the filler loading. This point is known as the percolation threshold [33]. The formation of an electrically conductive network is reached at this loading, resulting in a significant increase in the electrical conductivity. With the formation of an electrically conductive network through the material, higher filler loadings will only yield slight increase in the electrical conductivity of the composites. This relationship can be observed in Figure 11.

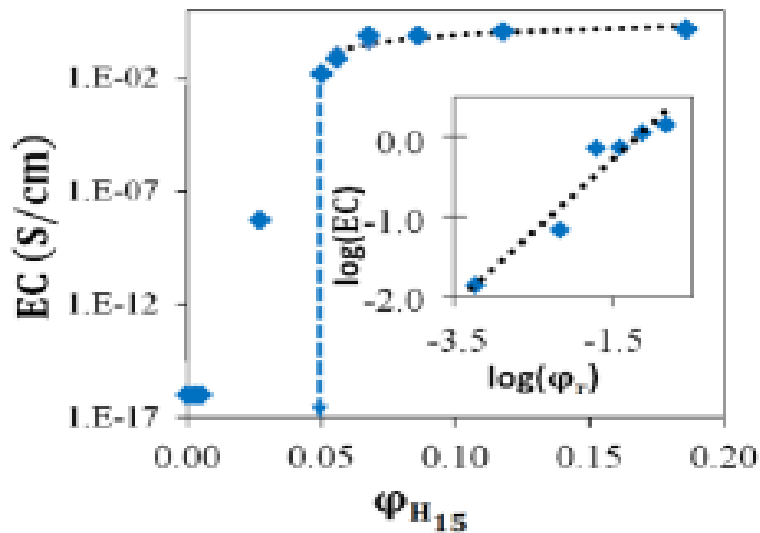


Figure 11. Electrical conductivity vs.  $\phi_{H15}$ , indicating the electrical percolation threshold, for graphene-filled epoxy composite [17].

By examining the structure of graphene and carbon nanotubes as shown in Figure 10, it is evident that both the thermal and electrical conductivities are high since the structure allows for a pathway for electrons to be transported along the material. As mentioned previously, both of these filler materials are anisotropic, as such, transfer of

electrons between layers of graphene or tubes of CNTs will be more difficult than along the lattices.

The electrical conductivities of polymers are low for similar reasons for their low thermal conductivities. The introduction of filler material leads to an increase in the electrical conductivity. At a critical filler loading, a percolation threshold is reached, leading to maximum conductivity. Filler loadings higher than this threshold yield very minimal increases to the electrical conductivity.

## **2.9 Mechanical Properties of the Composite Coatings**

Within the heat exchangers, the presence of particulates may impact the surfaces of the coatings as mentioned previously. Thus, characterization of the mechanical properties of these coatings is necessary [33, 34]. Prior research on a PFA matrix containing various ceramic fillers has been performed [36], and the fillers include boron nitride, silicon carbide, alumina and graphite. Considerable research has been conducted using scratch testing (with progressive load) on polymeric materials [9, 36, 37]. During the testing, a progressive load of 0-28 N was applied, with a lateral speed of 3 mm/min for a 3 mm length scratch. The coefficient of friction (COF) was evaluated using the measured frictional force ( $F_f$ ) and normal forces ( $F_N$ ) as:

$$COF = \frac{F_f}{F_N} \quad (2)$$

It was determined that graphite-filled composites yielded the lowest critical load for the onset of failure during scratch testing, attributed to the low extent of viscoelastic recovery of the composite material.

Wear testing is another common method of determining the durability of the coatings, as was performed in [35]. Ball-on-disk sliding tests were performed in dry (unlubricated) ambient conditions against a 6-mm diameter AISI 52100 steel ball using a Bruker's UMT machine. The applied load was 10 N with a sliding speed of 0.1 m/s. Weights of the samples and counter faces prior to and after testing were recorded to calculate the mass loss and wear rate. Frictional force was also recorded during testing and was used to determine the coefficient of friction. Similar to the scratch testing, of all the filler materials used, the graphite-filled composites showed the poorest performance.

Another method of determining wear rate is through the use of volumetric analysis. Polymers are more likely to be deformed than to be removed from bulk material, and as such, weight measurements of the samples before and after may not provide a clear picture as to the actual wear rate [38]. Thus, area analysis can be performed on a wear track at several points to determine the wear rate as:

$$\tilde{W} = A \times 2\pi R/s \quad (3)$$

where  $A$  is the average worn area taken from several measurements of the wear track,  $R$  is the radius of the wear track and  $s$  is the total sliding distance. With this equation, volumetric wear rate can be determined.

Particulates within the heat exchangers can result in the wear of the surface. If polymer barrier coatings are to be utilized, they must exhibit good durability. PFA was shown to have good adhesion between the matrix and the substrate, as well as good wear resistance.

## **2.10 Purpose of Research**

The aim of this research is to determine a viable composite coating containing a PFA matrix with nano filler materials (Graphene and MWCNT) for use in low-temperature condensing heat exchangers. Two grades of graphene filler and one grade of MWCNT filler are used in this research. The specific heat and thermal diffusivity (for the analysis of thermal conductivity) of the coatings as well as the electrical surface resistance are characterized. The microstructural cohesion of both compression-molded disks and composite coatings containing weight fractions varying from 1 wt% to 20 wt% are analysed. Methodology on coating generation and mechanical properties such as adhesion of the coating is also discussed.

## Chapter 3. Experimental Procedure

### 3.1 Materials

Neoflon AC-5600 PFA powder (Daikin, Inc.) was used as the polymer matrix. The powder has a nominal particle size of  $\sim 44 \mu\text{m}$  (325 mesh), a density of  $2.15 \text{ g/cm}^3$ , and thermal conductivity of  $0.25 \text{ W/mK}$  [39]. Three grades of carbon nano-powders were selected as the filler materials: AO-2 grade graphene, AO-4 grade graphene, and MW-CNTs. Their corresponding properties are listed in Table 2.

Table 2. The properties of carbon nanomaterials [12], [40-42].

Material Property	AO-2 Graphene	AO-4 Graphene	MW-CNT
Young's Modulus (GPa)	$\sim 1100$	$\sim 1100$	800-950
Fracture Strength (GPa)	125	125	63-150
Thermal Conductivity (W/mk)	<b><math>\sim 5000</math> (in-plane)</b>	<b><math>\sim 5000</math> (in-plane)</b>	<b><math>\sim 3000</math></b>
Specific Surface Area ( $\text{m}^2/\text{g}$ )	$> 15$	$\leq 40$	-
Diameter (nm)	-	-	50 - 85
Length ( $\mu\text{m}$ )	-	-	10 - 15
Average particle size ( $\mu\text{m}$ )	$\sim 5$	$\leq 7$	-
Average flake thickness (nm)	8	60	-
Bulk Density ( $\text{g/cm}^3$ )	2.267	2.267	0.230

The composites were prepared by adding various fractions of (1-20 wt%) the carbon nano-powders into the PFA powder. The filler and polymer powders were mixed at room temperature for 1 hour using a laboratory Inversina Tumbler Mixer (Bioengineering Inc.). Samples for thermal and electrical property measurements were prepared using compression moulding method: disks with dimensions of  $\Phi 32 \text{ mm} \times 2 \text{ mm}$  were formed and then sectioned. Stainless steel (SS 316) coupons were prepared, and the powder mixtures were electrostatically spray coated onto these substrates according to prior work [10]. The coupons are  $60 \text{ mm} \times 35 \text{ mm} \times 3 \text{ mm}$  in size and a total coating thickness

(including primary layer) of about 200-250  $\mu\text{m}$  was applied. All the sample preparation and coating application were completed in CanmetMATERIALS' Hamilton laboratory.

## 3.2 Compression Moulding of Composite Coupons

### 3.2.1 Hot Pressing of Disks

A hot-pressing process (compression moulding) was utilized to produce the composite coupons. The mixed composite powder was first loaded into a mould which could be heated while pressure was applied. The temperature of the mould was increased from room temperature to 350  $^{\circ}\text{C}$  (the melting point of the polymer is  $\sim 310$   $^{\circ}\text{C}$ ) within 1 hour, and held for 20 minutes to allow for complete melting. Pressure was gradually raised during heating, up to 10 MPa. The pressure was released at 300  $^{\circ}\text{C}$  and the sample was cooled within the mould to room temperature. The experimental setup for this process is shown in Figure 12.



*Figure 12. Hot press setup (left) and the temperature controller (right).*

### **3.2.2 Sectioning of the Disks**

The 32-mm-diameter disks were sectioned using a low speed diamond saw into two halves. One half was ground to form a smaller disk with a diameter of 12.7 mm for thermal diffusivity measurement using the laser flash method. The remainder of the sample was used for the specific heat measurement (differential scanning calorimetry), and for microstructure characterization under optical microscopy and scanning electron microscopy.

### **3.2.3 Thermal Property Measurements**

Differential scanning calorimetry was performed on the samples in order to determine the specific heat of the composite over a range of temperatures (25 to 250 °C). Specific heat measurements were conducted according to the ASTM E1269 as well as the ratio method. ASTM E1269 analyzes the difference in heat flow into the test material and a reference material. The ratio method is specific to the software used for testing, and involves measurement comparisons in very small intervals throughout testing. Laser flash analysis was performed on the  $\Phi 12.7$  mm disks for the determination of the thermal diffusivity over the same temperature range. With these two values as well as the density of the composite materials, the thermal conductivity of the sample was determined using Equation 1. Comparison between the thermal conductivity of different filler materials at different weight fractions was performed.

### **3.2.4 Electrical Property Measurements**

Surface electrical conductivity of the composite coupon sample was determined through the use of a Pro-4 four probe resistivity measurement system shown in Figure 13.

These tests were performed on the  $\Phi 32$  mm disks before they were sectioned to the smaller disks. Five measurements were taken for each sample with an average value being obtained for the sample.

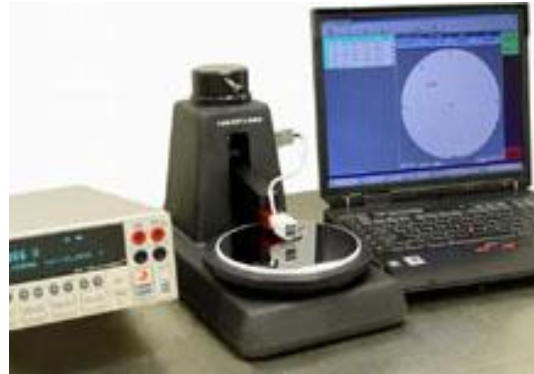


*Figure 13. The Pro-4 Four-Probe system for surface resistivity measurements.*

### **3.3 Composite Coatings**

#### **3.3.1 Electrostatic Powder Spray Coating**

SS316 stainless steel coupons were cut from a large steel plate (3 mm thick) into dimensions of 60 mm  $\times$  35 mm. These samples underwent several stages of grinding to remove all corners and edges to ensure that the coating process would allow the entire surface to be coated smoothly. The stages with which the substrates were prepared are shown in Figure 14. The rectangular samples were initially cut by waterjet, and then removed from the plate. The corners and the edges of the samples were then removed with a belt grinder and further rounded with 180 grit grinding pads. The samples were then sandblasted to remove any surface defects and create a rough surface for coating. The initial thicknesses of the samples were recorded, which were used to calculate the final thicknesses of the coatings after applying multiple layers of coating.





*Figure 14. Preparing the substrate for electrostatic spray coating.*

After cleaning in an ultrasonic bath and dried, the prepared substrates were hung on a sample stand in the manner displayed in Figure 15. A wire was connected to the stand to ground the samples to facilitate the electrostatic powder spray process. The stand was placed in a spray chamber so that over-sprayed powder can be recollected and reused. A primer powder (Daikin Neoflon ACP-5909BK) was first applied to the coupons, which allowed for better adhesion between the composite coating and the substrates. Through the spray gun, the powder was negatively charged and attracted to the grounded substrates. The samples (with the sprayed powder) were then removed from the stand and transported to an electrical furnace to cure the powder according to the scheme shown in Figure 10. Approximately 50  $\mu\text{m}$  of primer was applied to the substrates before the application of the top coating. Similar steps were used for the composite top coatings (mixtures of PFA powders with filler powders). These powders were also cured in the electrical furnace following a slightly different process to the primer coating as shown in Figure 10. The coating process was repeated until a topcoat thickness of approximately 150-200 microns was achieved.



*Figure 15. Samples hung on the stand for spray coating.*

### **3.3.2 Microscratch Testing**

Selected coatings (those with 20 wt % AO-2 and AO-4 grades graphene fillers) were chosen to undergo microscratch testing. Microscratch testing was performed under progressive loading (0-28 N) at a lateral speed of 1 mm/min over scratch tracks of 5 mm in length using a diamond Rockwell stylus (200-micron radius). The applied normal force as well as the frictional force were recorded during the testing. Using these values, the coefficient of friction (COF) was determined using Equation 2 and plotted against the scratch distance.

### **3.3.3 Wear Testing**

Selected composite coatings (those with 14 wt% and 20 wt% of AO-2 and AO-4 grades graphene fillers) were selected for dry (unlubricated) sliding ball-on-disk tests. The testing was performed at both ambient conditions (25 °C) and elevated temperatures (200

°C) using 10-mm diameter steel balls. An applied load of 5 N at a sliding speed of 0.1 m/s was utilised during the testing, and each test ran for approximately 8 hours. The test coupons and the counterface balls were weighed before and after each test. Analysis was performed on the wear tracks through laser microscopy, which provided the wear rates of the tests through Equation 3.

The frictional force, which was measured during the testing, was utilised to determine the coefficient of friction. The variation of the coefficient of friction against the sliding distance was plotted for each test condition, and the average coefficient of friction for each sample was calculated during the period when the figures displayed a steady state condition.

### **3.4 Microscopy**

Optical microscopy was performed on the hot-compressed composite disks to determine the size and distribution of filler materials within the polymer matrix. Analysis of the particle distribution was performed using the ImageJ program [43]. Scanning electron microscopy (SEM) was also performed on these samples. Microstructure analysis was performed on the coated coupons to determine the area fraction of the filler materials within the polymer coating. The primer section of these microstructures can be ignored in this analysis, as it only serves to provide better adhesion between the substrate and the composite coating. Very little to no filler should be present within this thin layer.

Three samples per filler type were selected for microstructure analysis (1%, 10% and 20% for each). For the coated coupons, the cross-section of the coating, i.e. the substrate/coating interface, was exposed and cold mounted using an epoxy mounting resin. Significant grinding was performed at 180 grit to ensure the removal of any damage that

was present after cutting. Grinding of the samples was then performed using the following scheme: with 90° rotations between each subsequent step: 180, 320, 400, 600, 800, 1200, 2400, 4000 grits. The samples were then polished with 1 micron diamond suspension to remove the scratches.

The coating surface was also analyzed using laser profilometry for determination of the surface roughness of the coatings. Three images for each sample were obtained, and the surface roughness measurements were performed on each sample that underwent wear testing using the Keyence laser microscope. The average mean deviation of the assessed area ( $r_a$ ) and the root mean squared ( $r_q$ ) values were determined. Further analysis was performed on wear tracks and scratch marks generated through the mechanical and tribological testing on the coating surfaces. SEM was performed on the scratches generated through microscratch testing to observe the mechanism of failure and compare it to friction results from scratch testing.

## Chapter 4. Results

### 4.1 Compression-moulded Composite Disks

#### 4.1.1 Microstructure of the Compression-Moulded Disks

Optical microscopy has been used to characterize the cross-section microstructures of the hot-pressed disks. The ImageJ program was used to quantitatively analyze the distributions of the filler particles inside the polymer matrix. The optical images were placed through a binary filter (polymer sections become white, filler sections become black), which allows for the determination of the area fractions of the filler within the polymer matrix. An example of this is shown in Figure 16. Both grades of graphene filler as well as the MWCNT filler were characterized at the weight fractions described in Chapter 3. The optical images are shown in Figures 17 to 19,

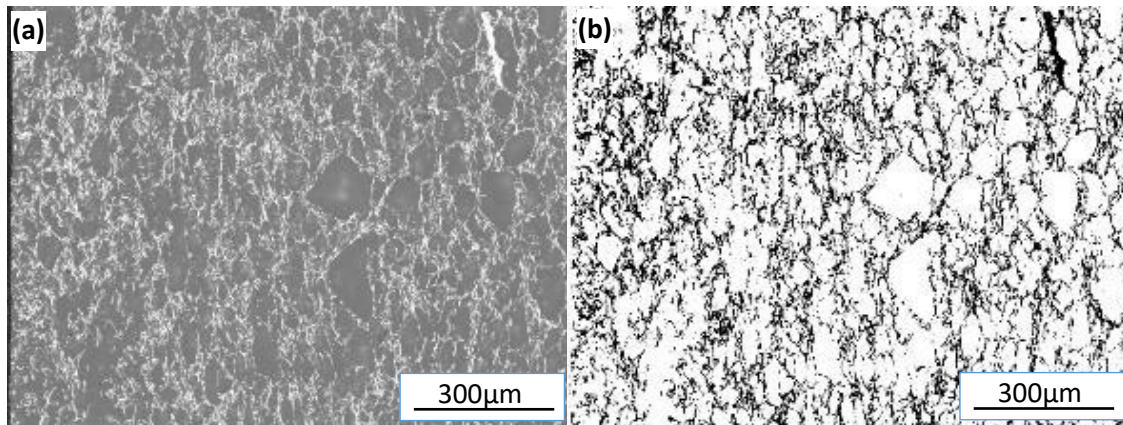


*Figure 16. AO-2 Graphene/AC-5600 PFA Composite 5% by weight 100x Magnification (a), binary filter (b).*

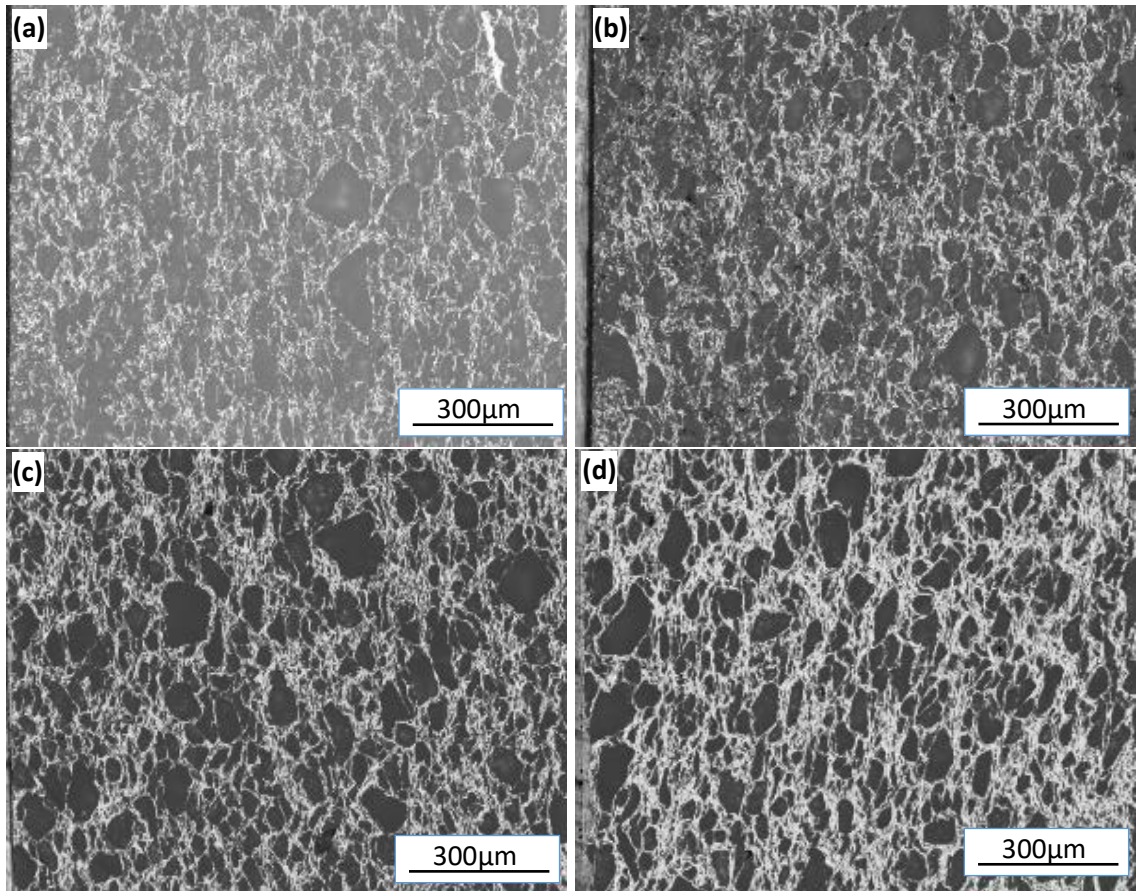


*Figure 17. AO-2 Graphene/AC-5600 PFA Composite 100x Magnification (a) 5wt%, (b) 10wt%, (c) 14wt%, and (d) 20wt%.*

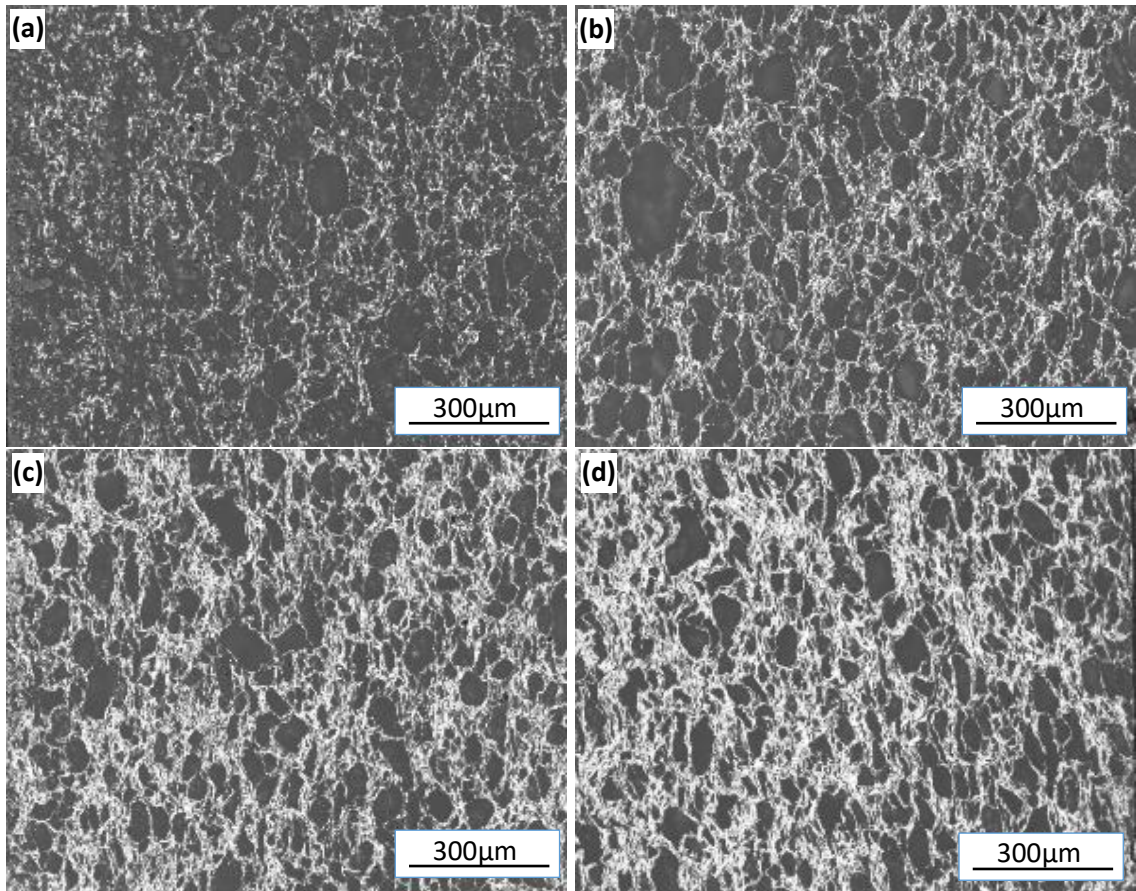


*Figure 18. AO-4 Graphene/AC-5600 PFA Composite 100x Magnification (a) 5wt%, (b) 10wt%, (c) 14wt%, and (d) 20wt%.*

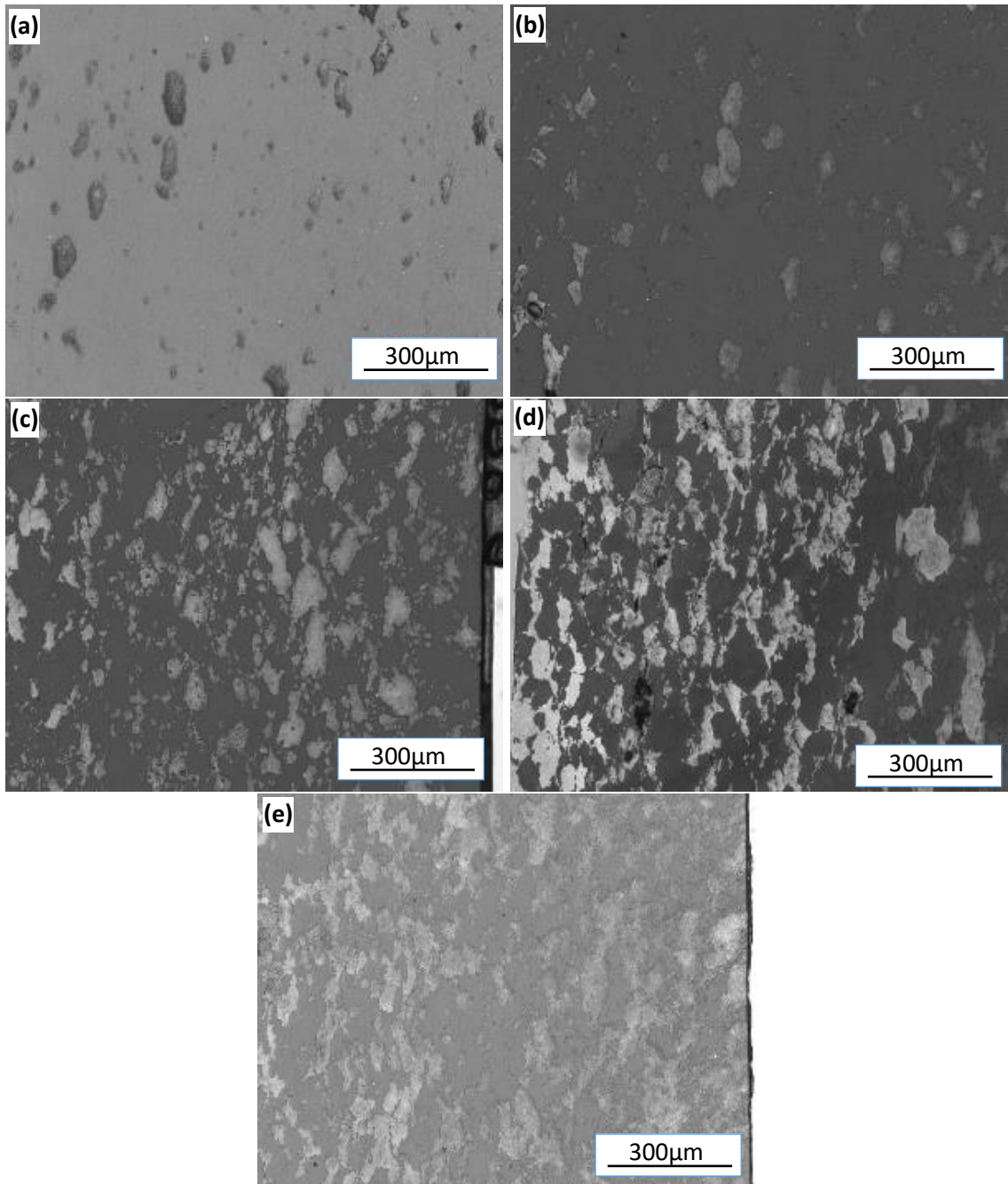


*Figure 19. MWCNT/AC-5600 PFA Composite 100x Magnification (a) 1wt%, (b) 5wt%, (c) 10wt%, (d) 14wt%, and (e) 20wt%.*

Attempts were made to adjust the contrast on the samples with 1 wt% AO-2 and AO-4 and graphene, but the ImageJ software could not identify the filler particles within the cross-sections because of the very low fraction of fillers. Only the sample with 1 wt%



MWCNT showed distinguishable fillers under this program. The results obtained from the area analysis are summarized in Table 3. The relationship between the weight fraction and the area fraction of the filler material is displayed in Figure 20.

*Table 3. Weight Fraction and Area Fraction of Filler Materials in Polymer Matrix.*

Filler Type	Weight Percentage (%)	Area Percentage (%)
<b>AO-2 Graphene</b>	5	21.04
	10	24.176
	14	28.256
	20	38.307
<b>AO-4 Graphene</b>	5	12.084
	10	19.708
	14	30.545
	20	37.92
<b>MWCNT</b>	5	6.329
	10	24.253
	14	30.204
	20	32.774

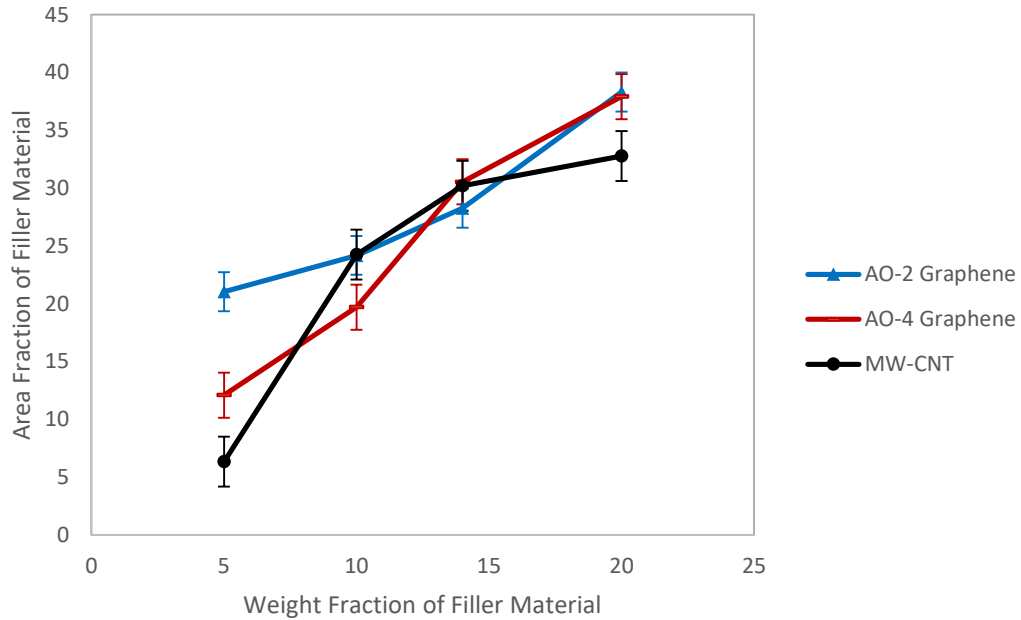


*Figure 20. Area fraction of the filler material with respect to the weight fraction of the filler material within the compression-molded composite materials.*

From these images, it is seen that the graphene samples tend to form quite uniformly distributed filler particles with the polymer matrix (Figures 17 and 18), while the MWCNT particles tend to agglomerate, forming large clusters (Figure 19). As expected, with the increase of the filler percentage, the observed filler area fraction increases. It is also evident that at higher weight fractions (14% and 20%), very little fluctuation in the area fractions is present among the filler types. In fact, the difference between the values of the samples (20 wt% AO-2 and AO-4 graphene) is less than 1%. This is not true at lower weight percentages, i.e. with the greatest difference being almost 10%. The results obtained from the MWCNT samples are also interesting to note. There is only a slight difference between the area fractions determined for the 1 wt% and 5 wt% samples. From Figures 19 (a) and (b), it can be seen that the size and number of particulates are quite similar, with only an increase in extremely small MWCNT particles in the 5 wt% sample. These extremely small particles contribute very little to the area fraction of the filler material, due to their limited size (the software could not recognize). Thus, these MWCNT samples show much lower area fractions than the graphene samples at the same filler weight percentages. With a larger fraction of MWCNT particles, these agglomerates become quite large and detectable, thus a similar area fraction to the graphene samples is reached at 20 wt%. However, the area fraction (33%) is still about 13% less than those of the graphene samples at 20 wt%.

#### **4.1.2 SEM of Composite Disks**

SEM was performed at CanmetMATERIALS on the cross-sections of the hot-pressed disks. Due to the similarities between the polymer and the filler materials (both

being carbon-based), no contrast between the filler and the polymer was observed in the backscattered electron images. A small notch was made on each sample using a saw, which allowed for easy fracture of the samples by hands. The samples were fractured to observe the fracture surface as well as the filler behaviour within the polymer matrix during fracture. Figures 21 to 29 display the SEM images of the fracture surfaces.

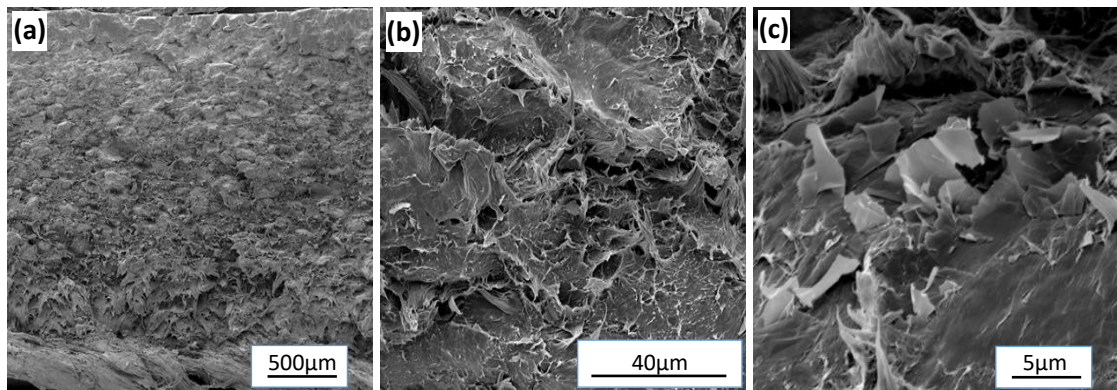


Figure 21. SEM images of AO-2 Graphene 1wt%: (a) 80 $\times$ , (b) 2,000 $\times$ , (c) 10,000 $\times$ .

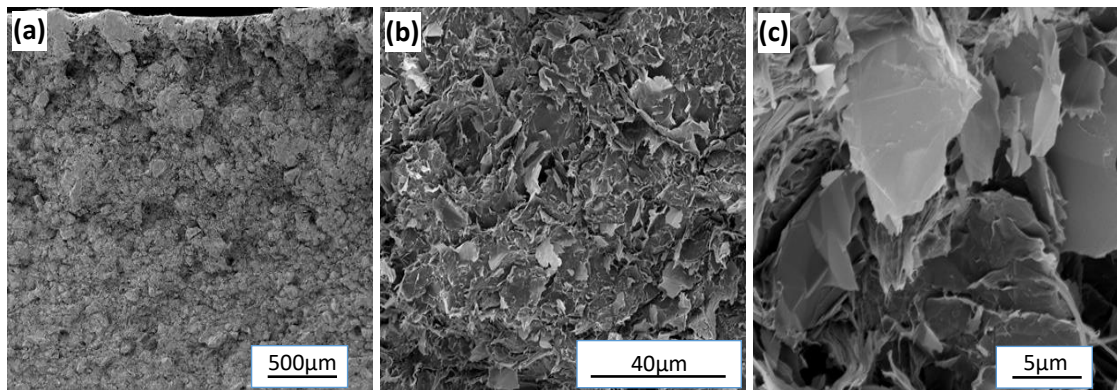


Figure 22. SEM images of AO-2 Graphene 10wt%: (a) 80 $\times$ , (b) 2,000 $\times$ , (c) 10,000 $\times$ .

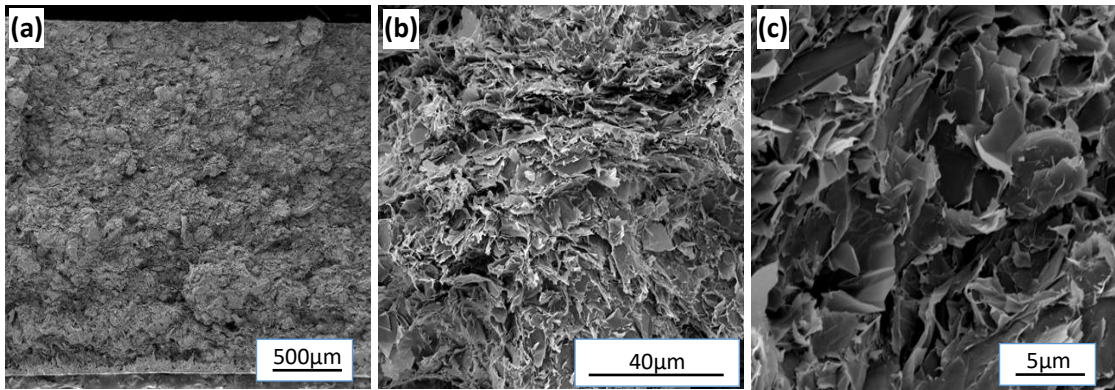


Figure 23. SEM images of AO-2 Graphene 20wt%: (a) 80×, (b) 2,000×, (c) 10,000×.

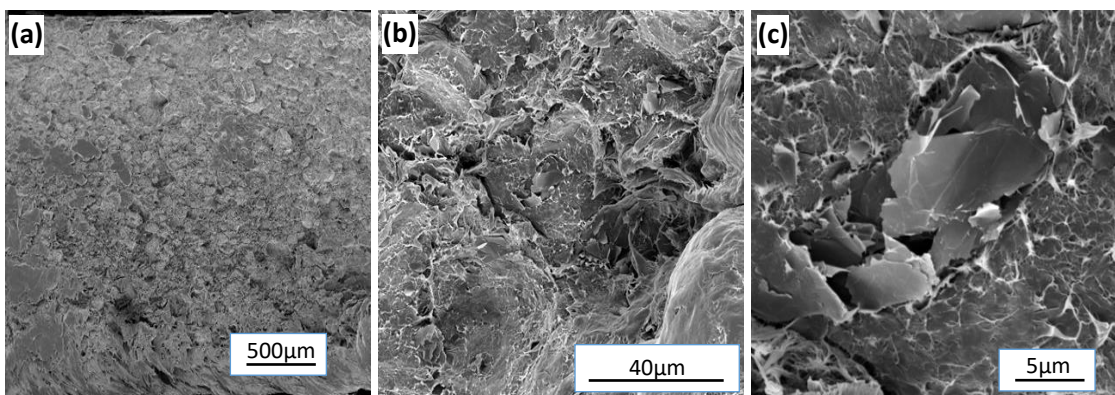


Figure 24. SEM images of AO-4 Graphene 1wt%: (a) 80×, (b) 2,000×, (c) 10,000×.

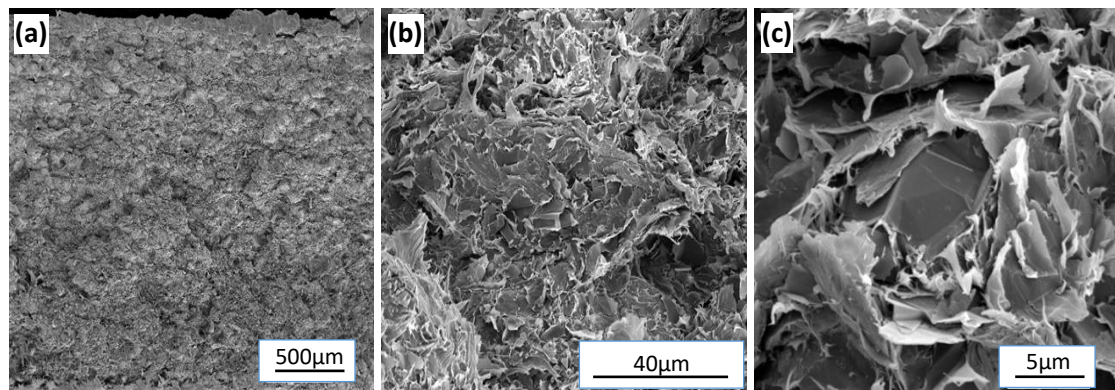


Figure 25. SEM images of AO-4 Graphene 10wt%: (a) 80×, (b) 2,000×, (c) 10,000×.

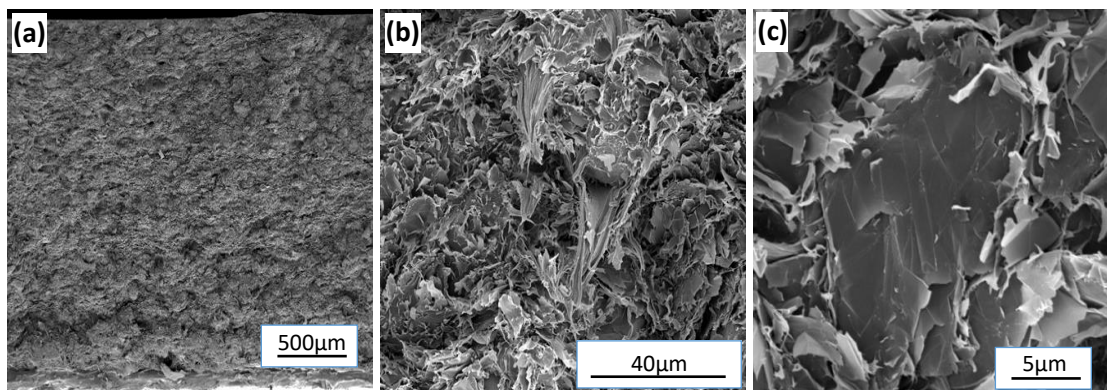


Figure 26. SEM images of AO-4 Graphene 20wt%: (a) 80 $\times$ , (b) 2,000 $\times$ , (c) 10,000 $\times$ .

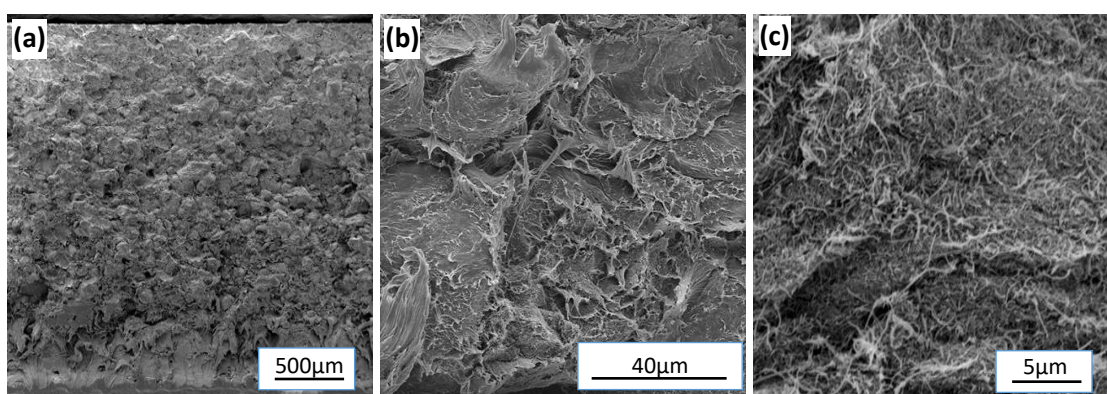


Figure 27. SEM images of MWCNT 1wt%: (a) 80 $\times$ , (b) 2,000 $\times$ , (c) 10,000 $\times$ .

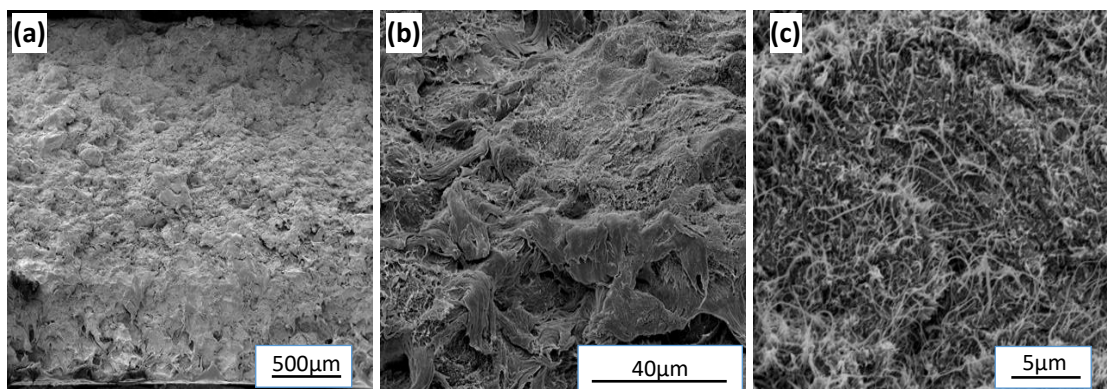


Figure 28. SEM images of MWCNT 10wt%: (a) 80 $\times$ , (b) 2,000 $\times$ , (c) 10,000 $\times$ .

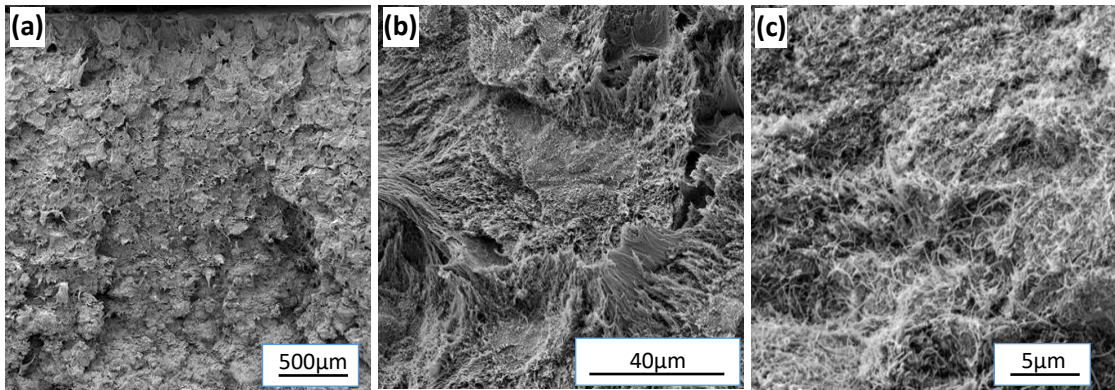


Figure 29. SEM images of MWCNT 20wt%: (a) 80 $\times$ , (b) 2,000 $\times$ , (c) 10,000 $\times$ .

Observations of the fracture surfaces of the composite disks yielded interesting results. In the graphene-filled samples, the graphene flakes were observable in 2,000 $\times$  magnification images in all but the 1 wt% filler samples. From the observation of these filler materials, it can also be determined that the AO-4 graphene flakes are significantly larger than those of the AO-2 graphene samples. In the MWCNT samples, the filler is only observable at 10,000 $\times$  magnification, due to the extremely small diameter of the nanotubes. The amount of filler material observable is proportional to the weight fraction of the filler within the composite, which is to be expected, with the exception of the images of the MWCNT samples, which all displayed similar amounts of filler material. This is most likely due to the way the particles were dispersed within the matrix of the composite. Graphene filler was spread evenly throughout the matrix, forming a network that spanned the entirety of the composite. The MWCNT filler formed agglomerates, thus the sections either contain a significant number of nanotubes, or none at all.

This may also explain why the fracture morphology is different among the samples. At low weight fractions, a large amount of the fracture surface would be composed of only polymer. The same can be said to the MWCNT samples, which do not have evenly

dispersed particles, and instead have agglomerates. Thus, a significant section of the fracture surface would consist of pure polymer. Polymers tend to deform under stress, rather than fracturing, thus a greater amount of plastic deformation in low filler content samples and MWCNT-filled samples is expected. Conversely, the well dispersed network of graphene filler at high weight fractions may have yielded a resistance to deformation, resulting in a more brittle fracture.

## 4.2 Thermal Measurements

### 4.2.1 Specific Heat Measurements

The specific heats of the composite disks were measured by differential scanning calorimetry (DSC). The results are shown in Figures 30-33. Although it is general true that with the increase of the filler amount, the specific heat increases, it is difficult to correlate the specific heat to the weight fraction.

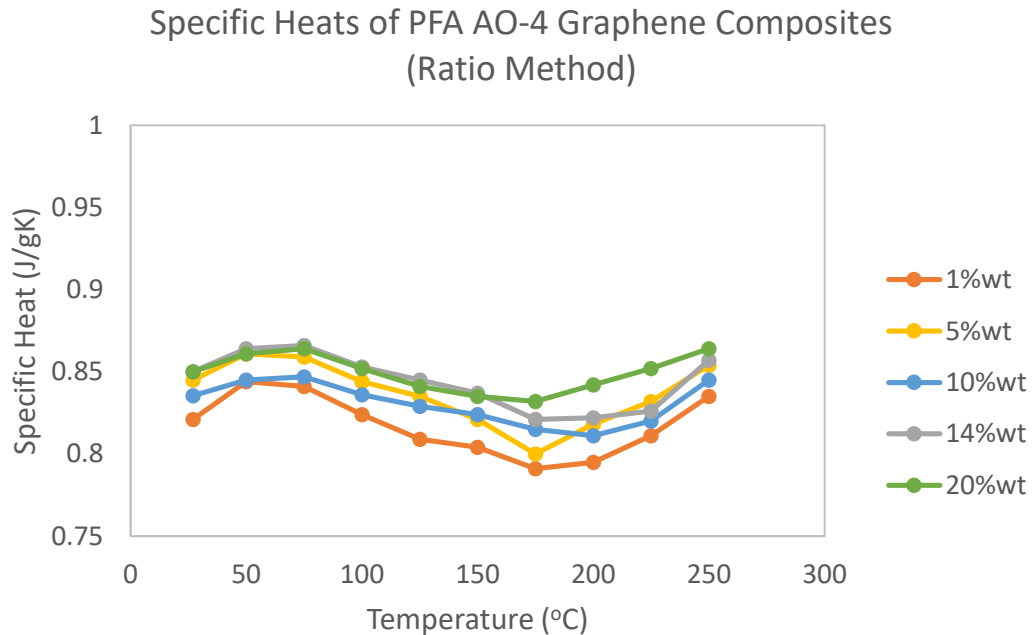


Figure 30. Heat Capacity of PFA AO-2 Graphene Composites (Ratio Method)

Specific Heats of PFA AO-4 Graphene Composites (ASTM E1269)

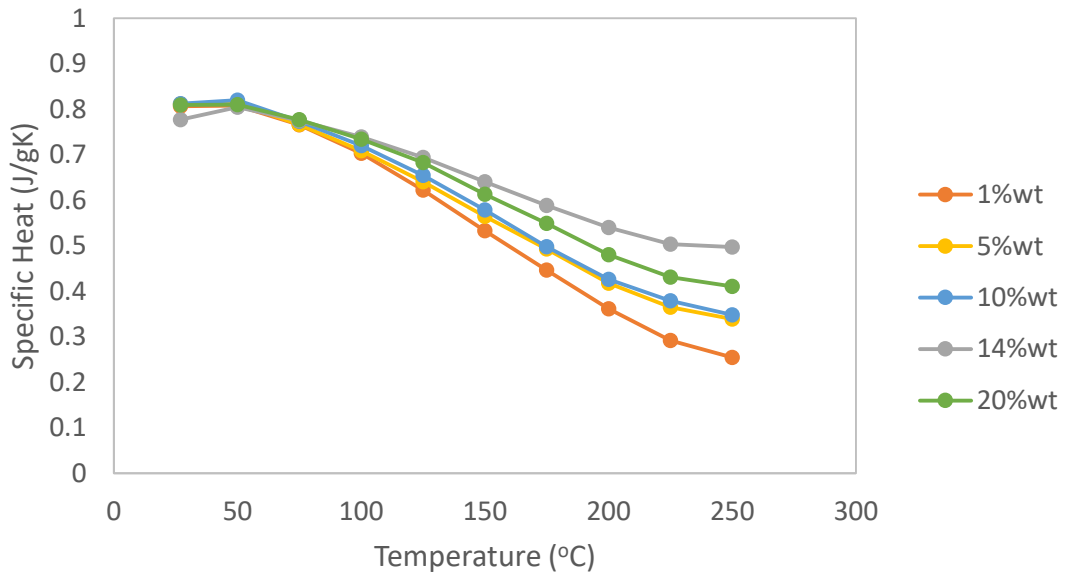


Figure 31. Heat Capacity of PFA AO-2 Graphene Composites (ASTM E1269)

It is evident from the data shown in Figures 31 and 32 that while the specific heats obtained from the ratio method are generally similar over large temperature ranges (they are not constant, but with fluctuations), those values obtained from the ASTM E1269 method show significant decreases at higher temperatures. The ASTM E1269 method adjusts for fluctuations by holding the sample at 300°C and observing the isothermal zones. However, the polymer does not hold flat  $c_p$  values at this temperature as the material is approaching melting. Due to this, the ratio method will be utilized in all further calculations.



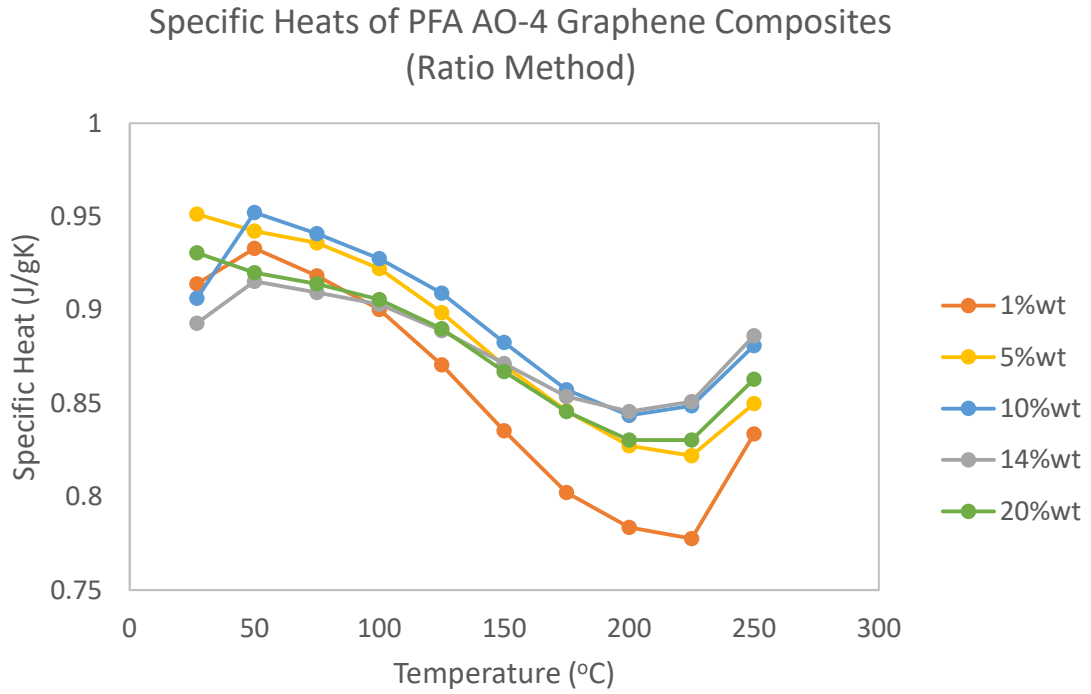


Figure 32. Heat Capacity of PFA AO-4 Graphene Composites (Ratio Method).

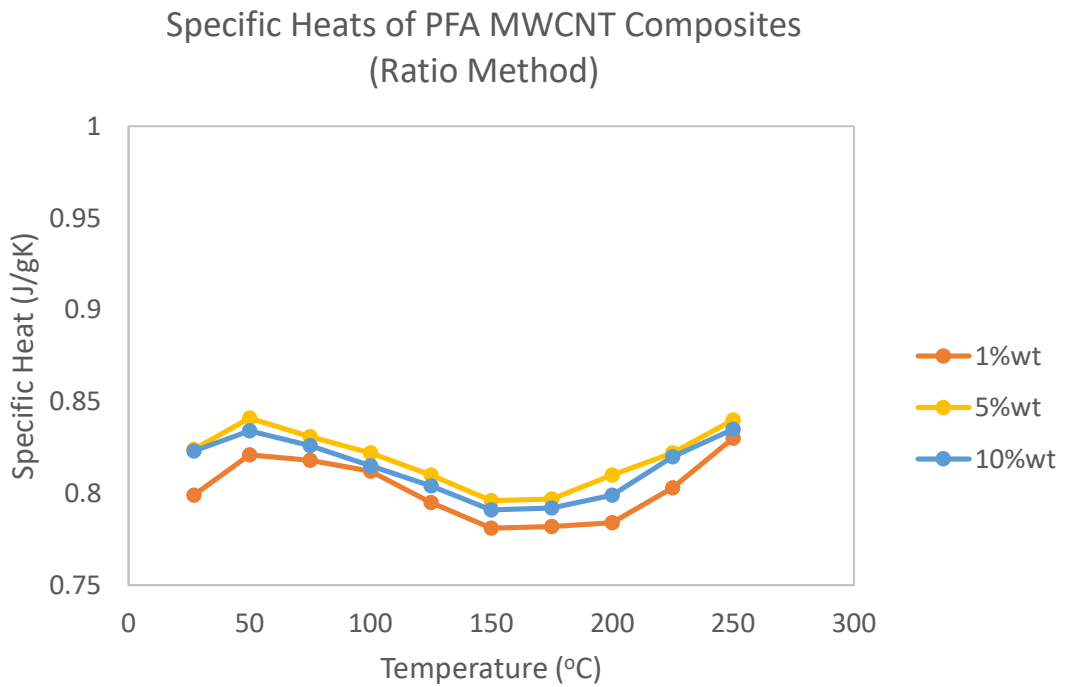


Figure 33. Heat Capacity of PFA MWCNT Composites (Ratio Method).

It should be noted that, the specific heat values of the MWCNT-filled composites are only available for three weight fractions (Figure 32). The 14% wt and 20% wt samples did not show results that would be reasonably expected with respect to the lower weight fraction samples. Given the minor variations in specific heats between the weight fractions, the specific heat for the 10 wt% sample was used to all the samples with more than 10 wt% MWCNT filler. It can be observed that a general trend is followed for all specific heat values using the ratio method, beginning with a slight increase, followed by a gradual decrease at approximately 50-75 °C, and finally an increase at 175-200 °C. The specific heats of the AO-2 filled samples in Figure 31 were observed to be lower than those filled with AO-4 graphene at low temperatures (50 - 100 °C) in Figure 33, but reached similar values at high temperatures. The values obtained for the MWCNT filled samples in Figure 33 were comparable to those of the AO-2 filled samples.

#### **4.2.2 Laser Flash Results**

Laser flash analysis was performed on the samples to determine their thermal diffusivity. The results are displayed in Figures 34-36.

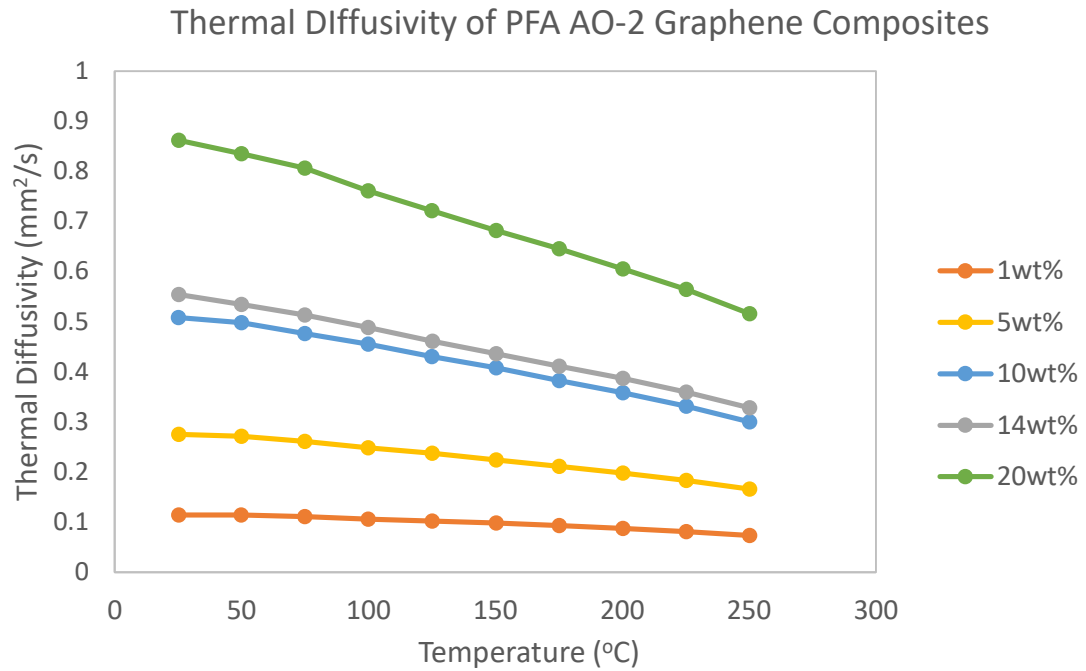


Figure 34. Thermal Diffusivity of PFA AO-2 Graphene Composites  $\sigma = 0.022\text{mm}^2/\text{s}$ .  $\sigma$  denotes standard deviation of thermal diffusivity.

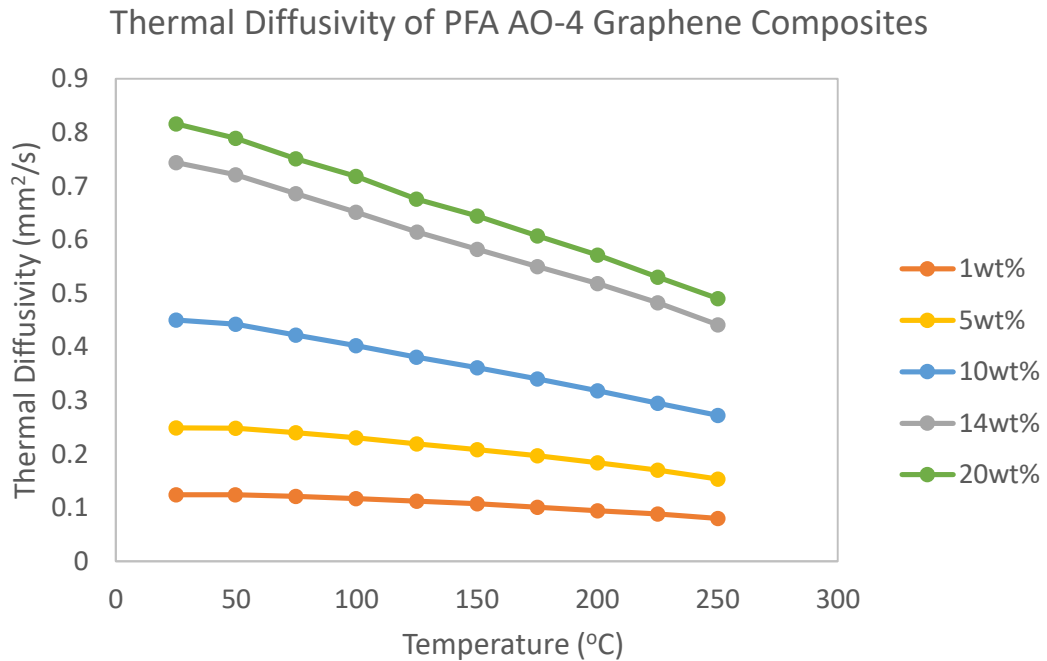


Figure 35. Thermal Diffusivity of PFA AO-4 Graphene Composites  $\sigma = 0.018\text{mm}^2/\text{s}$ .

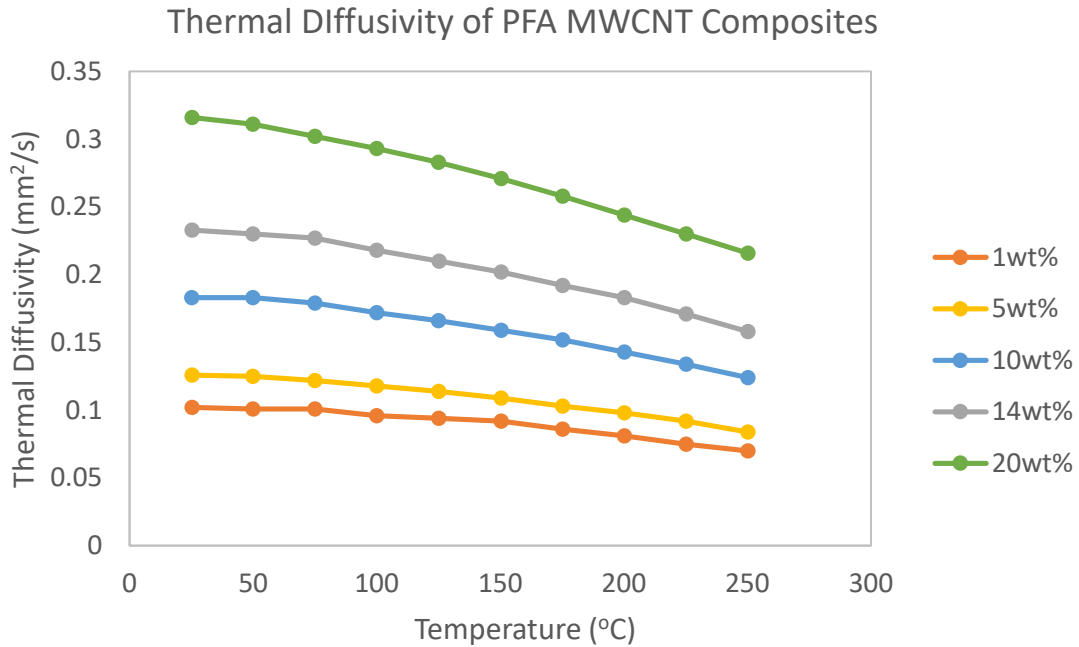


Figure 36. Thermal Diffusivity of PFA MWCNT Composites  $\sigma = 0.015\text{mm}^2/\text{s}$ .

Both graphene-filled composites (Figures 34-35) showed similar thermal diffusivity values as compared to the MWCNT values (Figure 36). Similar values among all three filler materials was only observed at the lowest weight fraction of filler material. With all filler materials, an increase in the thermal diffusivity was observed with an increase in filler content. At higher filler content, all samples showed a general decrease in diffusivity with an increase in temperature.

### 4.2.3 Thermal Conductivity Results

Thermal conductivity values were determined using Equation 1 along with the measured specific heat, thermal diffusivity, and density values. The calculated values are

displayed in Figures 37-39. Both graphene-filled composites yielded rather high thermal conductivities at high filler content, which was not seen in the MWCNT-filled composites. A general downward trend in the thermal conductivities of all samples was observed with an increase in temperature. It is also observed that an increase in filler content did yield an increase in thermal conductivity, which is to be expected.

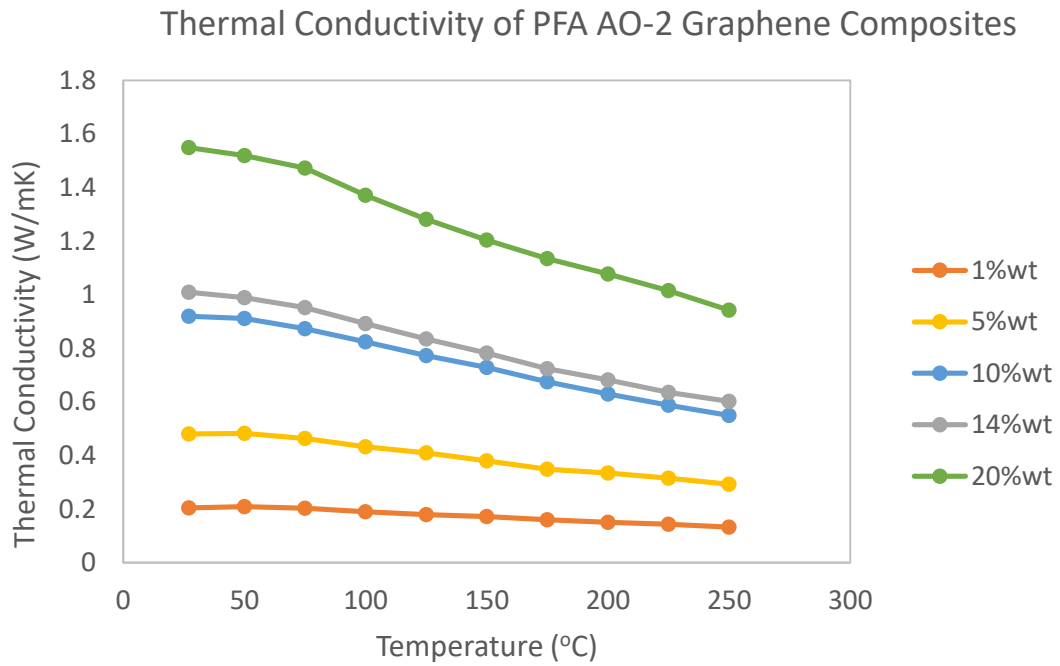


Figure 37. Thermal Conductivity of PFA AO-2 Graphene Composites  $\sigma = 0.044\text{mm}^2/\text{s}$ .

Thermal Conductivity of PFA AO-4 Graphene Composites

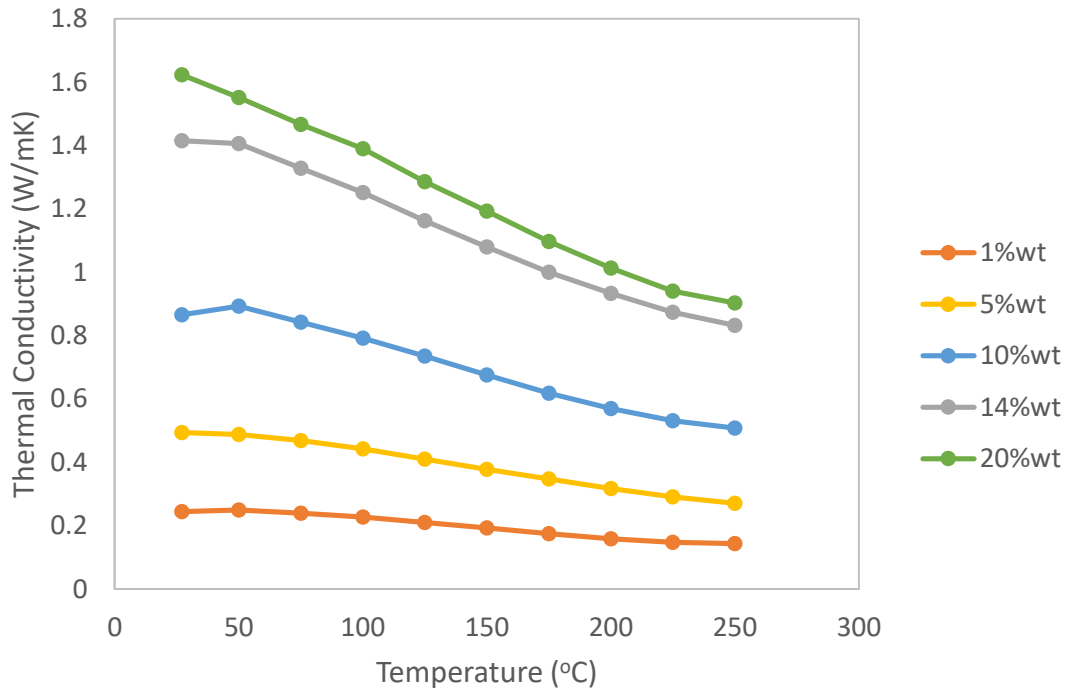


Figure 38. Thermal Conductivity of PFA AO-4 Graphene Composites  $\sigma = 0.036\text{mm}^2/\text{s}$ .

Thermal Conductivity of PFA MWCNT Composites

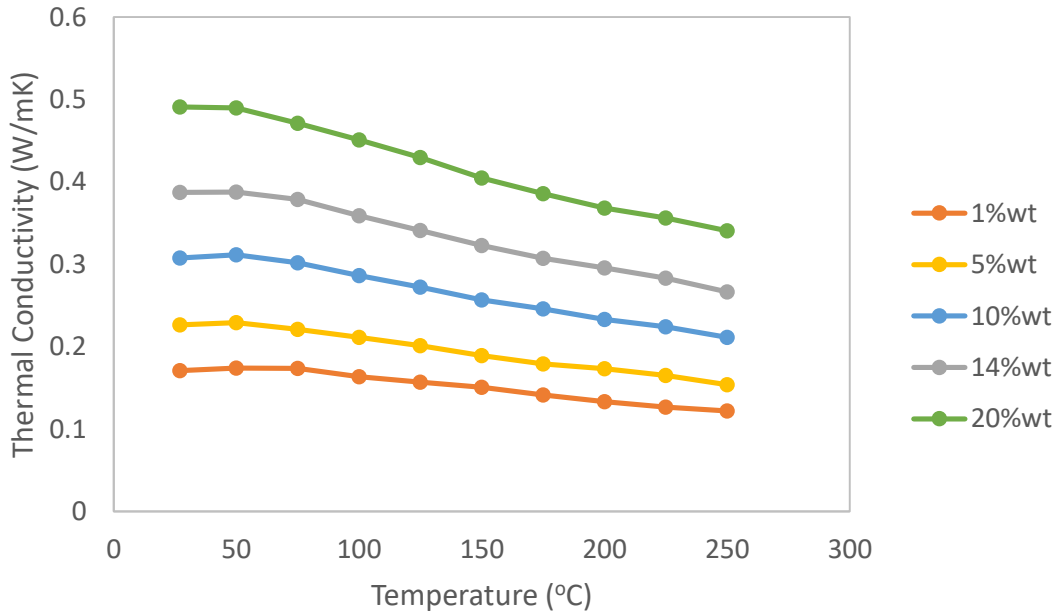


Figure 39. Thermal Conductivity of PFA MWCNT Composites  $\sigma = 0.025\text{mm}^2/\text{s}$ .

As expected, with an increase in the weight fraction of the high-thermal-conductivity filler material within the polymer matrix, an increase in the thermal conductivity is observed. With the exception of the 14 wt% graphene-filled samples, which indicated a large fluctuation between samples, it appears as if the thermal conductivity of the filled composites exhibits a near direct proportionality to the weight fraction of filler. At room temperature, the 10 wt% AO-2 graphene samples have a thermal conductivity of approximately 0.9 W/mK, while at 20 wt% AO-2 graphene, a thermal conductivity of 1.6 W/mK is observed. This is an 80% increase in thermal conductivity with a 100% increase in the weight fraction of the filler. The same phenomenon can be observed in all samples for both grades of graphene, except for the 1 wt% samples, which only show slightly higher thermal conductivities than the polymer matrix. This proportionality is not as direct in the MWCNT-filled samples, i.e. with the increase in thermal conductivity being significantly lower as compared to the graphene-filled samples.

It can be observed that with an increase in the temperature, the thermal conductivities of the composites decrease. This is the case for all samples except for those at low weight fractions. This results from the thermal diffusivity values, as the conductivity and diffusivity are directly proportional. In prior work, the thermal conductivities were constant over a range of temperatures, as the specific heats of the samples increased with increasing temperature [10]. In this research, the specific heat values fluctuated, but overall did not increase or decrease significantly, thus the decrease in the thermal conductivity due to the thermal diffusivity is not counteracted.

### 4.3 Electrical Resistivity Measurements

The surface electrical properties of several carbon-filled polymer composites were evaluated to determine the effect of an increase in filler content on these properties. No value for the surface resistance for any composites with a weight percentage of 1% could be determined (due to the limitation of the measuring device). In the case of the multi-walled carbon nanotubes, a weight percentage of 5% also did not yield electrical property results. These results have been compiled in Figure 40.

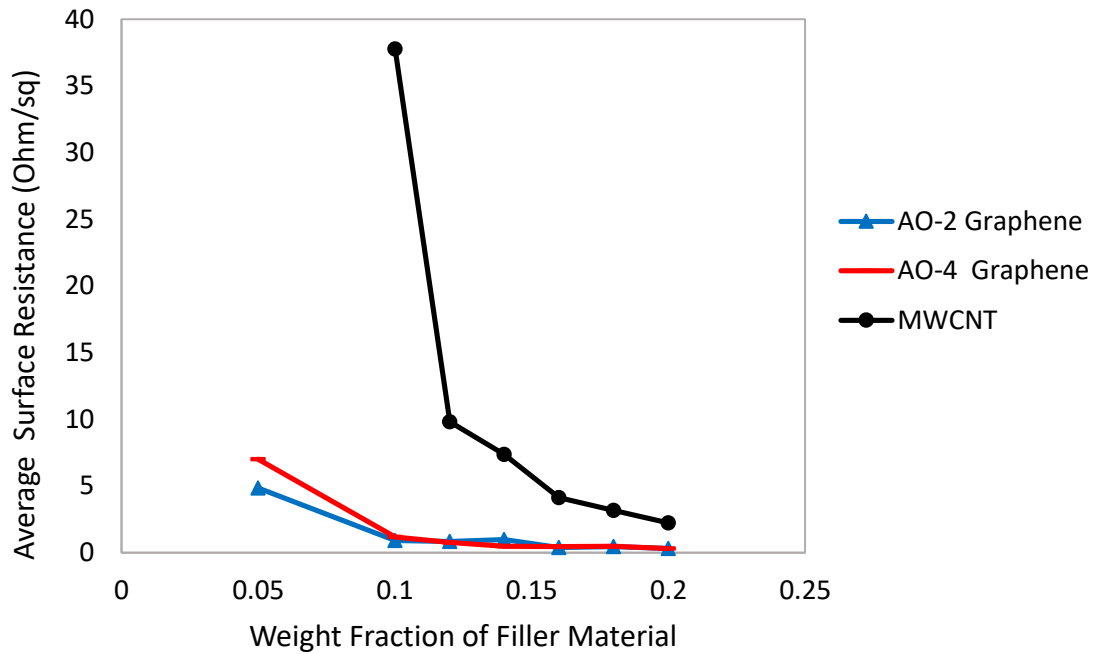


Figure 40. Electrical surface resistivity of filled PFA composites. Measurements were performed using a Pro-4 Four-Probe resistivity sensor at five locations on the surface of each compressed disk sample.

It was determined that both AO-2 and AO-4 graphene yield similar surface resistances, with the AO-2 filled samples yielding slightly lower resistances. The difference



at high filler contents (20% by weight) is almost negligible. This is not the case when comparing the MWCNT samples to either graphene sample. The resistance of the MWCNT samples at 10 wt% is almost 40 times greater than either of the graphene-filled composites at that weight fraction. At the greatest weight fraction tested (20%) the resistance was slightly higher for the MWCNT sample than the graphene samples. However, this difference is much smaller than that 10 wt%. These results are quite similar to those obtained from thermal property measurements. The pathways with which thermal energy is transferred in thermal diffusivity testing, and electrons in electrical conductivity tests are essentially the same within these samples. A connected network of filler particles is what allows for this transfer of energy; thus it is expected that with the increase in filler content, an increase in the electrical conductivity of the samples is observed. The difference of these results from the thermal results is that once a network has already been established within the material, increases in filler content may not generate even faster pathways, so there is a point, known as the percolation threshold where increases in the filler content will not yield a significant increase in the electrical transfer properties of the samples.

For the graphene samples, that threshold is most likely achieved between the 1 wt% and 5 wt% filled sample. Given that the 1 wt% sample did not yield any results due to extremely poor conductivity, while the 5 wt% samples yielded a value similar to those with filler content greater than 5 wt%, the percolation threshold must be between these two values. The decrease in the electrical resistance between 5 wt% and 10 wt% is significant, but most likely due to being at the tail end of the threshold. The percolation threshold for MWCNT-filled samples is most likely approximately 10 wt%, as a significant drop in the resistance is observed at weight fractions greater than this. It is also observed that both

grades of graphene yield very similar electrical resistance, with variability most likely due to differences within the matrix itself. It is possible that sections of low or high filler content may have yielded this fluctuation.

Composites containing graphene filler displayed a well-connected network of particles throughout the material, while those containing MWCNT displayed agglomerations within bulk polymer. Significant increase in thermal conductivity and decrease in surface electrical resistance was observed in samples containing graphene fillers, with limited effects in those containing MWCNT. There was essentially no difference in the microstructures or the properties of composites containing either grade of graphene.

## **4.4 Fluoropolymer Composite Coatings**

### **4.4.1 Optical Microscopy of Fluoropolymer Composite Coatings**

Cross-sections of the coatings were observed under optical and laser microscopy. The layout of the coating cross-section can be observed in Figure 41.

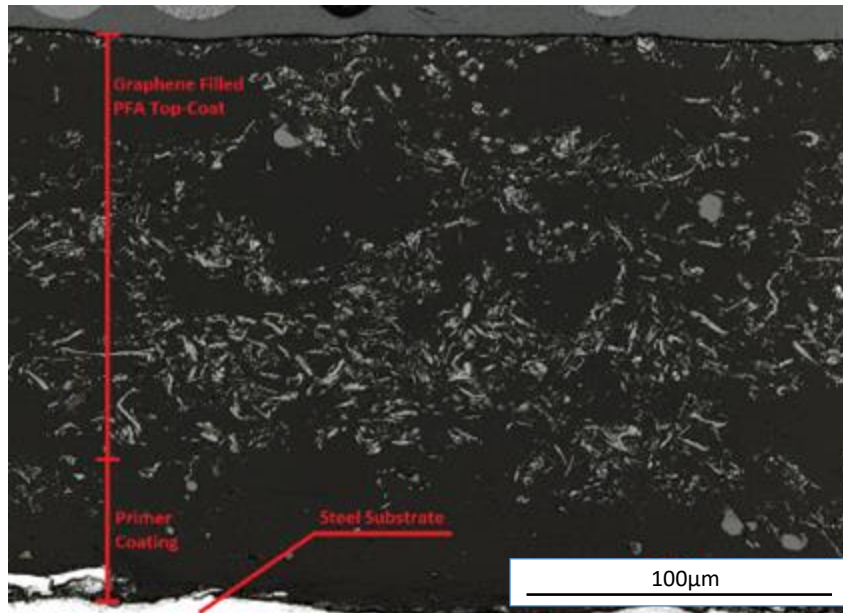


*Figure 41. The cross-sectional optical microscopy image of PFA matrix – 10 wt% AO-2 graphene filler coating on steel substrate.*

Figures 42-50 display the microstructures under optical imaging and binary views of these microstructures used to determine the area fraction of the particles within the microstructures using the ImageJ software.

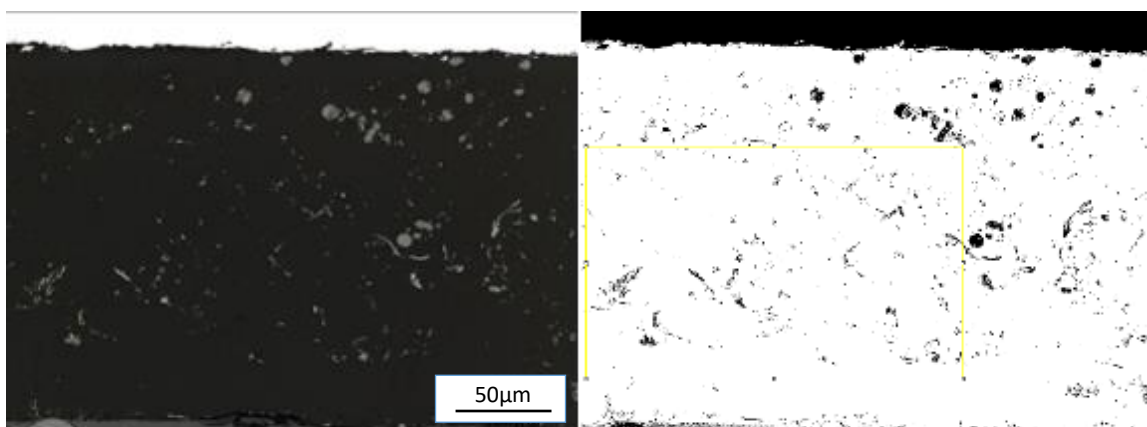


*Figure 42. AC-5600 PFA Composite with 1 wt % AO-2 Graphene Filler (left), binary view (right).*

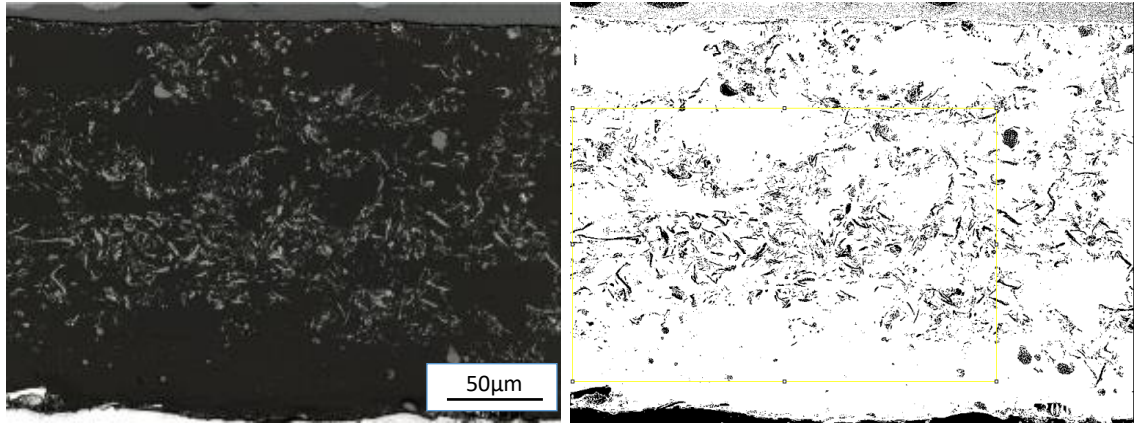


*Figure 43. AC-5600 PFA Composite with 10 wt % AO-2 Graphene Filler (left), binary view (right).*

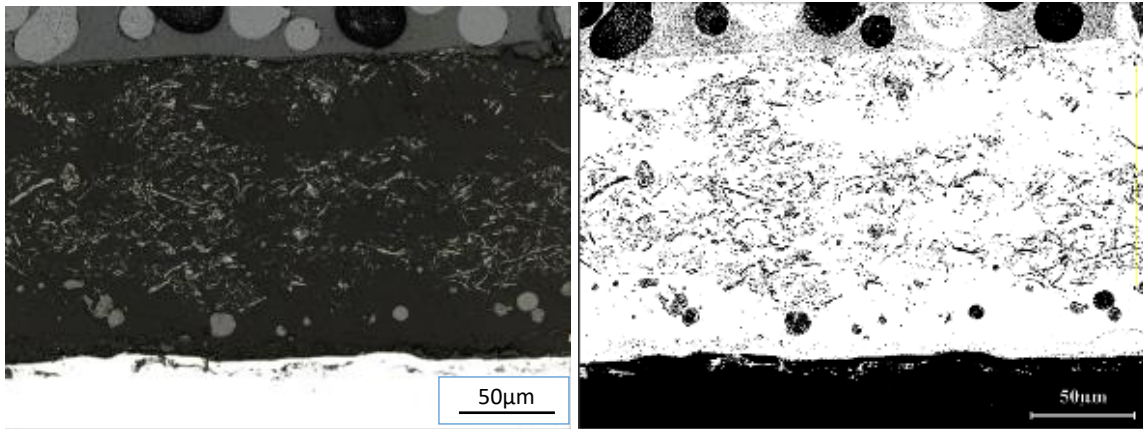


*Figure 44. AC-5600 PFA Composite with 20 wt % AO-2 Graphene Filler (left), binary view (right).*

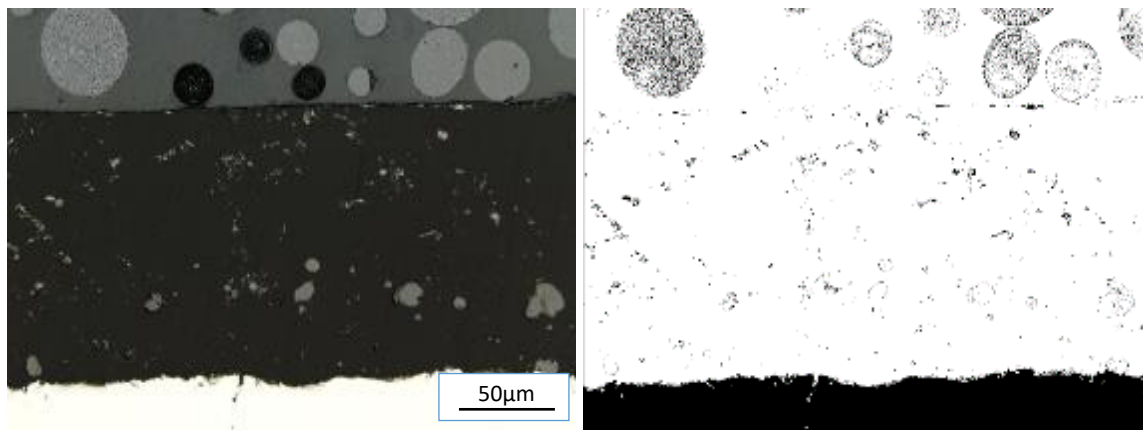


*Figure 45. AC-5600 PFA Composite with 1 wt % AO-4 Graphene Filler (left), binary view (right).*

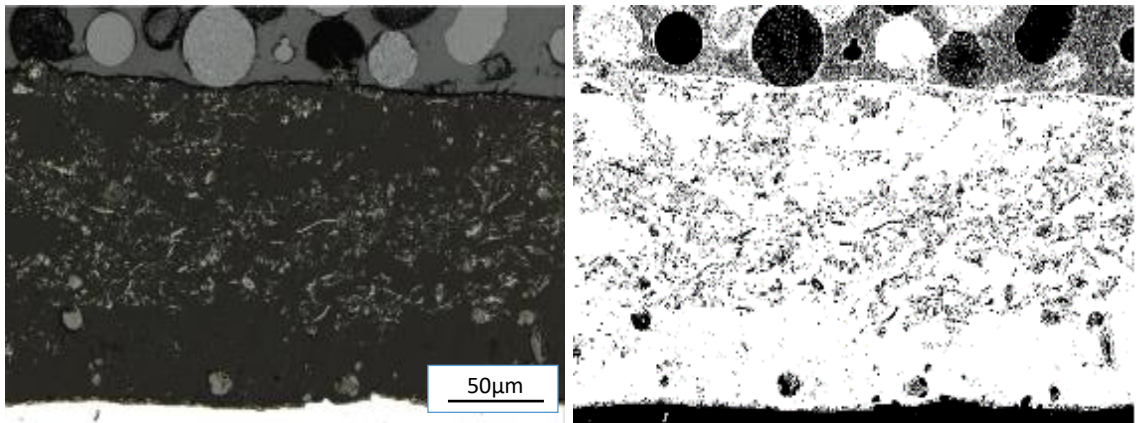


Figure 46. AC-5600 PFA Composite with 10 wt % AO-4 Graphene Filler (left), binary view (right).

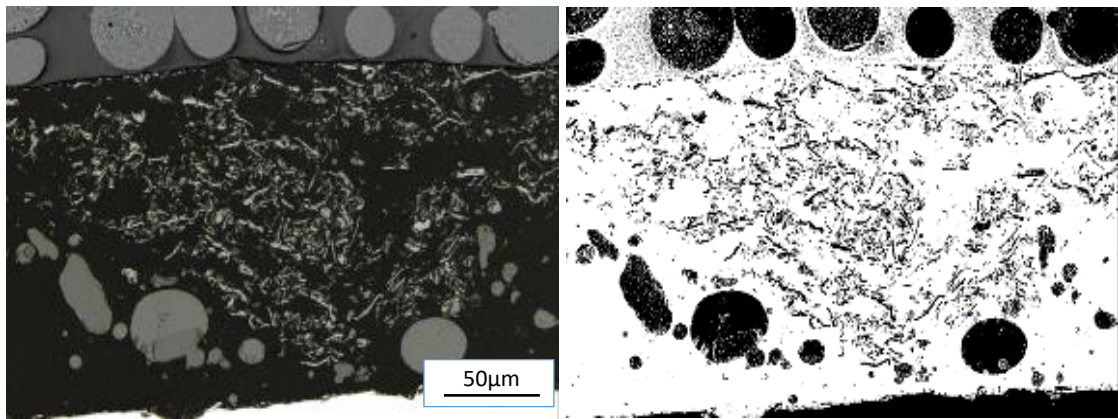


Figure 47. AC-5600 PFA Composite with 20 wt % AO-4 Graphene Filler (left), binary view (right).

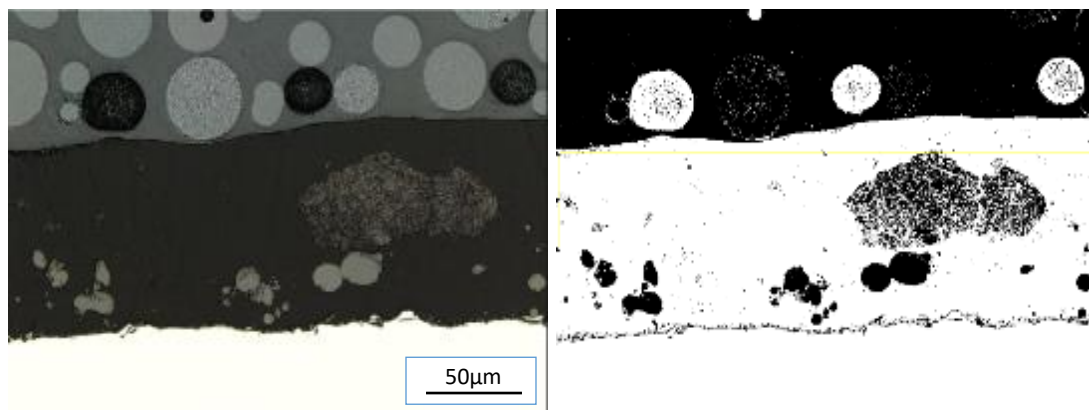


Figure 48. AC-5600 PFA Composite with 1 wt % MWCNT Filler (left), binary view (right).

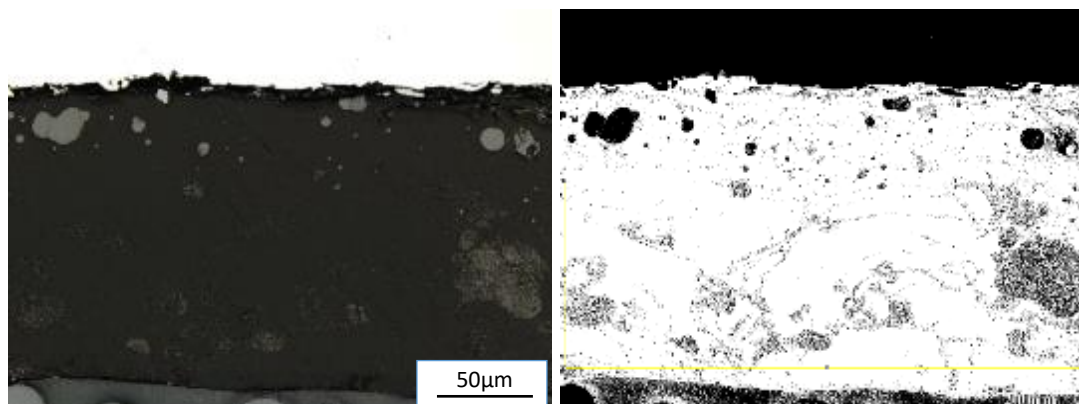


Figure 49. AC-5600 PFA Composite with 10 wt % MWCNT Filler (left), binary view (right).

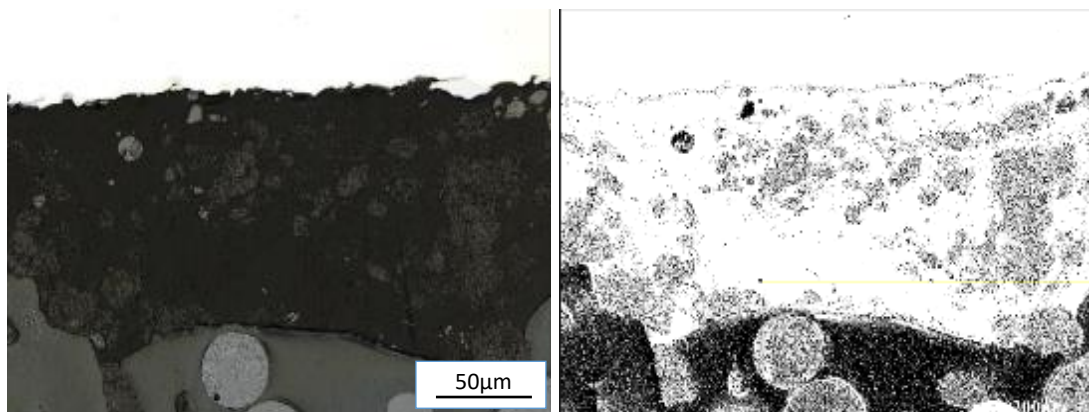


Figure 50. AC-5600 PFA Composite with 20 wt % MWCNT Filler (left), binary view (right).

Table 4. Area fraction of filler materials within composite coatings.

Weight Percentage	AO-2 Graphene	AO-4 Graphene	MWCNT
1%	2.576	0.831	6.317
10%	7.125	10.32	6.872
20%	9.119	12.513	13.142

From the results provided in Table 4, it is observable that area fractions of filler within the polymer matrix of the hot-pressed samples are consistently greater than that of the coatings. When observing the layout of the graphene-filled microstructures, a considerable difference is noticed. In the hot-pressed samples (Figures 17 and 18) a network of graphene flakes is formed, this is not apparent in the coated samples (Figures

42-47), and a more random orientation of particles is present. In both cases, significantly sized sections of the microstructure remain pure polymer with no presence of graphene within them; however, these sections are more defined in the hot-pressed samples. It can also be observed that the AO-4 graphene filled samples in Figures 45-47 contain larger particles than that of the AO-2 graphene filled samples in Figures 42-44. This corresponds to the observations made in the SEM of the fracture surfaces of the composite disks, as well as the properties of the filler materials themselves.

A similar microstructure is observed between the MWCNT hot-pressed and coated samples. Large clusters of filler are present in both microstructures. It is observable that large differences in the number of clusters are present; however, that is due to the scale of the microstructure. Only approximately 150-250 microns of material is observable due to the nature of the coating, while the hot-pressed samples were 2 mm in thickness. As such, the number of particles cannot be directly compared. This notion may also yield an explanation as to why there is such a difference in the area fraction between the hot-pressed and coated samples. A much smaller area of analysis is present in the coated samples due to the nature of the coating needing to be relatively thin, resulting in a much smaller area for analysis. It can be stated that some difference in the area fraction may be due to the nature of sample preparation (hot-pressing vs. electro-static spray coating) given that there is a difference in the microstructures of the samples. However, the scale of analysis may also have resulted in a significant difference in the area fraction of each sample.

Graphene filled coatings were shown to have good cohesion and a uniform coating thickness. Coatings containing MWCNT showed poor cohesion and significant variability

in coating thickness. Based on these results, only graphene coatings were selected for adhesion and durability testing.

#### 4.4.2 Scratch Testing of Composite Coatings

Scratch tests were performed on two selected composite coatings due to their high quality thermal and electrical properties. Figure 51 shows the variation in and coefficient of friction with respect to the scratch distance during scratch testing for both tested samples.

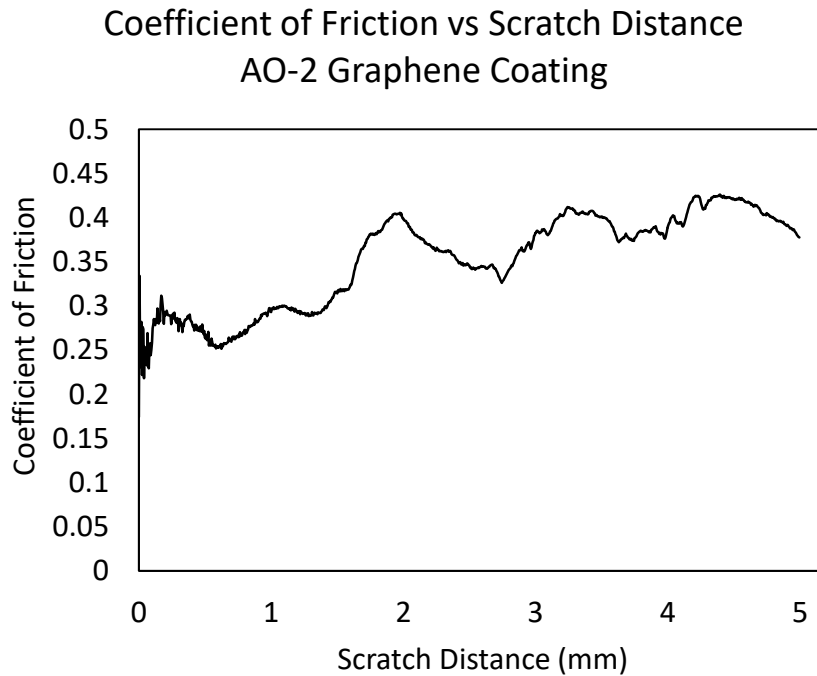


*Figure 51 Coefficient of friction vs scratch distance in AO-2 Graphene Coating during microscratch testing.*



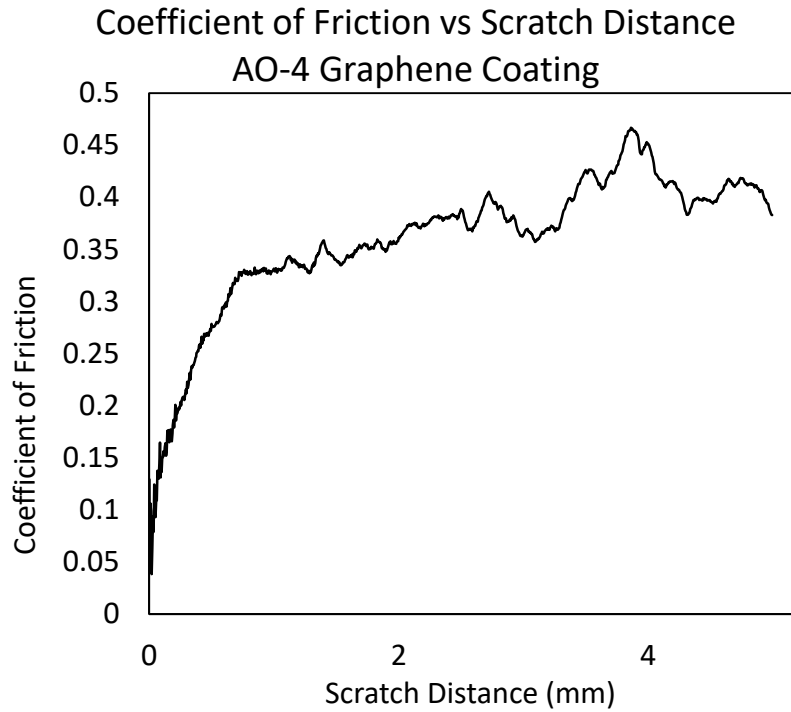


*Figure 52. Coefficient of friction vs scratch distance in AO-4 Graphene Coating during microscratch testing.*

SEM analysis was performed on both scratch tracks to compare the track with the friction data. Figure 52 displays the entire scratch track under SEM, as well as an area of interest within each of the tracks.

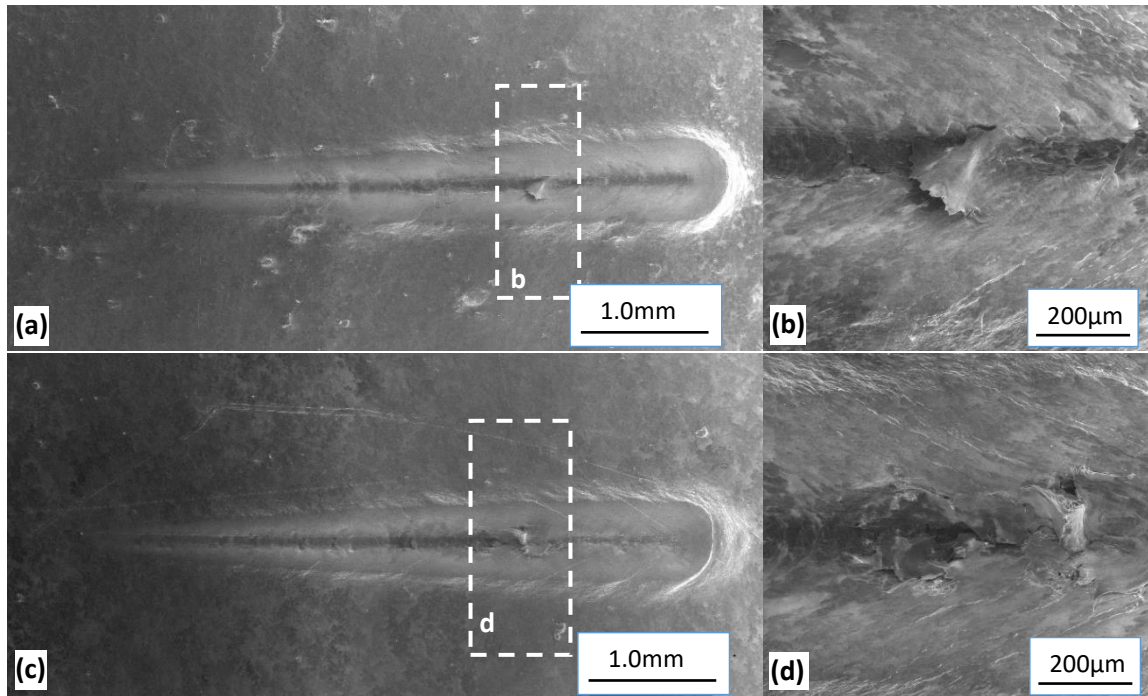


*Figure 53. Secondary electron SEM images of (a) the scratch track on the surface of AO-2 graphene composite coating, the enclosed area “b” indicates where closer inspection was performed; (b) higher magnification image of area “b” in Fig. 10(a), displaying a tear in the coating; (c) the scratch track on the surface of AO-4 graphene composite coating, the enclosed area “d” indicates where closer inspection was performed; (d) higher magnification image of area “d” in Fig. 10(c), displaying elongated fibers leading to a tear in the coating.*

Under SEM, it was observed that at approximately the 3.5 mm mark of the scratch track on both samples, unusual damage to the coating is present. It appears as if there is a section of material that was torn during the scratch test. This damage is displayed in Figure 52 (b) and (d). In the AO-2 sample, this section corresponds to a fluctuation in the frictional force near the maximum observed friction. This fluctuation phenomenon occurs for approximately another millimeter before an eventual decrease in frictional force. It is possible that this section of material was dragged by the scratch head for a significant distance and may provide an explanation for the odd fluctuation in Figure 51. In the AO-4

sample, this section also corresponds with an interesting section of Figure 52. A sharp increase in the frictional force was observed at approximately 3.5 mm which may be the result of a section of the coating being torn.

Other than the damaged areas that were mentioned previously, very little can be observed through these images. It is important to note that given both filler and matrix are carbon based, there will be almost no distinction between the two within these images. Several chevrons are noticeable at the edges of the track which indicate separation of the matrix during scratching.

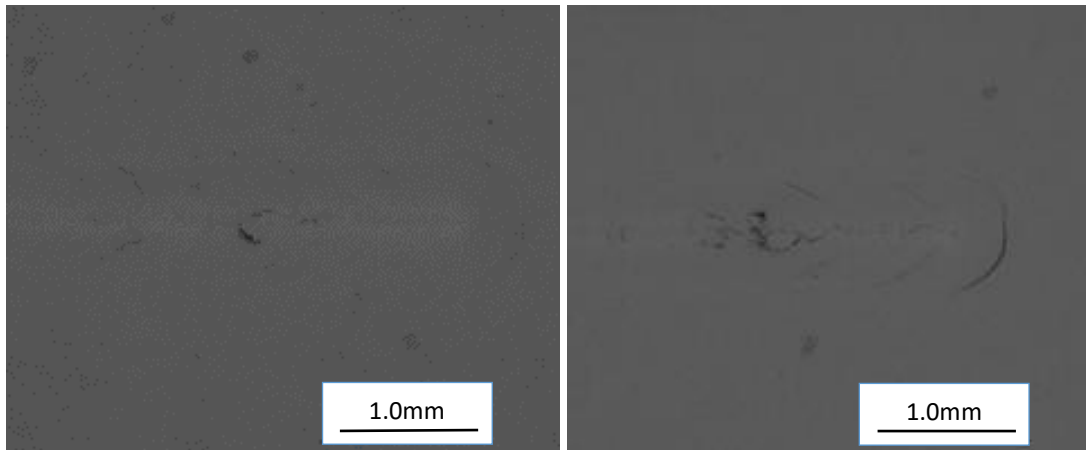


*Figure 54. SEM BSE images of scratch tracks at end of scratch of AO-2 graphene filled PFA coating (left), and AO-4 graphene filled PFA coating (right).*

BSE imaging showed very little variability in the images of the scratch tracks, even near the end of the track, where the indenter applied the highest load. From this it can be determined that there was no indenter-substrate contact. BSE images of both coatings near the end of the scratch can be seen in Figure 53.

Analysis was performed on the end of the scratch tracks (the locations that were under the greatest load during scratching). Figures 54 and 55 indicate a maximum depth of

penetration at 100 microns for the AO-2 grade graphene sample and 125 microns for the AO-4 grade graphene sample. The maximum scratch depth between the two samples is significant; however, there may be many causes that will be discussed in the discussion chapter.

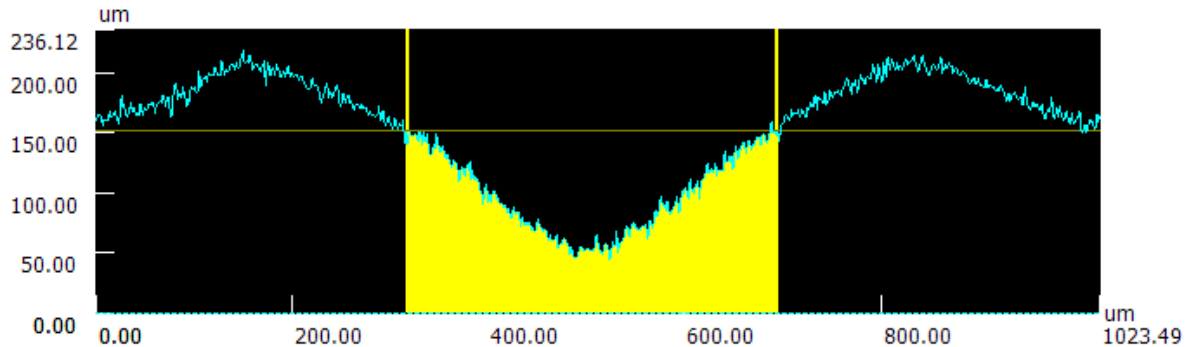


*Figure 55. Scratch depth analysis of AO-2 grade graphene filled PFA composite coating at maximum scratch load.*

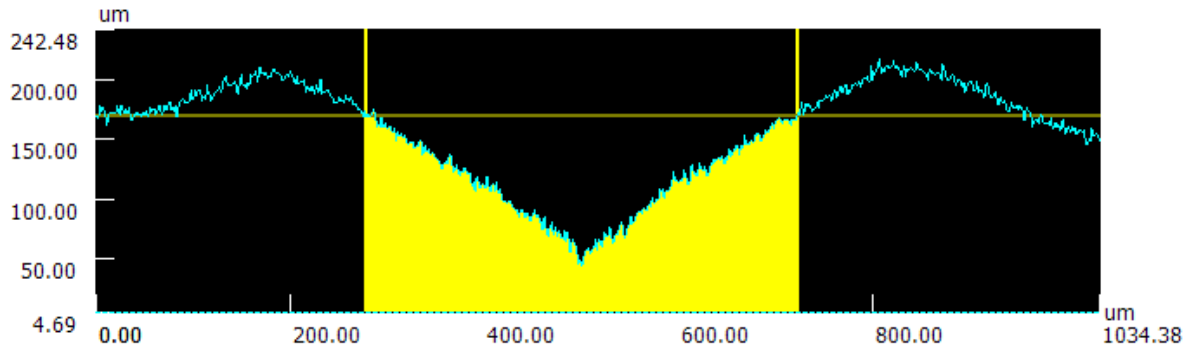


*Figure 56. Scratch depth analysis of AO-4 grade graphene filled PFA composite coating at maximum scratch load.*

### 4.4.3 Surface Roughness

Prior to wear testing, the surface roughness of the coatings was characterized. Images of the surfaces were taken. The samples with greater filler content yielded a greater surface roughness. This can be seen in Table 5, which describes the average surface

roughness  $r_a$  and the root mean squared values  $r_q$ . Samples are labeled in terms of the wear testing conditions to which they were subjected.

*Table 5. Surface roughness values of PFA composite coatings.*

Filler Material	Weight Percentage	Temperature	$r_a$ ( $\mu\text{m}$ )	$r_q$ ( $\mu\text{m}$ )
AO-2 Graphene	14%	Ambient	4.04	5.15
		200 °C	3.80	4.86
	20%	Ambient	7.54	9.64
		200 °C	7.42	9.59
AO-4 Graphene	14%	Ambient	5.02	6.44
		200 °C	5.12	6.56
	20%	Ambient	5.45	6.71
		200 °C	5.96	7.42

#### 4.4.4 Wear Testing

Microscopy was performed on the wear tracks generated through wear testing. Profilometry allowed for the analysis of missing area on the surface of the material due to wear. From this data and the dimensions of the wear tracks, the wear rates of the samples were determined and are displayed in Table 5. Figures 56-59 show optical images of portions of the wear tracks that were observed under optical microscopy.

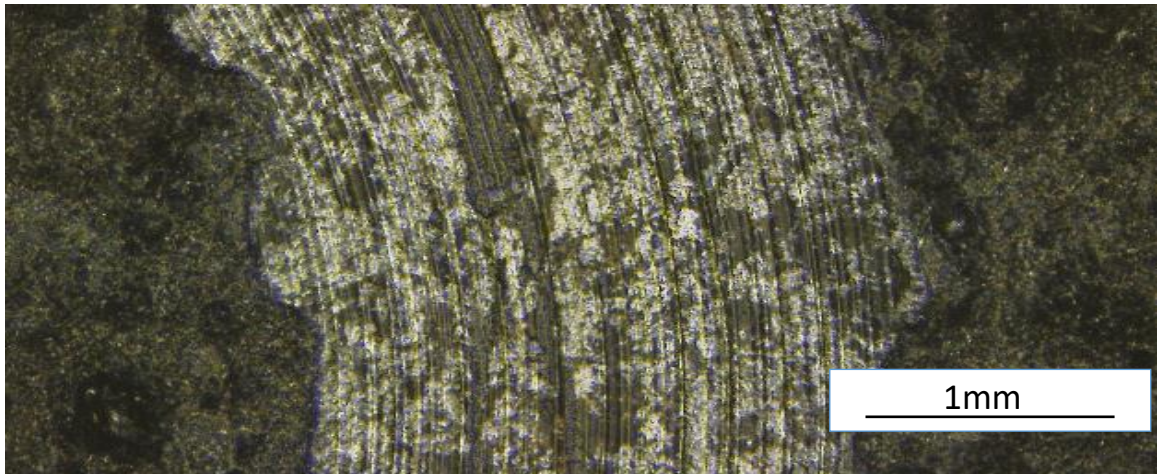


*Figure 57. Wear track of 20wt% AO-2 filled composite performed at ambient conditions.*

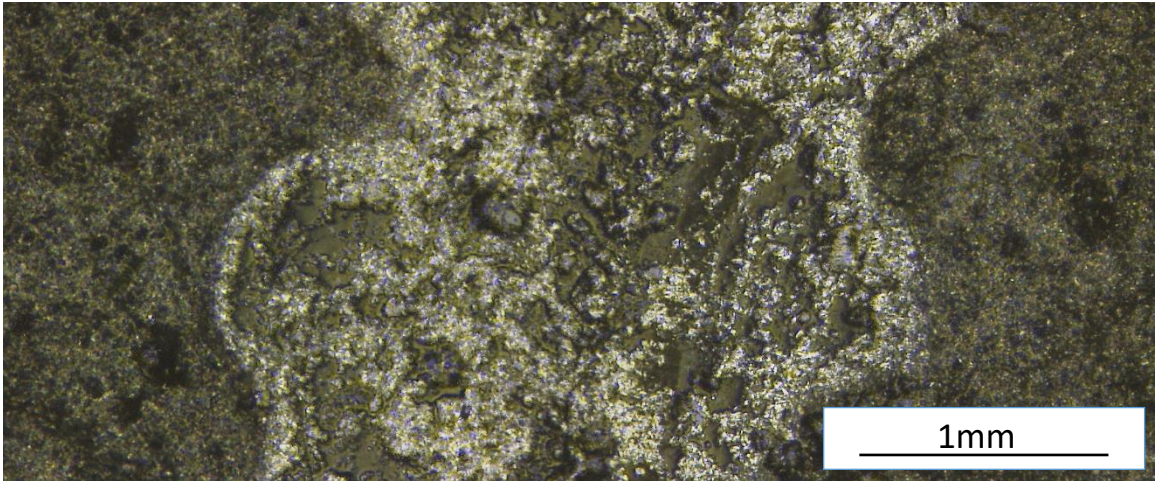


*Figure 58. Wear track of 20wt% AO-2 filled composite performed at 200°C.*

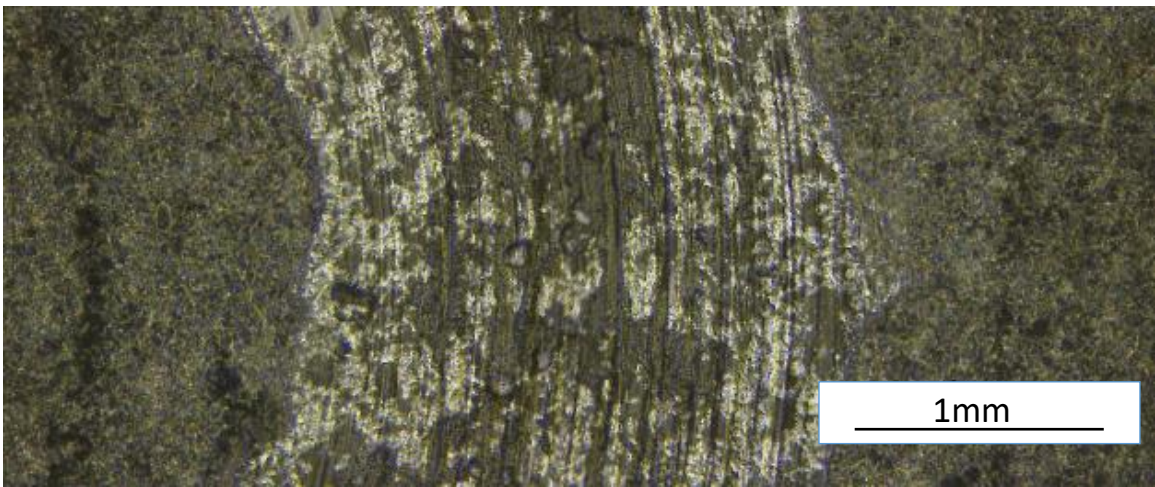


*Figure 59. Wear track of 20wt% AO-4 filled composite performed at ambient conditions.*

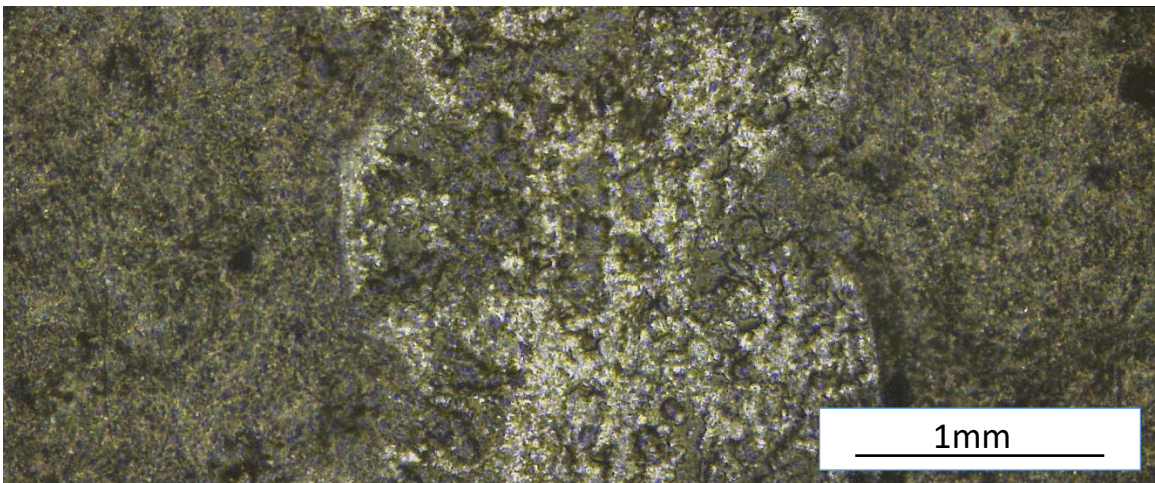


*Figure 60. Wear track of 20wt% AO-4 filled composite performed at 200°C.*

Clearly defined scratches are observable in the wear scars of the room temperature tests. These scratches are present throughout the wear scar. These scratches are less pronounced in the wear scars generated at higher temperatures. The edges of many of the wear scars are non-uniform. In some cases, this may be due to the surface roughness of the samples, with rough surfaces yielding non-uniform scars. It is important to note that the most extreme cases on non-uniformity in the wear scar are in the high temperature wear tests. This is most likely because of the temperature of the polymer. During wear testing, the temperature of the contact between the counterface and the coating can reach temperatures above the melting point of the polymer. It is possible that during wear, the polymer may have softened or melted in these areas, and when the samples were air cooled after testing, the polymer coating may have been reshaped. This is also the reason why the surfaces of the wear scars appear significantly different between high and low temperatures. This phenomenon will be further explained in the discussion section. Figure 60 and 61 show examples of the analysis performed to determine the wear area within the wear scar. Analysis of samples that underwent wear at ambient conditions as well at high temperature are displayed.

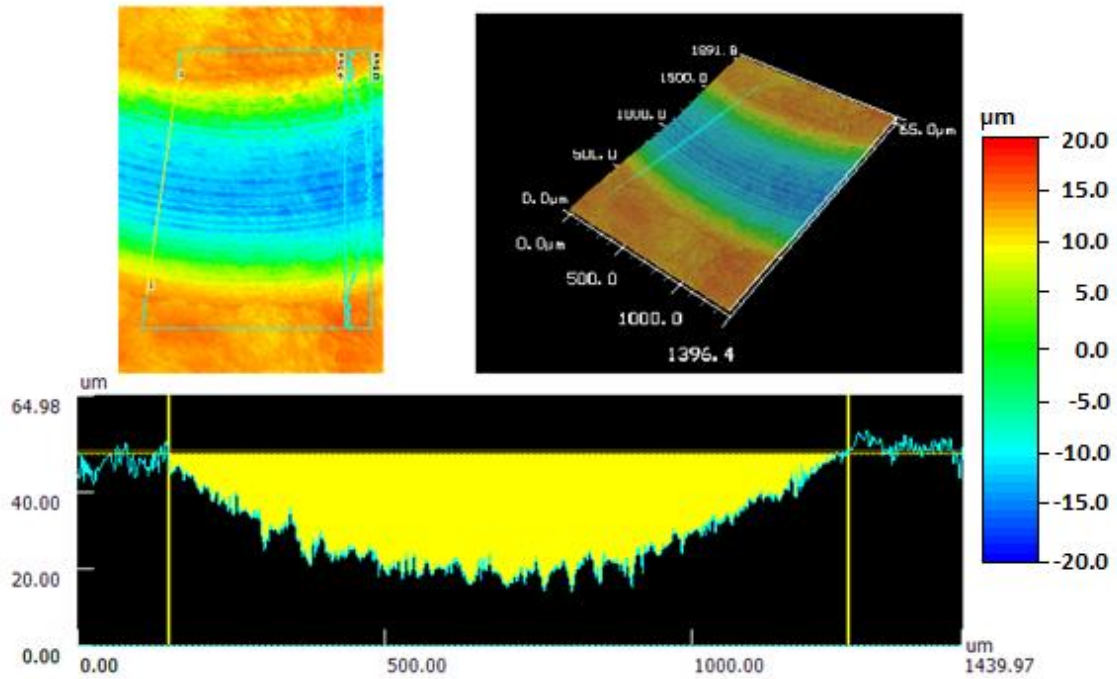


Figure 61. Analysis of wear scar at selected point perpendicular to wear direction in 14wt% AO-2 graphene sample undergoing ambient wear testing.

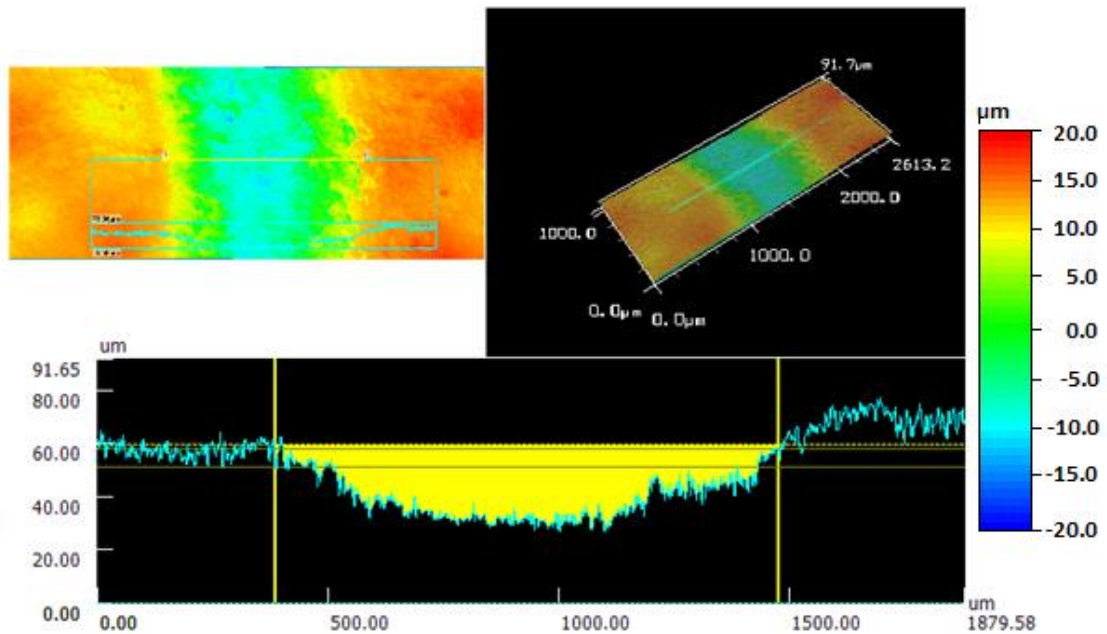
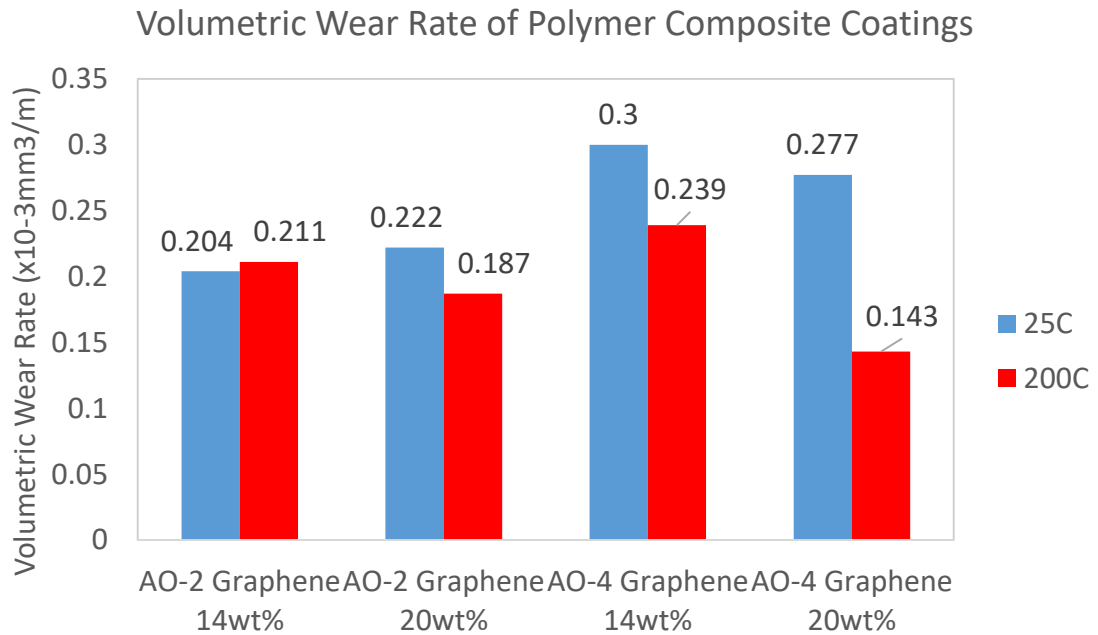


Figure 62. Analysis of wear scar at selected point perpendicular to wear direction in 14wt% AO-2 graphene sample undergoing wear testing at 200 °C.



From Figures 58 and 59, a clear difference in the roughness of the wear scar can be observed between the high temperature and room temperature testing. Figure 60 indicates a significant fluctuation in the depth of the wear scar for its entirety, while Figure 61 indicates a significantly smoother scar, except for a few sections of high depth variability. From this, it can be determined that the fluctuations in Figure 62 correspond to the visible scratches in the room temperature tests. The volumetric wear rates were calculated using the worn area, determined through wear scar analysis. These wear rates are displayed in Figure 62.



*Figure 63. Volumetric wear rates of polymer composite coatings.*

It is clear from the wear rates that the elevated temperature tests in most cases yielded decreases in the volumetric wear rates of the composite coatings. A slight elevation in the volumetric wear rate can be observed with an increase in temperature in the 14 wt%

AO-2 graphene sample. The coefficient of friction vs. sliding distance analysis are displayed in Figures 63-70.

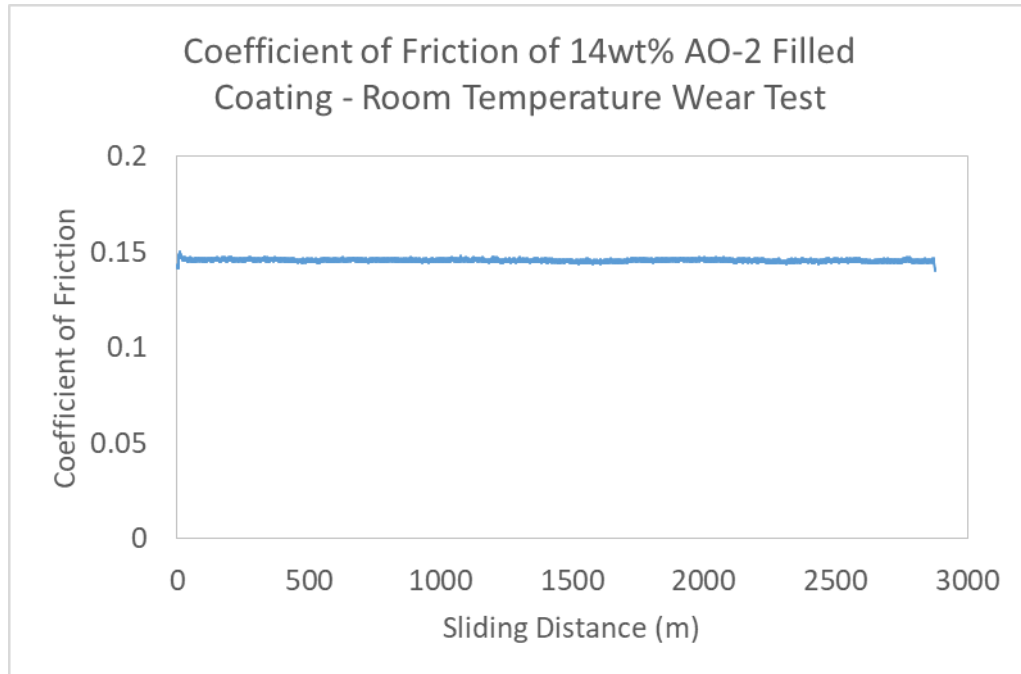


*Figure 64. Coefficient of friction vs. sliding distance of wear test of 14 wt% AO-2 graphene-filled coating at ambient temperature.*

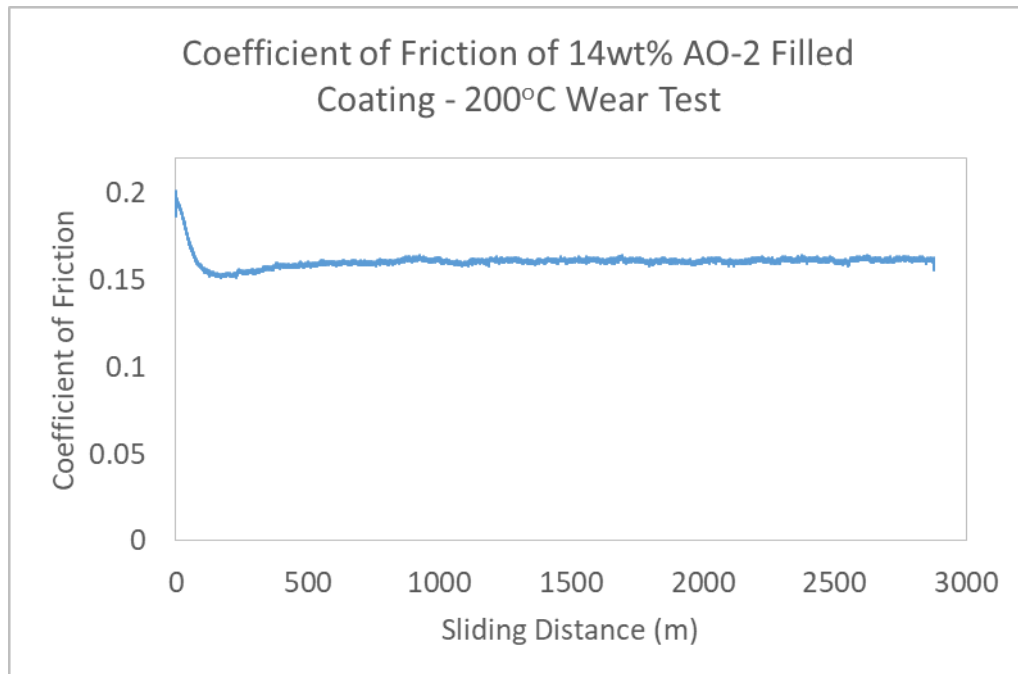


*Figure 65. Coefficient of friction vs. sliding distance of wear test of 14 wt% AO-2 graphene filled coating at 200°C.*

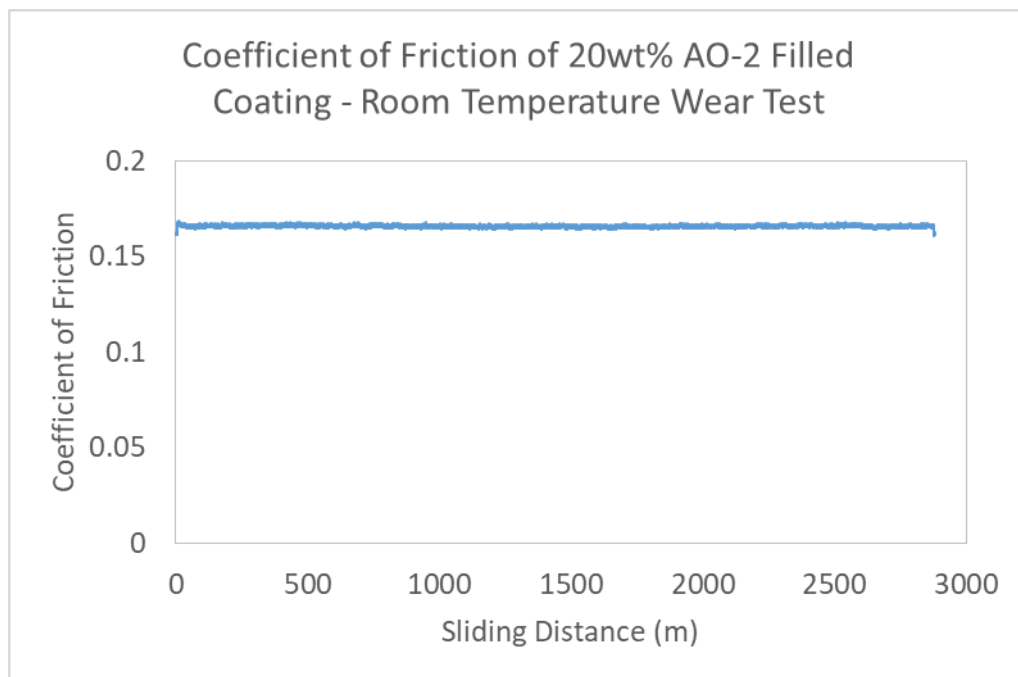


*Figure 66. Coefficient of friction vs. sliding distance of wear test of 20 wt% AO-2 graphene filled coating at ambient temperature.*

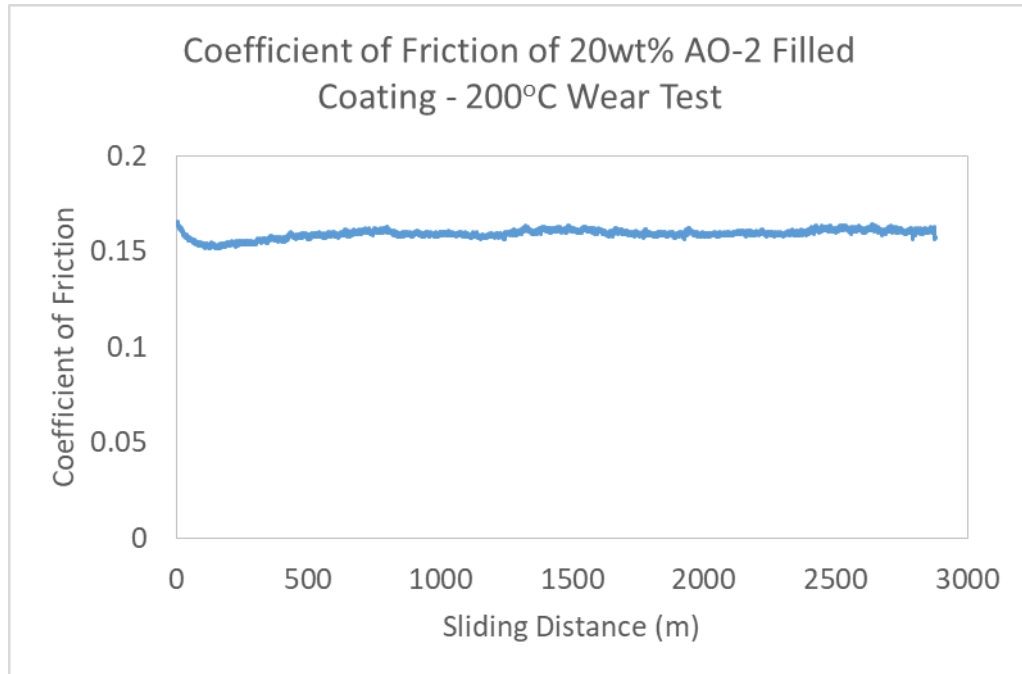


*Figure 67. Coefficient of friction vs. sliding distance of wear test of 20 wt% AO-2 graphene filled coating at 200°C.*

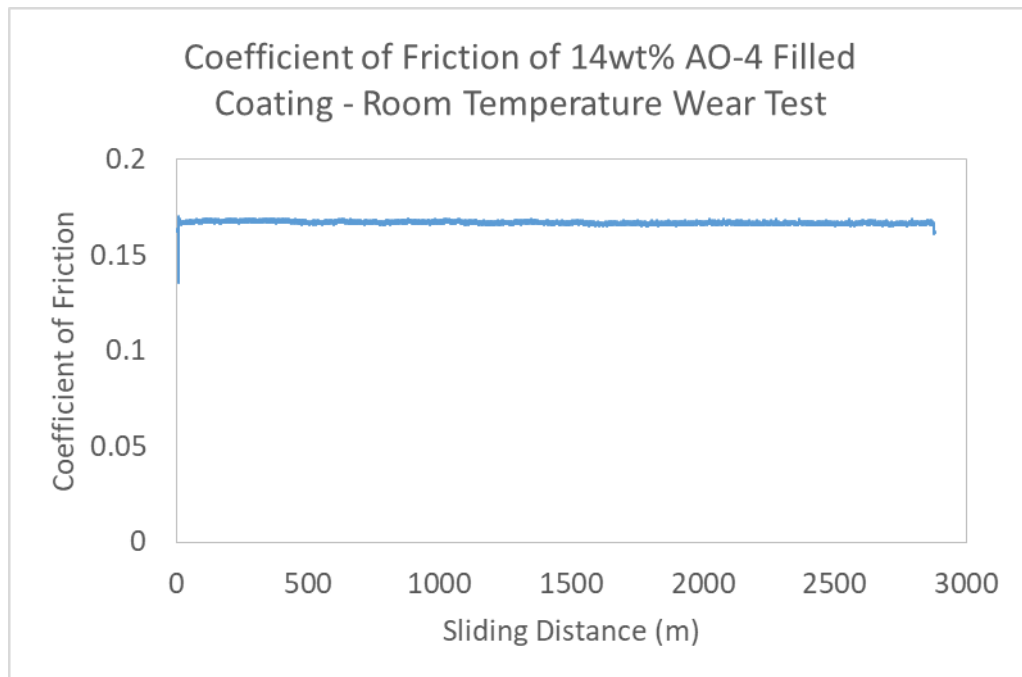


*Figure 68. Coefficient of friction vs. sliding distance of wear test of 14 wt% AO-4 graphene filled coating at ambient temperature.*

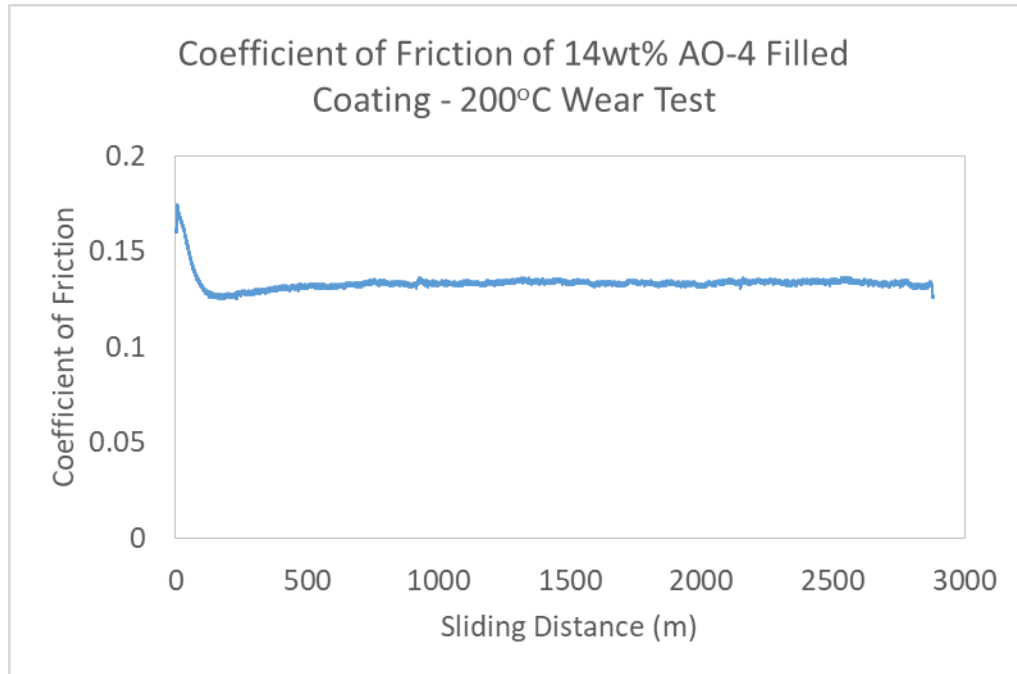


*Figure 69. Coefficient of friction vs. sliding distance of wear test of 14 wt% AO-4 graphene filled coating at 200°C.*

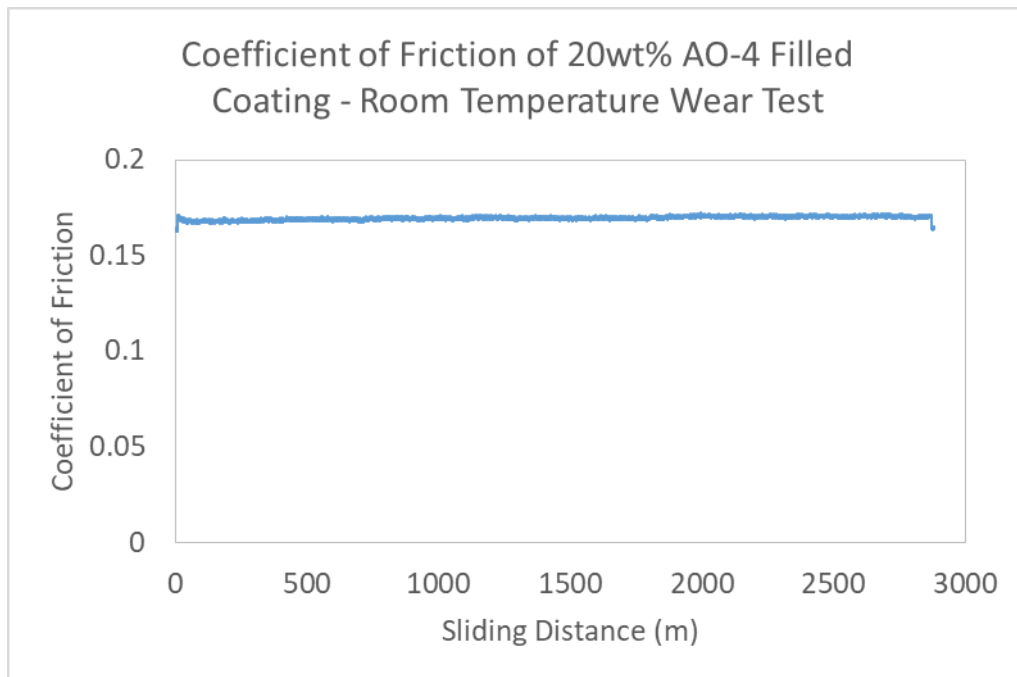


*Figure 70. Coefficient of friction vs. sliding distance of wear test of 20 wt% AO-4 graphene filled coating at ambient temperature.*

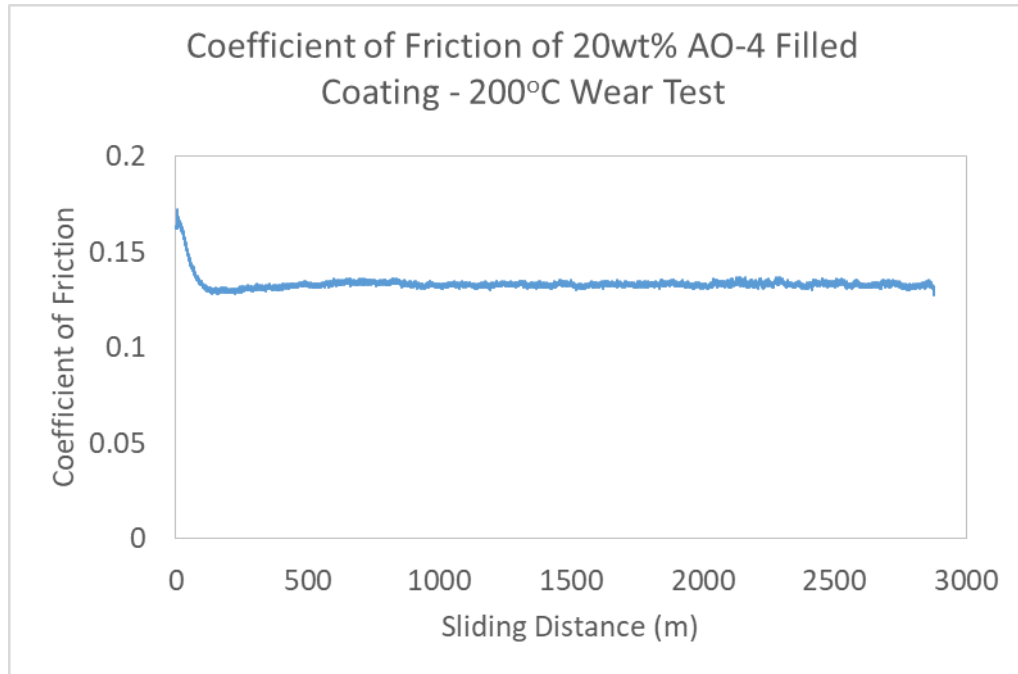


*Figure 71. Coefficient of friction vs. sliding distance of wear test of 20 wt% AO-4 graphene filled coating at 200 °C.*

It is clear from both the wear rate data as well as the frictional data that the wear at high temperature is significantly lower than at room temperature, with only one data point displaying the opposite relationship. In steady state conditions, the coefficient of friction values for the high temperature tests were lower than those at room temperature. The difference between these values is rather significant in many of the tests performed, especially the AO-4 graphene-filled samples. Observations of the cross-sections of the coatings did show significantly larger particles within the AO-4 graphene-filled samples when compared to the AO-2 graphene-filled samples.

Steady-state wear is determined through fluctuations in the coefficient of friction recorded through analysis of the wear data. It is the point at which wear is occurring in the bulk material. Surfaces of coatings may have different consistency from the internal

sections of the materials, and in some cases a thin layer of oxide in the case of wear on metals may be present. A stable coefficient of friction, one indicating very little variability with respect to the increases in the sliding distances, is an indicator for steady-state wear. It appears that steady-state wear of the room temperature wear tests was achieved at significantly low sliding distances. Steady-state wear was achieved almost immediately, with very few cycles before a constant frictional force (coefficient of friction) was achieved. By contrast, it appears that significant sliding distances were required for steady state wear to be achieved in high temperature testing. It is possible that the time for the coating to soften or melt at the temperatures the test was performed may have resulted in the significant increase in the sliding distance required to reach steady state.

Images of the counterfaces of the wear testing are shown in Figures 71 and 72. Sections of polymer are observed on the surface of a counterface of room temperature testing, which have been transferred from the polymer coating because of wear. A slight amount of wear on the top right section of the counterface is also observed. Significantly more damage is observed in high temperature wear testing. Damage to the counterface is not expected due to the softening of the polymer coating during high temperature wear testing. It is possible that an oxide layer formed, which was then worn off during testing. The edges of Figure 71 show black sections of the counterface. Visual observations of the counterface also show this darkening of the surface. The area in contact with the composite coating however shows none of this dark layer, which may have been the layer that was worn off during testing.

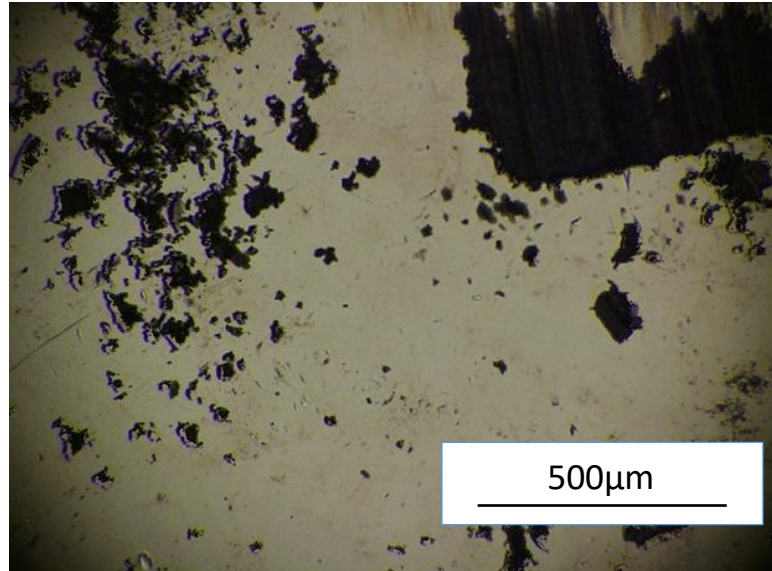


*Figure 72. Counterface surface after wear testing performed at ambient conditions on coating containing 20 wt% AO-2 graphene.*

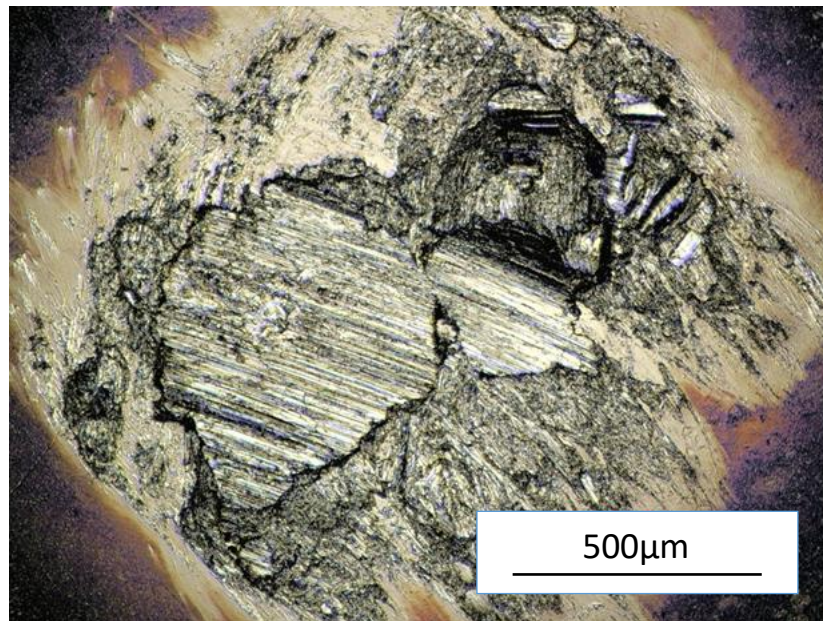


*Figure 73. Counterface surface after wear testing performed at 200°C on coating containing 20 wt% AO-2 graphene.*



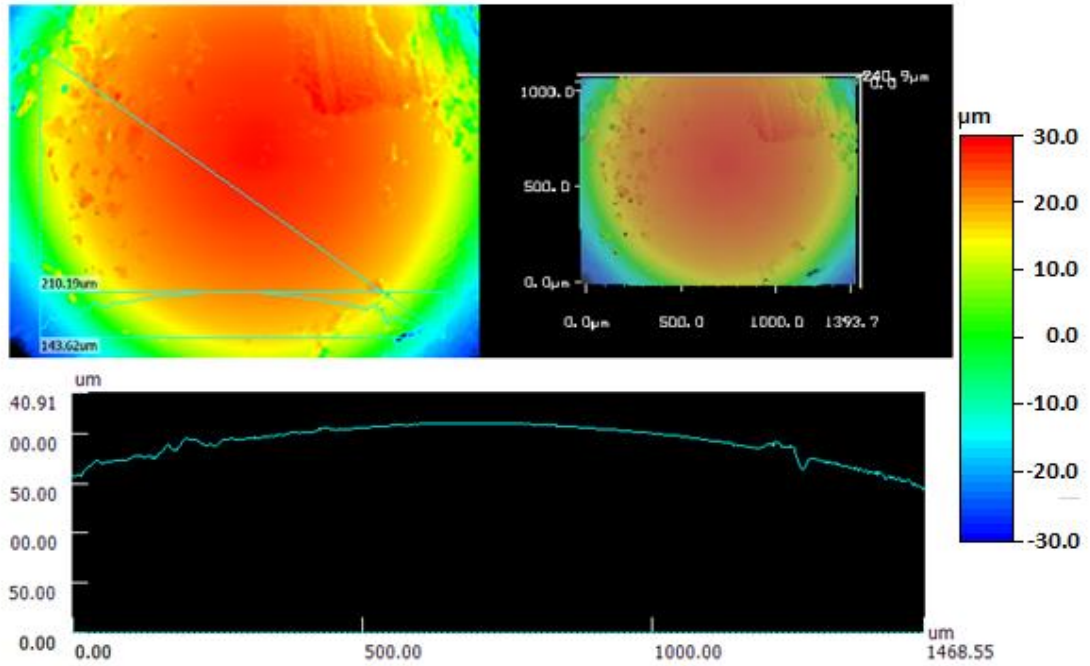


Figure 74. Counterface surface topography after wear testing performed at ambient conditions on coating containing 20 wt% AO-2 graphene.

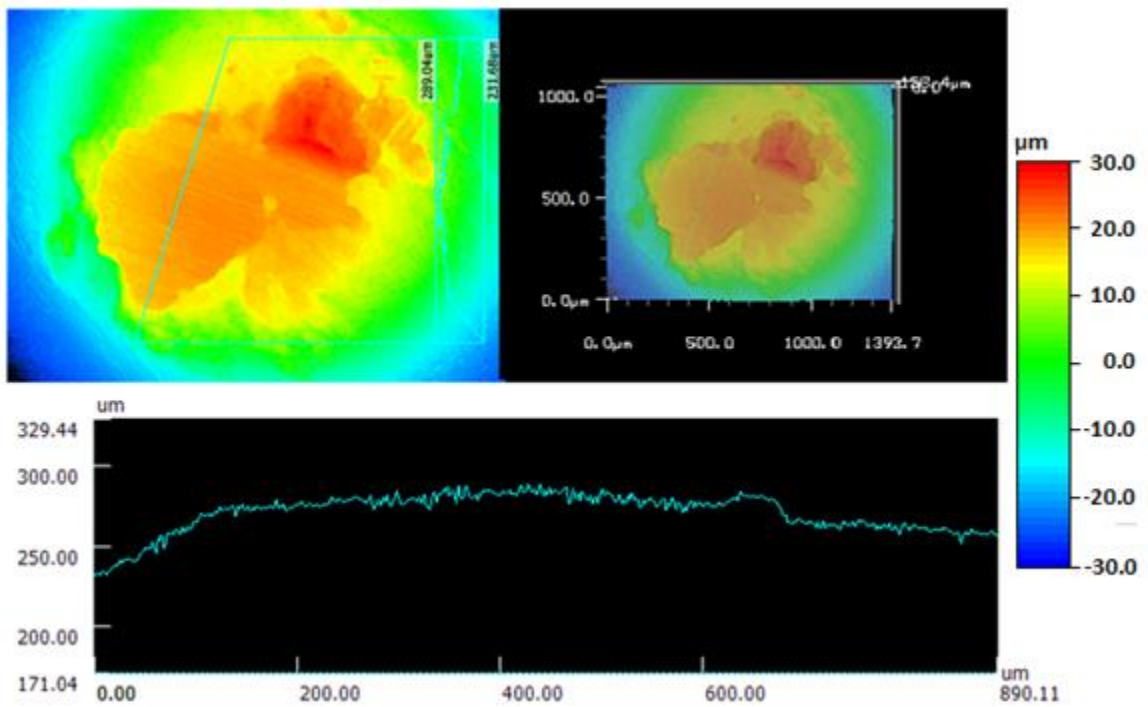


Figure 75. Counterface surface topography after wear testing performed at 200 °C on coating containing 20 wt% AO-2 graphene.

Figures 73 and 74 show the surface topography of the counterface after wear testing. Figure 73 shows a considerably smooth surface except for the top right section, which based on the intensity of the colour, shows a bit of damage to the counterface occurred. Figure 74 shows significant fluctuations in the surface topography of the counterface.
















#### **4.4.5 Corrosion Test**

A total of fifteen coated samples were subjected to corrosion test to determine the resistance of the polymer coating to highly acidic environments. The samples were immersed in an 80% sulphuric acid heated at 85 °C for more than 1500 hours. After testing, images of the samples were taken and are displayed in Table 6. It is clear from these images that samples containing either of the graphene fillers displayed no visible damage. The 14 wt% AO-4 grade graphene sample does exhibit a rough surface; however, this is due to a variability in the surface finish of the samples after coating. No difference was observed in this sample when comparing before and after corrosion testing. Very limited mass gain or loss was observed in any of the samples after testing, with mass variations below 50 mg.

The MWCNT samples with weight fractions of 10% and above exhibit apparent discoloration after corrosion test. This may be due to the penetration of the acid through the coating and corrodes the substrates. In the 20 wt% sample, pitting appears to occur in some areas. This is expected, as after coating, the surfaces of the 20 wt% samples were rough, and the coating did not show good quality. Nevertheless, the masses of each sample did not show significant difference before and after corrosion, which indicates that

although some of the coatings have been damaged, the corrosion of the substrate has just started and does not cause apparent mass gain/loss yet.

*Table 6. The (a) AO-2 Grade Graphene, (b) AO-4 Grade Graphene, and (c) MWCNT samples after corrosion testing.*

Filler Type	Filler Weight Percent				
	1 wt%	5 wt%	10 wt%	14 wt%	20 wt%
(a) AO-2 Grade Graphene					
(b) AO-4 Grade Graphene					
(c) MW- CNT					

Graphene filled coatings were shown to have good adhesion to the substrate and good durability. Characterization of the durability of the MWCNT filled coatings was not performed due to their poor thermal properties in the compression molded analogues, as well as their coating quality. Graphene filled coatings, and MWCNT coatings containing <10 wt% displayed good corrosion resistance, while MWCNT filled coating containing

$\geq 10$  wt% indicated significant corrosion on the coating in the form of pitting and coating penetration.

## **Chapter 5. Discussion**

This chapter discusses in detail the results obtained through experimentation. This will be separated into two sections. The first will detail the results pertaining to the composite disks. This includes microscopy and how it is related to thermal and electrical properties. The second section will detail the microstructural, mechanical, tribological and corrosion resistant properties of the composite coatings.

### **5.1 Composite Disks**

The microstructures of the composite disks shown in Figures 17-19 clearly indicate that in the composites containing graphene fillers, a clear network of filler material is established in all the weight fractions. Within higher weight fraction samples, the network observed appears larger and much more defined. High variability in the area fraction is observed in low weight fractions of the samples, as observed in Figure 20. The minimal amount of filler at low weight fractions allows the particles to reorient unobstructed through the molten polymer. As the filler content increases, the free area that the filler can move through during compression decreases, leading to greater restriction in the manner the filler material can move. This is contrasted by the composites containing multi-walled carbon nanotube fillers, which displayed agglomeration of filler material. Higher weight fractions within these samples yielded larger or more abundant agglomerates. It is postulated that this network is formed due to the pressure applied to the mixed powder during curing. During compression at the polymer melting point, the polymer is pushed perpendicular to the compression axis. The filler particles are pulled in the direction of the flow. This results in the alignment of the filler materials perpendicular to the compression

axis, and thus a network is formed. This is important to note when compared to the microstructures of composite coatings, which will be discussed in detail in section 5.2.

SEM performed on the fracture surfaces of composite disks yield results that are corroborated by filler material properties in Table 3. It can be observed in Figures 21-29 that samples containing AO-2 grade graphene displayed much smaller graphene flakes when compared to samples containing AO-4 grade graphene. Graphene flakes are visible under magnification as low as 2,000 $\times$ ; however, MWCNT filler requires magnification near 10,000 $\times$  to visibly observe the filler material. Fracture surfaces of low filler content composite disks appear very similar; however, with increasing MWCNT filler content, a greater amount of plastic deformation is visible that is not present in graphene-filled composites. It appears that the introduction of filler material results in a more brittle fracture mechanism; however, MWCNT filler results in significantly more deformation before fracture. Within the composites containing graphene filler, a more brittle fracture is expected. The interface between the graphene filler and polymer matrix spans the entire sample, in the form of the network that can be observed in Figures 17 and 18. The fracture occurs along this interface, as opposed to through the polymer matrix, resulting in limited deformation of the polymer matrix before fracture. Conversely in the MWCNT filled composites, fracture must occur through the polymer, as the MWCNT agglomerates have limited connectivity throughout the material.

The thermal results obtained for composite disks in Figures 30, 32-33 displayed very little correlation between weight fraction and specific heat. It is also clear that while there are differences present within the microstructures, all composites containing any of the three filler materials yielded very similar specific heat values. It can be assumed that

due to these two facts, the specific heat of these composites is mainly controlled by the matrix of the sample, with very little influence from the filler materials. Conversely, a very clear correlation between weight fraction of filler and thermal diffusivity is observed in Figures 34-36, with increases in weight fraction yielding increases in thermal diffusivity. Specific heat is the measure of the amount of heat per unit mass to raise the temperature of the sample by one degree Celsius. The polymer makes up the majority of the samples for all weight fractions, and is the factor that controls the specific heat. This explains why the specific heat essentially has no reliance on the filler content. Conversely, the thermal diffusivity is the measure of the heat transfer rate from hot to cold through a material. This property is heavily dependent on the number of heat transfer pathways through a material. Due to the filler materials having significantly higher thermal conductivities compared to the polymer matrix, the network acts as a pathway for thermal conduction. With a greater filler content, the size of the filler network increases, resulting in higher thermal diffusivities.

Very little difference can be observed in the thermal diffusivities of composites filled with different grades of graphene, with only the 14 wt% filled samples yielding a significant difference. This variation is possibly due to inconsistencies of filler within the composite. Given that sectioning of the disk was required for thermal diffusivity analysis, it is possible that the location chosen for testing may have had an abundance or absence of filler material, resulting in significant differences in thermal diffusivities between different grades of graphene. It is also possible that due to the way the filler particles orient themselves in the microstructure that the size of the particles plays no role in the thermal diffusivity. A network of similar shape and size is formed in both graphene filled

microstructures, resulting in very similar thermal properties. Unlike the results observed for the specific heats of samples, a significant difference in thermal diffusivity is seen between graphene-filled and MWCNT-filled composites. It can be observed that the highest diffusivity for MWCNT-filled samples (20wt% filled samples) is slightly higher than those of 5wt% of graphene filled composites. This is also expected given the microstructure of the MWCNT filled samples. Unlike in graphene-filled composites, the MWCNT filler formed clusters of particles, and were not connected throughout the material. Due to this, the energy diffused through the samples did not have an easy pathway to follow and had to travel through bulk polymer. This resulted in the significantly lower thermal diffusivity of the MWCNT-filled samples.

Thermal conductivity values in Figures 37-39 showed similar patterns to the thermal diffusivity. Both graphene-filled composites yielded similar thermal conductivity values, with the exception of the 14 wt% sample mentioned previously. A maximum thermal conductivity value of approximately 1.60 W/mK was obtained for the 20 wt% AO-4 graphene-filled composite at room temperature. Prior work performed on this polymer matrix with graphite as a filler material at 20 wt% yielded 0.8 W/mK [9]. An approximate increase of 100% is observed. From the prior research, it was also determined that samples of 30 wt% graphite yielded a thermal conductivity of 1.4 W/mK, which is even smaller than that with 20 wt% graphene[10]. Unlike in the prior research, which showed no concrete relationship between temperature and thermal conductivity, a significant decrease in thermal conductivity with temperature is observed in this research. Methods of specific heat measurement in this study were different than those in the study by He. et al., which led to the difference in trends of thermal conductivity[10].



It is also observed that the highest thermal conductivity achieved for MWCNT-filled composites is approximately 0.5 W/mK at room temperature for 20 wt% filled samples, which is significantly lower than that of the graphite samples in the reviewed literature. From the acquired data, significant improvements to the thermal conductivity of polymer composite disks was achieved, with graphene-filled samples of both grades yielding similar results, and MWCNT-filled samples yielding poor thermal properties. Graphene and MWCNTs are well known for their superior thermal properties; however, the incorporation of these materials into the polymer matrix does not induce a large increase on the overall thermal conductivity of the composite as compared to that of the filler material. Carbon nanomaterials have significant anisotropy, leading to directional variations in their thermal properties, i.e. the thermal conductivity in one direction is significantly higher than in the other direction. The processing methods used to prepare and mold the mixed composite particles resulted in the random orientation of filler particles. Thus, the filler particles were not aligned to optimize the thermal conductivity in the direction of the thermal flow, resulting in limited thermal conductivity values.

Electrical surface resistivity measurements were also performed on composite coupon samples. These results, shown in Figure 40, display that both grades of graphene yielded extremely similar resistivity values, with significant variation occurring only at 5 wt% for these samples. MWCNT-filled samples yielded significantly higher resistivity values at low filler loads, with no results being obtained at 5 wt% due to extremely limited conductivity. Resistivity values comparable to graphene-filled composites are only observed in samples near 20 wt%. This can be explained in much the same way that the difference in the thermal properties between filler types was explained. In both graphene

samples, a network of particles is formed, providing pathways in which electrons can travel easily. At lower filler content these pathways are less defined and a greater resistance to electron motion is observed. This network is not present in MWCNT-filled samples, thus a significant difference in the resistance is expected at lower weight fractions. At high weight fractions, the sheer number of agglomerates results in an ease of electron transfer, thus lower resistance values are observed.

## **5.2 Composite Coatings**

Microstructural observation performed on composite coatings provided significantly different results from that performed on composite disks. The compression-molded disks were approximately 2 mm in thickness, allowing for a greater area of observation, whereas the coatings are much thinner, at approximately 250 microns. Consequently, some of the structures observed in the compression-molded disks are still present in the coated samples, but they do not appear as obvious, and the observable area is much smaller. Observations of graphene-filled coatings indicate the presence of a random dispersion of filler materials. Orientation of the particles is random and large sections of the coating are absent of filler particles. A distinct network of graphene particles was not present in these microstructures. The reason for this can be directly drawn from the method of fabrication. During compression molding, a constant pressure was applied to the composite melt, leading to a flow of the polymer, which dragged the filler material to align in the direction perpendicular to the compression direction. During curing of the coatings after electrostatic spray coating, there was no pressure applied, and the particles remained in the position that they were sprayed. Thus, the graphene within the coatings is randomly dispersed, with variable orientation within the matrix.

MWCNT-filled coatings displayed significant agglomeration of particles within the polymer matrix. The thicknesses of the MWCNT-filled coatings were also significantly lower than the graphene-filled coatings. This is attributed to the poor dispersion of filler particles within these coatings. The polymer matrix did not have good cohesion, resulting in the loss of material at the surface. The poor surface finish and difficulty in building thick coatings during electrostatic spray indicate that the MWCNT is not a suitable filler material for the application. Structurally, the compression molded disks and the coatings were quite similar. Large agglomerations of particles were observed randomly distributed throughout both microstructures. This leads to the belief that the clustering of MWCNT particles occurred in the mixing stage of the fabrication process. Both samples also indicated poor cohesion of the matrix at high weight fractions. When comparing area fraction of particles with those of the composite disks, it is clear that the coatings have significantly smaller area fraction of filler with the highest area percentage of 13.14% in the 20 wt% MWCNT samples, which is less than half than that of the composite disks at that weight fraction. Thus, it can be expected that the properties measured for composite disks are not entirely applicable to the coatings that have been generated. Optimization of the spray coating method to generate coatings with a more analogous microstructure to that of the disks would allow for a more appropriate comparison.

Scratch tests were performed to determine whether the coatings would delaminate when subjected to stress. Due to the poor coating quality of MWCNT-filled samples, measurements were only performed on the 20 wt% graphene-filled coatings. Through measurement of the frictional force during scratching, it was determined that during steady state, the coefficient of friction of both graphene-filled composites was approximately 0.4.

This result is similar to those achieved by He et al. [35], which performed scratch testing on similar grades of PFA with ceramic and graphite fillers. The coatings generated in this thesis did not delaminate under the highest load of 28 N, and the steel substrate was not reached during the scratch. This is identified because the BSE images do not show areas of brightness, which would be an indicator to the presence of steel in the image. On both scratch tracks, a point of interest is noted at approximately 3.5 mm along the track. In the AO-2 graphene-filled sample, there appears to be a section of polymer that was torn and may have been dragged by the scratch head for a significant distance. This may have resulted in the significant fluctuations in the coefficient of friction of this sample at approximately 3.5 mm and beyond. At the same region in the AO-4 graphene filled sample, a void is present. This may have been a cluster of filler material or a region of poor cohesion that may have been removed due to the pressure applied by the indenter. This may also have resulted in the fluctuations located at 3.5 mm to 4 mm in the coefficient of friction figure for this sample. The damage to the coatings at the same point may be an indication of a critical loading. This is the point at which a coating begins to break down, or exhibit a loss to adhesion [44]. This point is indicated by damage to the coating at the specific load of 19.5 N. The fluctuations in the coefficient of friction may also have resulted from minor slipping of the coating due to reaching this critical load.

Other than these sections, several chevrons present at the edges of the track, indicating a separation of the matrix during scratching; however, no failure of the coating is observed, indicating good adhesion of the coating. Scratch depth figures depict the deepest point of the scratch was at maximum 125 microns. Given that the thickness of the top coating is 50 microns, it can be assumed that scratch testing did not reach the primer

coating, thus the entirety of the scratch took place in the composite portion of the coating. As such, it is not expected that any fluctuations present in the coefficient of friction are due to differences in the topcoat and primer layer.

Surface roughness measurements were performed on the samples that were to undergo wear testing. From the results in Table 5, it is observed that the surfaces of the higher weight fraction samples tended to have higher surface roughness. This is expected, as a greater amount of filler may disrupt the cohesion between filler and matrix. It is important to note that the majority of the surface finishes of coatings was controlled by the powder morphology during the curing process. Some generated samples of higher weight fractions were observably smoother than those of lower weight fractions. This phenomenon is more readily visible when observing the corrosion results of the coatings and will be discussed in detail. Samples that underwent wear testing were chosen due to their surface finishes observable with naked eyes.

Wear rates were calculated through microscopic analysis of wear tracks. Several sections along each wear track were analyzed for the area of the wear scar. Given the radius of the wear scar, the wear rates were determined. It is clear from these results that higher temperature tests resulted in lower wear rates with the exception of the AO-2 14 wt% graphene samples, which had a slight increase in the wear rate at higher temperature. Comparatively, a reduction in the coefficient of friction in the steady state portion of testing with an increase in temperature is seen, with the exception of the AO-2 14 wt% samples, which yielded a slight increase in the coefficient of friction with an increase in temperature. All coefficient of friction data indicated a near constant coefficient of friction, with no significant increases or decreases in steady state. It is also observable that the wear profiles

of the higher temperature tests are significantly smoother than those of the room temperature test. It is possible that during testing, the contact point between the stainless steel counterface and the polymer reached temperatures above the melting point of the polymer, resulting in a gliding of the counterface, thus leading to significantly lower wear rates [45], [46]. It is also possible that an ironing effect was present during wear testing, also as a result of the higher contact temperature. AO-2 graphene flakes have much smaller layer thicknesses compared to AO-4 graphene. This may lead to stronger bonding between the filler material and the polymer matrix in the AO-2 samples. The stronger bonding yields an increase in the hardness of the sample, which may explain the larger wear rate in the AO-4 filled samples than the AO-2 filled samples at room temperature[47], [48].

Microscopic images of the wear scars and counterfaces are displayed in Figures 56-59, 71-72. The outer edges of the wear tracks in the high temperature wear testing were much less uniform than those at room temperature. Elevated temperatures result in thermal softening of the polymer, reducing the force restricting the steel counterface causing significant deformation at the outer edges of the wear track. A combination of abrasive and adhesive wear was observed through analysis of the wear scars and the counterface balls. A majority of the composite coating was deformed and pushed to the outer edges of the wear scar. This phenomenon is known as ploughing, which is a form of abrasive wear. The point of contact between the counterface and the coating reached extremely high temperatures, and portions of the coating adhered to the counterface. Since there was adhesion of the coating on the counterface, it is possible that the sliding action present during wear testing was between the coating and sections of the transferred coating rather than the counterface. This would result in a reduction in the coefficient of friction and wear

rate, and may be the reason that the high temperature wear testing resulting in lower coefficient of friction and wear rate. Observation of the counterface used in high temperature wear testing showed blackened edges, and severe scratches at the point of contact. The blackened edges indicate the formation of an oxide layer due to the heat from the heat gun. It is possible that this thin oxide layer was worn during the wear testing instead of the counterface, resulting in the scratches.

Several samples underwent extreme corrosion testing. Images of the surfaces of the samples in Table 6 indicated that in all graphene-filled samples, no corrosion was observed. The same can be said of the 1 wt% and 5 wt% MWCNT samples. However, samples containing greater than 10 wt% MWCNT showed apparent discoloration. The surface finish of these samples was of poor quality, which resulted in the poor performance of the samples during corrosion testing. If the surface of the coating is very rough, or there are sections of the coating that are much thinner than others, they will be more susceptible to corrosion. As observed in microscopy of the MWCNT-filled coatings, the surface finish was very poor. However, it is believed that a combination of the poor cohesion of MWCNT particles within the coating as well as the coating thickness is the cause of the poor corrosion resistance. It is observed that the graphene coatings are resistant to extremely corrosive environments, and thus are of good quality for the proposed application.

## Chapter 6. Conclusions

The final chapter is a restatement of the significant findings resulting from this research, as well as recommendation for future work which could further develop thermally conductive barrier coatings containing carbon nanomaterial filler.

### 6.1 Conclusions

- Compression molded samples showed an even distribution of graphene filler in the polymer matrix, forming a network of particles throughout the material. MWCNT filler particles clustered in large agglomerates, and did not form a network.
- The graphene-filled composites yielded a significant increase in the thermal conductivity, up to 1.6 W/mK at 20 wt% of both filler materials at room temperature as compared to virgin PFA (an 8× increase). The MWCNT-filled composites only achieved 0.5 W/mK at the same weight percentage at room temperature.
- Both composites containing graphene filler exhibited low electrical resistivity, and were comparable between each other across all filler content. MWCNT samples at low filler content exhibited extremely high electrical resistance (too high to measure below 10 wt%), but close to those of graphene at high filler content (20 wt%).
- The composite coatings containing graphene filler exhibited good surface finish and uniform thickness, while those containing high filler content MWCNT exhibited poor surface finish, and extremely variable thickness. Microstructures appeared similar to those of compression-molded samples; however, a distinct



network of graphene particles was not observed to the same degree in composite coatings. Agglomerates of MWCNT were clearly observable in samples containing MWCNT filler.

- Durability testing showed that graphene-filled coatings did not delaminate during microscratch testing, although material tearing was observed. Wear testing of the coatings exhibited lower coefficients of friction at higher temperatures. The wear rates of 20 wt% AO-4 graphene-filled composites yielded a higher wear rate at room temperature ( $0.277 \times 10^{-3} \text{ mm}^3/\text{min}$ ) when compared to AO-2 graphene-filled composites at the same weight fraction ( $0.222 \times 10^{-3} \text{ mm}^3/\text{min}$ ), but a lower wear rate ( $0.143 \times 10^{-3} \text{ mm}^3/\text{min}$  compared to  $0.187 \times 10^{-3} \text{ mm}^3/\text{min}$  for AO-2) at  $200^\circ\text{C}$ . A combination of abrasive and adhesive wear was observed during all tests.
- Composite coatings showed very minimal mass gain or loss after immersion in 80% sulphuric acid at  $85^\circ\text{C}$  for 1500 hours. Discolouration was observed in samples containing greater than 10 wt% MWCNT, indicating the onset of corrosion, while no samples containing graphene indicated any form of corrosion.
- For coating application in low-temperature heat exchangers, AO-4 would be a more feasible filler material for the polymer composite barrier coating. Both graphene filled composites yielded very similar results, and were shown to have better thermal properties than the MWCNT filled composites. AO-4 graphene is the less expensive of the two grades of graphene, as the particles are much larger than the AO-2 grade graphene.

## **6.2 Recommendations**

Characterization of the thermal and electrical properties of the composite coatings should be performed in further research. The microstructure of the compression molded samples and coatings were not identical, and thus the thermal properties determined are not expected to be identical to those of the coatings. Methods of aligning the carbon nanomaterials within the polymer matrix may also yield significant increases in the thermal properties of the composite materials. Evaluation of the thickness of the composite coating and of the primer, and their effect on thermal and durability properties may also be performed. An analysis of the wettability of the coating may also be performed to understand the mechanics of condensation of water and acids on the surface of the coatings.

## References

- [1] I. B. Page, *Waste Heat Recovery: Technology and Opportunities in U.S. Industry*. U. S. Department of Energy. 2008.
- [2] Q. Zhuang, P. Geddis, B. Clements, and V. Ko, “Corrosion-resistant coating development with potential application in equipment of low-temperature waste heat recovery,” *Can. J. Chem. Eng.*, vol. 96, no. 1, pp. 101–106, 2018.
- [3] M. J. Li, S. Z. Tang, F. long Wang, Q. X. Zhao, and W. Q. Tao, “Gas-side fouling, erosion and corrosion of heat exchangers for middle/low temperature waste heat utilization: A review on simulation and experiment,” *Appl. Therm. Eng.*, vol. 126, pp. 737–761, 2017.
- [4] W. De Jesus, M. C. Pereira, and R. Zenhei, “Localized Corrosion of 7Xxx-T7 Aluminum Alloys,” *Tech. Contrib. to XX intl Congr. ABM, Brazil*, pp. 1–5, 2007.
- [5] M. P. Schwartz, “Four Types of Heat Exchanger Failures . . . mechanical, chemically induced corrosion, combination of mechanical and chemically induced corrosion, and scale, mud, and algae fouling.”
- [6] L. Fedrizzi, F. Andreatta, L. Paussa, F. Deflorian, and S. Maschio, “Heat exchangers corrosion protection by using organic coatings,” *Prog. Org. Coatings*, vol. 63, no. 3, pp. 299–306, 2008.
- [7] N. K. Dhama, M. S. Reddy, and A. Mukherjee, “We are IntechOpen , the world ’ s leading publisher of Open Access books Built by scientists , for scientists TOP 1 % Control of a Proportional Hydraulic System,” *Waste Water - Eval. Manag.*, vol.

2, pp. 137–164, 2012.

- [8] E. Leivo, T. Wilenius, T. Kinos, P. Vuoristo, and T. Mäntylä, “Properties of thermally sprayed fluoropolymer PVDF, ECTFE, PFA and FEP coatings,” *Prog. Org. Coatings*, vol. 49, no. 1, pp. 69–73, 2004.
- [9] Y. He, R. Santos, R. Zhang, P. Liu, D. Walsh, and J. Lo, “Youliang He, Raul Santos, Ruby Zhang, Pei Liu, Dan Walsh and Jason Lo,” 2013.
- [10] Y. He, D. Walsh, and C. Shi, “Fluoropolymer composite coating for condensing heat exchangers: Characterization of the mechanical, tribological and thermal properties,” *Appl. Therm. Eng.*, vol. 91, pp. 387–398, 2015.
- [11] G. W. Hanson and S. Member, “Hanson - nano\_antennas 2005.pdf,” vol. 53, no. 11, pp. 3426–3435, 2005.
- [12] U. K. Sur, “Graphene: A Rising Star on the Horizon of Materials Science,” *Int. J. Electrochem.*, vol. 2012, pp. 1–12, 2012.
- [13] P. R. Verdonck, U. Siller, D. S. De Wachter, F. De Somer, and G. Van Nooten, “Hydrodynamical comparison of aortic arch cannulae,” *Int. J. Artif. Organs*, vol. 21, no. 11, pp. 705–713, 1998.
- [14] D. Verma, P. C. Gope, A. Shandilya, and A. Gupta, “Mechanical-Thermal-Electrical and Morphological Properties of Graphene Reinforced Polymer Composites: A Review,” *Trans. Indian Inst. Met.*, vol. 67, pp. 803–816, 2014.
- [15] A. Li, C. Zhang, and Y. F. Zhang, “Thermal conductivity of graphene-polymer composites: Mechanisms, properties, and applications,” *Polymers (Basel)*, vol. 9,

no. 9, pp. 1–17, 2017.

- [16] A. A. Balandin, “Thermal properties of graphene and nanostructured carbon materials,” *Nat. Mater.*, vol. 10, no. 8, pp. 569–581, 2011.
- [17] M. Shtein, R. Nadiv, M. Buzaglo, K. Kahil, and O. Regev, “Thermally conductive graphene-polymer composites: Size, percolation, and synergy effects,” *Chem. Mater.*, vol. 27, no. 6, pp. 2100–2106, 2015.
- [18] S. Wu *et al.*, “Aligning multilayer graphene flakes with an external electric field to improve multifunctional properties of epoxy nanocomposites,” *Carbon N. Y.*, vol. 94, pp. 607–618, 2015.
- [19] N. Nuraje, S. I. Khan, H. Misak, and R. Asmatulu, “The Addition of Graphene to Polymer Coatings for Improved Weathering,” *ISRN Polym. Sci.*, vol. 2013, pp. 1–8, 2013.
- [20] F. Soltani-Kordshuli, F. Zabihi, and M. Eslamian, “Graphene-doped PEDOT:PSS nanocomposite thin films fabricated by conventional and substrate vibration-assisted spray coating (SVASC),” *Eng. Sci. Technol. an Int. J.*, vol. 19, no. 3, pp. 1216–1223, 2016.
- [21] J. N. Coleman, U. Khan, W. J. Blau, and Y. K. Gun’ko, “Small but Strong: A Review of the Mechanical Properties of Carbon Nanotube-polymer Composites,” *Carbon N. Y.*, no. 44, pp. 1624–1652, 2006.
- [22] Z. Spitalsky, D. Tasis, K. Papagelis, and C. Galiotis, “Carbon nanotube-polymer composites: Chemistry, processing, mechanical and electrical properties,” *Prog.*

*Polym. Sci.*, vol. 35, no. 3, pp. 357–401, 2010.

- [23] X. Zhao, A. A. Koos, B. T. T. Chu, C. Johnston, N. Grobert, and P. S. Grant, “Spray deposited fluoropolymer/multi-walled carbon nanotube composite films with high dielectric permittivity at low percolation threshold,” *Carbon N. Y.*, vol. 47, no. 3, pp. 561–569, 2009.
- [24] R. H. Todd, D. K. Allen, and L. Alting, *Manufacturing Processes Reference Guide*. Industrial Press Inc., 1994.
- [25] C. Chen, E. M. Kelder, M. J. G. Jak, and J. Schoonman, “Electrostatic\_spray\_deposition\_of\_thin\_1.pdf,” *Solid State Ionics*, no. 86–88, pp. 1301–1306, 1996.
- [26] C. Chen, E. M. Kelder, P. J. J. M. Van Der Put, and J. Schoonman, “Morphology control of thin LiCoO<sub>2</sub> films fabricated using the electrostatic spray deposition (ESD) technique,” *Journal of Materials Chemistry*, vol. 6, no. 5, pp. 765–771, 1996.
- [27] T. Kim, A. Canlier, G. H. Kim, J. Choi, M. Park, and S. M. Han, “Electrostatic Spray Deposition of Highly Transparent Silver Nanowire.pdf,” 2013.
- [28] R. Kumar, S. Singh, and B. C. Yadav, “Conducting Polymers : Synthesis , Properties and Applications,” *Int. Adv. Res. J. Sci. Eng. Technol.*, vol. 2, no. 11, pp. 595–604, 2015.
- [29] E1461–13, “Standard Test Method for Thermal Diffusivity by the Flash Method 1,” *ASTM Int.*, vol. i, pp. 1–11, 2016.

- [30] ASTM - E1269-05, "Standard Test Method for Determining Specific Heat Capacity by Differential Scanning," vol. i, no. Reapproved, pp. 10–15, 2014.
- [31] W. Zhang, H. Zuo, X. Zhang, J. Wang, L. Guo, and X. Peng, "Preparation of graphene-perfluoroalkoxy composite and thermal and mechanical properties," *Polymers (Basel)*, vol. 10, no. 7, 2018.
- [32] Y. He, "Rapid thermal conductivity measurement with a hot disk sensor: Part 1. Theoretical considerations," *Thermochim. Acta*, vol. 436, no. 1–2, pp. 122–129, 2005.
- [33] W. Bauhofer and J. Z. Kovacs, "bauhofer2009\_A review and analysis of electrical percolation in carbon nanotube polymer composites," pp. 1–26, 2008.
- [34] R. D. Hollis, "Scratch Resistance of Mineral-Filled Polypropylene Materials," vol. 4, no. 4.
- [35] C. Xiang and H. Sue, "of High Crystallinity Polypropylene Copolymers," vol. 41, no. 1, pp. 23–31, 2001.
- [36] K. Farokhzadeh, A. Edrisy, and H. Y., "Tribological and Mechanical Properties of Polymer Composite Coatings," *Univ. Wind.*, 2014.
- [37] H. Jiang, R. Browning, and H. Sue, "Understanding of scratch-induced damage mechanisms in polymers," *Polymer (Guildf)*, vol. 50, no. 16, pp. 4056–4065, 2009.
- [38] K. Farokhzadeh, "Modification of Ion Nitriding of Ti-6Al-4V for Simultaneous Improvement of Wear and Fatigue Properties," 2014.

- [39] I. Boedeker Plastics, “Fluoropolymer Plastic Product Family.” [Online]. Available: <https://www.boedeker.com/family/fluoropolymers>.
- [40] “Graphene Supermarket.” [Online]. Available: [available: https://graphene-supermarket.com/](https://graphene-supermarket.com/).
- [41] American Elements The Advanced Materials Manufacturer, “Graphene.” [Online]. Available: <https://www.americanelements.com/graphene-1034343-98-0>.
- [42] American Elements The Advanced Materials Manufacturer, “Multi-Walled Carbon Nanotubes.” [Online]. Available: <https://www.americanelements.com/multi-walled-carbon-nanotubes-308068-56-6>.
- [43] C. A. Schneider, W. S. Rasband, and K. W. Eliceiri, “NIH Image to ImageJ: 25 years of image analysis,” *Nat. Methods*, vol. 9, no. 7, pp. 671–675, 2012.
- [44] P. Benjamin and C. Weaver, “Measurement of adhesion of thin films,” *Proc. R. Soc. A*, vol. 254, no. 1277, 1960.
- [45] Fluorotherm Polymers, “PFA Properties,” 2020. [Online]. Available: <https://www.fluorotherm.com/technical-information/materials-overview/pfa-properties/>.
- [46] M. Mondal, K. Biswas, and J. Maity, “A Transient Heat Transfer Model for Assessment of Flash Temperature During Dry Sliding Wear in a Pin-on-Disk Tribometer,” *Metall. Mater. Trans. A*, vol. 47, pp. 600–607, 2016.
- [47] S. McElwain, T. Blanchet, L. Schadler, and G. Sawyner, “Effect of Particle Size on the Wear Resistance of Alumina-Filled PTFE Micro- and Nanocomposites,”



*Tribol. Trans.*, vol. 51, pp. 247–253, 2008.

- [48] S. Chauhan and S. Thakur, “Effects of Particle Size, Particle Loading and Sliding Distance on the Friction and Wear Properties of Cenosphere Particulate Filled Vinylester Composites,” *Mater. Des.*, vol. 51, pp. 398–408, 2013.

## Vita Auctoris

NAME: Mitchell Cierpisz

PLACE OF BIRTH: Windsor, Ontario

YEAR OF BIRTH: 1994

EDUCATION: Assumption High School, Windsor  
2008-2012

University of Windsor, Windsor, Ontario  
2012-2016 B.A.Sc.

University of Windsor, Windsor, Ontario  
2016-2020 M.A.Sc.